Economic Geology

BULLETIN OF THE SOCIETY OF ECONOMIC GEOLOGISTS

VOL. 113 March–April NO. 2

Structural Controls on Porphyry Au-Cu and Au-Rich Polymetallic Carbonate-Hosted Replacement Deposits of the Kassandra Mining District, Northern Greece

Chris R. Siron,[1,†] David Rhys,[2] John F.H. Thompson,[1] Tim Baker,[3] Theodore Veligrakis,[4] Alfredo Camacho,[5] and Lazaros Dalampiras[4]

[1]*Department of Earth and Atmospheric Sciences, Cornell University, Ithaca, New York 14853*

[2]*Panterra Geoservices Inc., 14180 Greencrest Dr., Surrey, British Columbia V4P 1L9, Canada*

[3]*Eldorado Gold Corporation, 1188 Bentall 5, 550 Burrard St., Vancouver, British Columbia V6C 2B5, Canada*

[4]*Eldorado Gold Exploration, 23a Vassilissis Sofias Ave. 106 74, Athens, Greece*

[5]*Department of Geological Sciences, University of Manitoba, 240 Wallace Building, 125 Dysart Road, Winnipeg R3T 2N2, Manitoba, Canada*

Abstract

The Kassandra mining district of northern Greece contains about 12 Moz Au in porphyry Au-Cu and Au-Ag-Pb-Zn-Cu carbonate replacement deposits that are associated with Oligocene-Miocene intrusions emplaced into polydeformed metamorphic basement rocks belonging to the Permo-Carboniferous to Late Jurassic Kerdilion unit and the Ordovician-Silurian Vertiskos unit. Regional extensional tectonics active since the middle Eocene resulted in the development of widespread normal and transtensional faults, including the Stratoni fault zone that hosts carbonate replacement sulfide orebodies. This structure has been previously interpreted as the tectonic boundary between the Kerdilion and Vertiskos units. Geologic relationships, structural patterns, immobile element geochemistry, and published zircon U-Pb ages suggest that the tectonic boundary between these lithotectonic units is an older structure and not a detachment fault as previously indicated.

Carbonate-hosted replacement orebodies at the Olympias, Madem Lakkos, and Mavres Petres deposits are controlled by the Kassandra fault and Stratoni fault zones. Orebody location and morphology is influenced by a preexisting ductile structural architecture and the interaction of ductile to brittle faults with marble host rocks. Intersection of ductile fabrics and folds with extensional mylonites and synmineral semibrittle shear zones form a linear plunging domain that controls sulfide ore at the Olympias deposit. The Madem Lakkos sulfide orebodies are hosted by marbles located within fold hinges and intersecting semibrittle faults, whereas the Mavres Petres orebody is controlled by lenses of marble entrained within the Stratoni fault zone. Hydrothermal mica $^{40}Ar/^{39}Ar$ ages indicate that sulfide ore deposition occurred between 24.0 ± 0.6 and 22.6 ± 0.3 Ma, overlapping with late Oligocene magmatism in the district. Kinematic fault-slip data and field relationships suggest that carbonate replacement mineralization within the Stratoni fault zone was initiated toward the end of north-south extension during the late Oligocene, whereas younger Au-bearing quartz-rhodochrosite vein breccias that are spatially related to but crosscut sulfide ores were controlled largely by east-west extension.

The Skouries Au-Cu deposit is hosted by an early Miocene quartz monzonite porphyry stock that postdates the folding of gneiss and schist of the Vertiskos unit. Mineralized veins within the stock and porphyry dikes predominately strike northeast, consistent with the orientation of the Oligo-Miocene igneous belt. Ascent of fertile magmas into the upper crust may have been triggered by a change in the extension direction during the early Miocene. Magmatism during the late Oligocene and early Miocene corresponds to distinct extensional episodes that facilitated polymetallic carbonate replacement and porphyry Au-Cu ore formation within an evolving post-collisional tectonic setting.

† Corresponding author: email, crs344@cornell.edu

Economic Geology, v. 113, no. 2, pp. 309–345
ISSN 0361-0128; doi: 10.5382/econgeo.2018.4552; 37 p.
Supplementary files available online.

Submitted: May 25, 2017
Accepted: November 6, 2017

Introduction

The Serbo-Macedonian metallogenic province (Janković, 1997; Serafimovski, 2000) of the Tethyan mineral belt forms a NW-trending zone of porphyry Au-Cu, Cu skarn, and Au-rich polymetallic vein and carbonate-hosted replacement deposits extending from Serbia and Kosovo through the Republic of Macedonia and northern Greece. Deposits within this belt are associated with Oligo-Miocene intrusions occurring within a tectonically complex environment (Heinrich and Neubauer, 2002). The most economically significant district in the Greek segment of the Serbo-Macedonian metallogenic province is the Kassandra mining district, which contains about 12 Moz Au hosted by porphyry and polymetallic carbonate replacement orebodies. The Skouries porphyry Au-Cu deposit contains a measured and indicated resource of 289.3 Mt grading 0.58 g/t Au and 0.43% Cu. The Olympias carbonate replacement deposit contains a measured and indicated resource of 15.1 Mt at 8.97 g/t Au, 146 g/t Ag, 4.9% Pb, and 6.5% Zn (Eldorado Gold Corporation, 2017). Approximately 13.5 Mt of Ag-Pb-Zn ore was historically produced from the Madem Lakkos carbonate replacement deposit (Forward et al., 2010) with the nearby and actively producing Mavres Petres mine containing a measured and indicated resource of 0.55 Mt at 212 g/t Ag, 8.1% Pb, and 11.0% Zn (Eldorado Gold Corporation, 2017).

Zircon U-Pb geochronology defines two magmatic episodes that took place within the Kassandra mining district during the late Oligocene and early Miocene, each of which corresponds to a major metallogenic event (Frei, 1992, 1995; Gilg, 1993; Gilg and Frei, 1994; Hahn et al., 2012; Siron et al., 2016). Previous studies (e.g., Haines, 1998) recognized the Stratoni fault zone as a major mineralized corridor that hosts the Mavres Petres and Madem Lakkos Au-Ag-Pb-Zn-Cu carbonate replacement-style massive sulfide deposit. Based on crosscutting relationships with respect to dated igneous intrusions, sulfide ore is interpreted to have formed syn- to postemplacement of the late Oligocene (~25 Ma) Fisoka and Stratoni granodiorite stocks (Siron et al., 2016). The Olympias Au-Ag-Pb-Zn-Cu carbonate replacement deposit, located to the north of the Stratoni fault zone, occurs within a folded marble-gneiss sequence and is closely associated with the Kassandra fault. Sulfide ore from the Olympias deposit shows mineralogical and textural similarities to the Mavres Petres deposit (Siron et al., 2016). These similarities and an arsenopyrite Re-Os age have led previous workers to assign an Oligo-Miocene age to the Olympias deposit (Kalogeropoulos et al., 1989; Hahn et al., 2012; Hahn, 2014).

The Skouries Au-Cu deposit is associated with a narrow, steeply plunging, pipe-shaped and multiphase quartz monzonite porphyry intrusion (Eliopoulos and Economou-Eliopoulos, 1991; Frei, 1992, 1995; Tobey et al., 1998; Kroll et al., 2002; Hahn et al., 2012; Hahn, 2014; McFall et al., 2016; Siron et al., 2016). Published K-Ar whole-rock and zircon U-Pb ages from the Skouries porphyry and a hydrothermal biotite $^{40}Ar/^{39}Ar$ cooling age are within error and define a 20 to 19 Ma age range for Au-Cu mineralization (Frei, 1992, 1995; Hahn et al., 2012; Hahn, 2014). Based on these ages, the Skouries deposit is interpreted to be ~4 to 5 m.y. younger than the fault-controlled carbonate-hosted replacement massive sulfide deposits to the north (Siron et al., 2016).

In spite of the economic importance of the Kassandra mining district and the demonstrable association of the Madem Lakkos and Mavres Petres deposits with the Stratoni fault zone, little previous work has been done to assess the structural controls on ore deposit formation. Previous work is limited to a study of the Stratoni fault zone on one level in the now-closed Madem Lakkos mine by Haines (1998) and district-scale reviews in unpublished consulting reports. This study presents the results of research focused on characterizing the kinematic and structural controls on mineralization and identifying the structural architecture that facilitated faulting and Oligo-Miocene magmatism associated with porphyry and carbonate replacement mineralization. We present detailed geologic maps and cross sections from the Olympias, Madem Lakkos, Mavres Petres, and Skouries deposits based on field and drill core observations, structural measurements, and fault kinematic analyses, as well as whole-rock geochemical data (Appendix). The location and importance of the Stratoni fault zone as a potential terrane-bounding structure is discussed in the context of whole-rock geochemistry and the age of the metamorphic units from previous zircon U-Pb data. The objectives of this study are to (1) define the structural architecture and deformation history of the district, (2) characterize the style, timing, and significance of faulting, and (3) identify the major structural controls that focused polymetallic carbonate replacement and porphyry Au-Cu systems within the Kassandra mining district.

Lithotectonic Setting

The Hellenic orogen of northern Greece originated from the collision of the Apulian and Pelagonian microcontinents with the previously accreted Serbo-Macedonian and Rhodope continental fragments to the Eurasian continental margin during the Late Cretaceous to Eocene (Pe-Piper and Piper, 2006). Convergence of microcontinents and subduction of oceanic lithosphere during this event led to magmatism resulting from slab detachment or lithospheric delamination assisted by rollback of the subducting slab during postcollisional back arc extension of the subducted wedge (de Boorder et al., 1998; Wortel and Spakman, 2000; Lips, 2002; Neubauer, 2002; Brun and Sokoutis, 2010; Jolivet and Brun, 2010; Krenn et al., 2010; Ring et al., 2010; Jolivet et al., 2013; Papanikolaou, 2013). Retreat of the subducting slab resulted in widespread extension that manifested in the unroofing of deep-crustal lithotectonic blocks from the Late Cretaceous to the late Miocene (Dinter and Royden, 1993; Sokoutis et al., 1993; Wawrzenitz and Krohe, 1998; Krohe and Mposkos, 2002; Brun and Sokoutis, 2007; Brun and Faccenna, 2008; Wüthrich, 2009; Kydonakis et al., 2014; Kounov et al., 2015).

Northeastern Greece is principally underlain by rocks belonging to the Rhodope metamorphic province, defined as a crustal-scale, amphibolite-facies accretionary complex consisting of SW-verging stacked nappes that lie within the overriding plate of the Hellenic subduction zone (Burg et al., 1990, 1996; Ricou et al., 1998; Gautier et al., 1999; Bonev et al., 2006; Jahn-Awe et al., 2010; Krenn et al., 2010; Burg, 2012). Bordered by the Maritza dextral strike-slip fault in southern Bulgaria, the Rhodope metamorphic province extends under the Thrace basin of northeastern Greece and is bounded by the ophiolitic Vardar suture zone, which crops out on the

western Chalkidiki Peninsula (Fig. 1; Ricou et al., 1998). The Rhodope metamorphic province comprises the eastern and structurally stacked Thracia and Rhodope lithotectonic terranes and the western Serbo-Macedonian terrane. The upper tectonic Permo-Carboniferous Rhodope unit, which hosts Late Jurassic orthogneiss, is separated from the lower Thracia terrane by the SW-verging Nestos thrust fault (Fig. 1; Turpaud and Reischmann, 2010). The Permo-Carboniferous Thracia terrane consists of the lower Pangeon and upper Kerdilion marble-gneiss sequences. On the Chalkidiki Peninsula, the Kerdilion unit is tectonically juxtaposed with Ordovician to Silurian orthogneiss and Triassic leucogranites belonging to

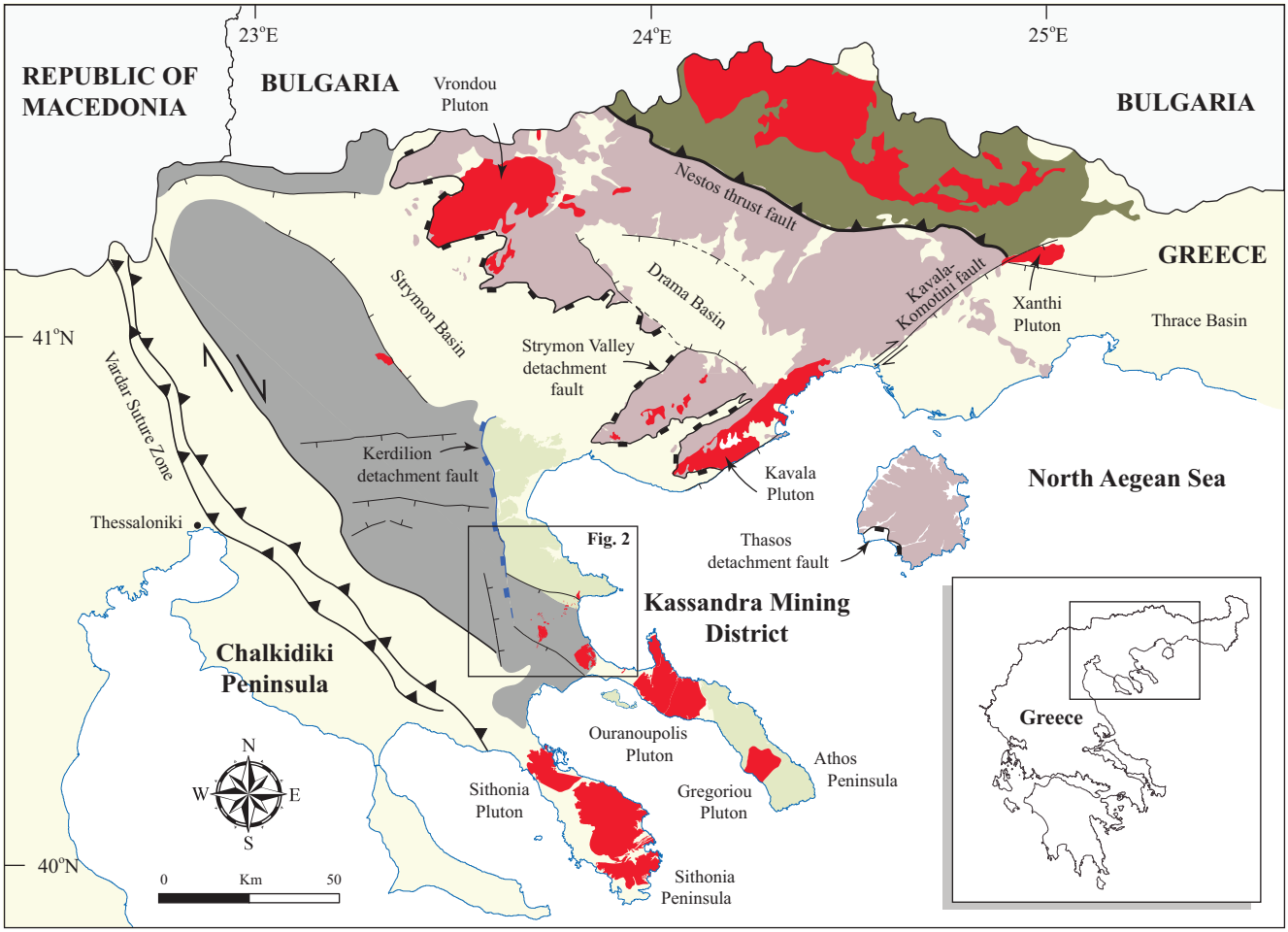

Fig. 1. Simplified regional geologic map of northeastern Greece modified after Kydonakis et al. (2014). The Maritza fault lies outside of the figure area and only the tectonic units referenced in the text are displayed. The Strymon Valley detachment fault and the Kavala-Komotini fault are after Dinter (1998), the Thasos detachment fault is after Wawrzenitz and Krohe (1998), and the Kerdilion detachment fault is adapted from Brun and Sokoutis (2007). Inset shows map location.

the Vertiskos unit of the Serbo-Macedonian terrane (Fig. 1; Himmerkus et al., 2007).

The Kassandra mining district is underlain by Vertiskos and Kerdilion units (Fig. 1; Kockel et al., 1971, 1977; Brun and Sokoutis, 2007), which are interpreted to be the upper and lower tectonic units, respectively, of the Serbo-Macedonian terrane (Kockel et al., 1971). The Vertiskos unit is interpreted to be a Gondwanan-derived continental magmatic arc that was accreted onto the European margin in the Carboniferous (Himmerkus et al., 2006, 2007, 2009a). In contrast, zircon ages and whole-rock geochemical data suggest that the Kerdilion unit originated from a Permo-Carboniferous magmatic arc, which was overlain by Paleotethyan carbonates and was subsequently modified by Late Jurassic to Early Cretaceous arc magmatism related to the Neotethyan subduction zone (Turpaud and Reischmann, 2003; Himmerkus et al., 2007, 2011). The contact between the Vertiskos and Kerdilion units has been interpreted in earlier studies as the Stratoni fault zone (e.g., Nebel et al., 1991; Haines, 1998). Himmerkus et al. (2005), however, reassigned this tectonic boundary to the Athos-Volvi suture zone (Fig. 2).

Ultramafic and mafic rocks cropping out within the Athos-Volvi suture zone belong to the Thermes-Volvi-Gomati ophiolite complex, first described in detail by Dixon and Dimitriadis (1984) and interpreted to represent mantle-derived magmas formed by rifting in a suprasubduction zone setting during the Late Permian to Early Triassic (Himmerkus et al., 2005; Liati et al., 2011; Bonev et al., 2012). Late Triassic anorogenic granites of the Arnea-Kerkini Suite were emplaced within a rift setting that is broadly coeval with the formation of the ophiolitic rocks (Dixon and Dimitriadis, 1984; De Wet et al., 1989; Himmerkus et al., 2005, 2009b; Christofides et al., 2007; Bonev et al., 2012). Neoproterozoic basement fragments including gneisses of the Arnea-Kerkini Suite and dismembered segments of the Thermes-Volvi-Gomati ophiolite sequence were incorporated into the Athos-Volvi suture zone during Late Paleozoic to Mesozoic assembly of the European margin during closure of the Neotethyan Vardar Ocean and inception of the Alpine-Hellenic orogeny (Fig. 2; Dixon and Dimitriadis, 1984; Bonev and Dilek, 2010; Liati et al., 2011).

Accretion of the Vertiskos continental fragment to the European margin was accompanied by regional high-temperature, upper greenschist- to lower amphibolite-facies metamorphism that overprinted an earlier and discrete high-pressure subduction-related eclogite-facies event (Wawrzenitz and Mposkos, 1997; Lips et al., 2000; Mposkos and Kostopoulos, 2001; Liati, 2005; Turpaud and Reischmann, 2010; Kydonakis et al., 2014, 2016). Synmetamorphic thrust faulting and exhumation of the Vertiskos unit to midcrustal levels occurred by early Late Cretaceous time (Kydonakis et al., 2016). The Kerdilion unit, however, underwent amphibolite-facies metamorphism that locally reached anatectic partial melt conditions by the early to middle Eocene and was subsequently overprinted by retrograde greenschist-facies metamorphism (Kalogeropoulos et al., 1989; Wawrzenitz and Krohe, 1998; Lips et al., 2000). Thermochronological studies suggest contrasting evolutionary paths for the Vertiskos and Kerdilion units (Burg et al., 1995; Brun and Sokoutis, 2007; Kounov et al., 2015; Kydonakis et al., 2016).

Tertiary magmatism and regional extension

Early Eocene subduction-related arc magmatism is evident throughout the Rhodope metamorphic province. Rollback of the subducting slab and back arc extension in the north Aegean region gave way to postcollisional magmatism from the Oligocene to early Miocene (Fytikas et al., 1984; Jones et al., 1992; Dinter et al., 1995; Pe-Piper and Piper, 2002; Ring et al., 2010). A southward migration of the magmatic arc resulted from the retreat of the Hellenic trench from the late Miocene into the Pliocene. This occurred coeval with northward collision of the Arabian plate with Eurasia, facilitating westward extrusion of the Anatolian block into the northern Aegean (Jolivet et al., 2013). Since the middle Miocene, this westward escape of Anatolia has been largely accommodated by regional north-south crustal stretching and dextral displacement on the north Anatolia fault (Armijo et al., 1998; Gautier et al., 1999; Jolivet et al., 2013), which propagated into the north Aegean Sea by approximately 5 Ma (Armijo et al., 1998; Koukouvelas and Aydin, 2002).

Extensional tectonics have been active in the north Aegean region since the middle to late Eocene beginning with the unroofing of the southern Rhodope core complex in the footwall of the inferred Kerdilion detachment fault (Fig. 1; Brun and Sokoutis, 2007, 2010). Exposure of the Kerdilion detachment fault is limited and is largely defined by thermochronology. Fission track age patterns from the study area indicate that the footwall Kerdilion unit cooled below the apatite and zircon partial annealing temperatures from 42 to about 24 Ma coincident with detachment faulting and exhumation of the Kerdilion unit (Wüthrich, 2009; Kounov et al., 2015). A similar conclusion was reached by Brun and Sokoutis (2007) based on the reinterpretation of previously published isotopic cooling ages from the region.

Continued exhumation of the previously unroofed metamorphic dome was accompanied by early Miocene magmatism and accommodated by the Thasos and Strymon Valley detachment faults located northeast of the Kassandra mining district (Fig. 1; Dinter and Royden, 1993; Sokoutis et al., 1993; Dinter et al., 1995; Dinter, 1998; Wawrzenitz and Krohe, 1998). Unroofing of the southern Rhodope core complex continued into the late Pliocene where it was modified by late Pliocene to Quaternary basin-forming normal and strike-slip faults (Dinter, 1998). Exhumation of the southern Rhodope core complex reflects an estimated 120 km of extension accompanied by approximately 30° clockwise rotation of the Chalkidiki block from the middle Eocene to present as determined from paleomagnetic studies (Dimitriadis et al., 1998; Brun and Sokoutis, 2007).

Regional Structural Framework

The Kassandra mining district is underlain by metamorphic rocks belonging to the polydeformed Vertiskos and Kerdilion units (Kockel et al., 1977), including mafic and ultramafic bodies mainly occupying areas around the Gomati and Stratoni fault zones (Fig. 2). Subduction-related Late Cretaceous to early Eocene calc-alkaline magmatism was followed by the emplacement of postcollisional late Oligocene and early Miocene intrusions along a NE-trending corridor hosted by both Vertiskos and Kerdilion units (Siron et al., 2016). This section

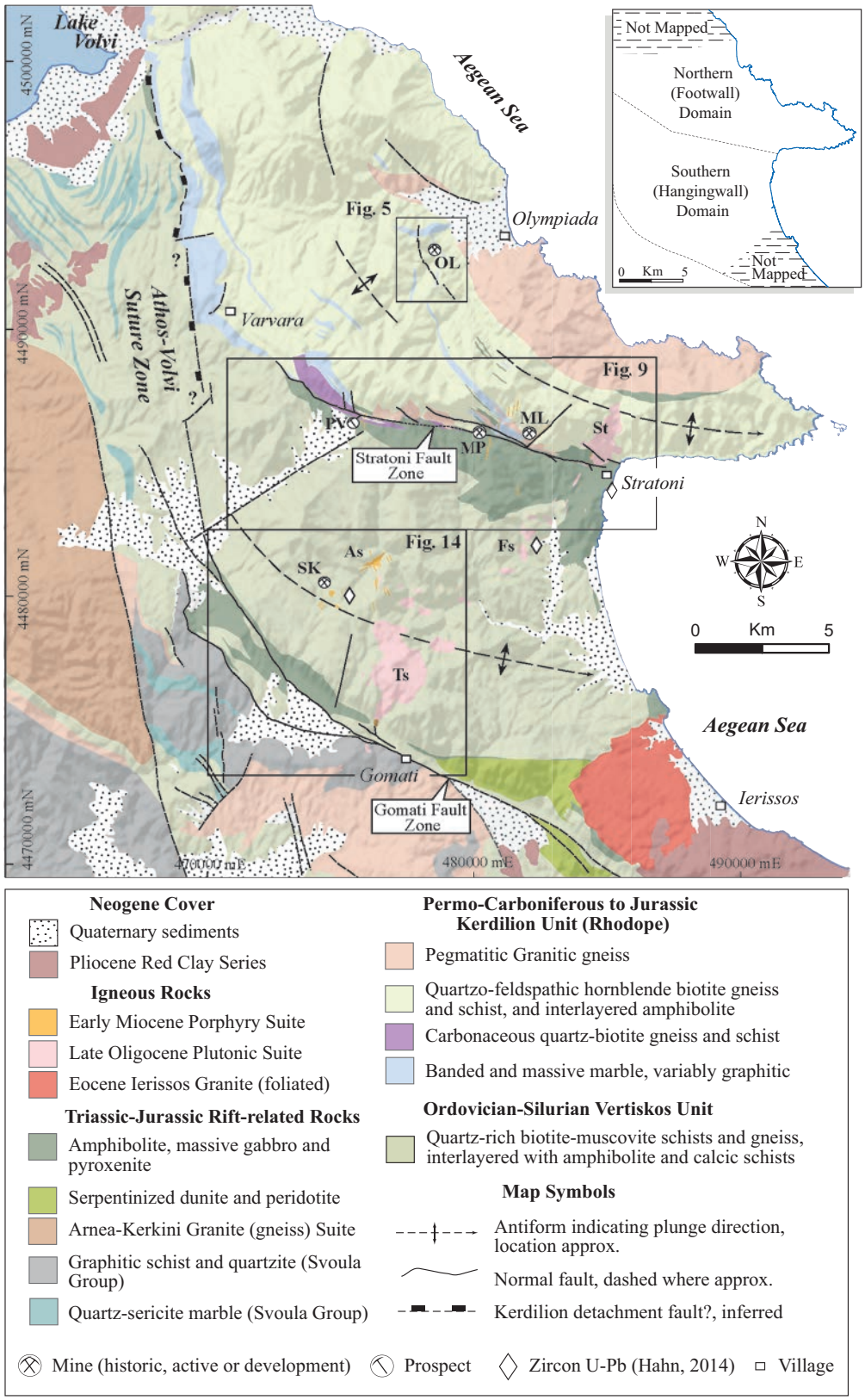

Fig. 2. Geologic map of the Kassandra mining district modified after Kockel et al. (1977). The inset map at the top right outlines the northern and southern structural domains referenced in the text. Coordinates are displayed in the Greek Geodetic Coordinate System (GGRS 87 Greek Grid). Abbreviations: As = Aspro Lakkos porphyry stock, Fs = Fisoka stock, ML = Madem Lakkos deposit, MP = Mavres Petres deposit, OL = Olympias deposit, PV = Piavitsa prospect, SK = Skouries deposit, St = Stratoni stock, Ts = Tsikara composite stock.

presents lithologic descriptions of these metamorphic basement units based on field and drill core observations, combined with previously published geochronological data. Major deformation events recorded by these rocks are described from structural data collected from surface outcrops.

Metamorphic basement rocks

Metamorphic rocks of the Kerdilion unit to the north of the Stratoni fault zone consist of partially migmatitic quartzofeldspathic hornblende-biotite gneiss containing intervals of compositionally layered to massive graphite-bearing marble, metagabbros composed of massive to strongly layered amphibolite, interspersed bodies of megacrystic plagioclase-microcline orthogneiss, and fine-grained to aplitic granite gneiss (Kockel et al., 1977; Kalogeropoulos et al., 1989; Nebel et al., 1991; Gilg and Frei, 1994). These lithologic units have an arcuate geometry, striking in a north-south direction in the north and becoming east-west striking near the Stratoni fault zone (Fig. 2). Middle Jurassic to Early Cretaceous zircon U-Pb and Pb-Pb ages from granitic gneiss of the Kerdilion unit range from 164 to 134 Ma and are interpreted as primary igneous ages reflecting a period of widespread magmatism within the region (Himmerkus et al., 2011; Hahn, 2014). The hosting rock units, however, are likely Carboniferous to Permian in age based on inherited zircon cores derived from the orthogneiss (Himmerkus et al., 2011). Pegmatitic dikes and sills occur throughout the Kerdilion unit. These probably represent anatectic partial melts of the metamorphic rock from about the middle Paleocene to middle Eocene (Wawrzenitz and Krohe, 1998; Kalogeropoulos et al., 1989). These dikes commonly contain a penetrative foliation and may be folded and boudinaged, indicating that ductile deformation persisted through at least the middle Eocene (Kalogeropoulos et al., 1989; Gilg and Frei, 1994). Pegmatitic gneisses and dikes are largely absent south of the Stratoni fault zone.

Strongly foliated and variably graphitic garnet-bearing quartz-biotite gneiss and schist (metapelites) define a distinct unit that is spatially associated with the Stratoni fault zone (Fig. 2). This unit is exposed underground in the Mavres Petres mine and is present in outcrop and drill core at the Piavitsa prospect. Quartz-biotite ± garnet gneiss and schist consist of thinly laminated quartz-rich lenses grading into layers with abundant graphite. Drill core intercepts indicate that the graphitic quartz-biotite gneiss and schist unit is conformable with quartzofeldspathic biotite gneiss and is interlayered with graphite-bearing marble, calcareous schists, and thin amphibolite layers. The graphitic metapelite unit is extensively altered in the Stratoni fault zone where a black, insoluble carbonaceous residue is focused within pressure solution seams and biotite, feldspar, and garnet are variably altered to white mica-chlorite-carbonate to form a gray, carbonaceous phyllite.

Mafic and ultramafic rocks are exposed predominately within the hanging wall of the Stratoni fault zone (Fig. 2); however, thinner mafic layers also occur to the north and extend into the Olympias area. These rocks consist of layered- and massive-textured amphibolite with subordinate pods of variably serpentinized pyroxenite. Amphibolite units that occur to the north of the Stratoni fault zone are interlayered with marble and have contacts that are compositionally gradational with hornblende-bearing quartzofeldspathic biotite gneiss. Amphibolites in this area are potentially correlative with the Triassic Thermes-Volvi-Gomati ophiolitic complex (Dixon and Dimitriadis, 1984; Bonev and Dilek, 2010; Liati et al., 2011); however, a Middle Jurassic zircon U-Pb age of 167 Ma was obtained from feldspar-rich banded amphibolite south of the village of Stratoni (Fig. 2; Hahn, 2014).

A monotonous sequence of quartz-rich feldspathic to muscovite-biotite–bearing gneiss and schist assigned to the Vertiskos unit occurs to the south of the Stratoni fault zone and the large amphibolite unit described above (Fig. 2). Minor calcareous calc-silicate schist, marble, and amphibolite are thinly interlayered within the metamorphic sequence. Zircon U-Pb ages (Hahn, 2014) show that the micaceous schist in the Skouries area ranges from Neoproterozoic (686–576 Ma) to Ordovician (464–450 Ma), which is consistent with the age of the Pan-African Pirgadikia and Vertiskos units of the Serbo-Macedonian terrane, respectively (Himmerkus et al., 2006, 2007). Hahn (2014) additionally identified a broad range of zircon ages from a micaceous schist near the southern amphibolite contact south of the Stratoni fault zone (Fig. 2). Three populations of zircon U-Pb ages from Neoproterozoic (699–594 Ma), Ordovician to Silurian (475–428 Ma), and Permian to Triassic (279–228 Ma) correspond to the Pirgadikia unit, Vertiskos unit, and the Arnea-Kerkini granite gneiss suite, respectively (Himmerkus et al., 2006, 2007). This wide distribution of zircon ages, which includes rare Neoarchean zircon cores (2519 Ma), reflects either a complex detrital sedimentary precursor and/or a mélange of structurally imbricated basement units.

In the southernmost parts of the study area, mafic and ultramafic rocks consisting of chlorite-amphibole schist, metagabbro, and chromite-bearing serpentinized peridotite and dunite crop out along the Gomati fault zone (Fig. 2). These rocks belong to the dismembered Gomati ophiolite body and are interpreted to be the lowest structural position of the Thermes-Volvi-Gomati ophiolitic complex (Kockel et al., 1977; Dixon and Dimitriadis, 1984; Bonev and Dilek, 2010). This mafic to ultramafic body is mostly hosted by the tectonic mélange of the Athos-Volvi suture zone (Himmerkus et al., 2005).

Tertiary igneous rocks

Three suites of subduction-related and postcollisional igneous rocks crop out within the Kassandra mining district. The earliest suite comprises late Paleocene to early Eocene intrusions that are variably deformed. The most significant intrusion from this suite is the ca. 53 Ma subduction-related calc-alkaline Ierissos granodiorite (Frei, 1992, 1996; Himmerkus et al., 2011), which crops out to the southeast of the district (Fig. 2) and is coeval with the Sithonia, Ouranoupolis, and Grigoriou granodiorites located on the Sithonia and Athos peninsulas, respectively (Fig. 1; De Wet et al., 1989; Christofides et al., 1990; Bébien et al., 2001; Pe-Piper and Piper, 2002). Other intrusions in this suite include foliated granodiorite dikes that crop out within the Stratoni fault zone between the Stratoni granodiorite stock and the Madem Lakkos deposit. One of these granodiorite dikes yielded a zircon U-Pb crystallization age of 58.0 ± 0.2 Ma (C. Siron, unpub. data, 2016), suggesting that the late Paleocene to Eocene subduction-related

igneous event extended to the north into the Kassandra mining district.

A NE-trending, 15-km-long belt of postcollisional intrusive rocks of Oligo-Miocene age mostly crops out between the Gomati and Stratoni fault zones (Fig. 2) and represents the two youngest intrusive suites in the study area (Gilg and Frei, 1994; Hahn, 2014; Siron et al., 2016). Zircon U-Pb geochronology defines two distinct postcollisional magmatic episodes in the late Oligocene (27–25 Ma) and early Miocene (20–19 Ma). Both igneous suites belong to the high-K calc-alkaline magma series with the younger early Miocene porphyritic intrusions having a more-evolved, shoshonitic geochemistry (Kroll et al., 2002; Siron et al., 2016). The late Oligocene igneous suite includes monzogabbros and granodiorites belonging to the 27.0 ± 0.2 to 26.7 ± 0.3 Ma Tsikara composite stock in the south and the 25.7 ± 0.4 to 24.5 ± 0.1 Ma variably porphyritic diorite to granodiorite stocks and dikes of Stratoni and Fisoka in the north (Fig. 2; Siron et al., 2016).

The early Miocene igneous suite includes the 20.6 ± 0.5 Ma (zircon U-Pb; Hahn et al., 2012; Hahn, 2014) Au-Cu–mineralized Skouries quartz monzonite porphyry stock (Fig. 2). Highly potassic glomerophyric porphyry dikes that crosscut the Stratoni fault zone and the Olympias deposit are interpreted to be early Miocene in age, coeval with the Skouries stock (Siron et al., 2016). Early Miocene magmatism continued with the emplacement of the barren Aspro Lakkos quartz monzonite porphyry stock (19.7 ± 0.1 Ma) and crosscutting trachyandesite black-matrix porphyry dikes dated at 19.6 ± 0.1 Ma (Siron et al., 2016). The youngest stage of magmatism in the district is documented by the 19.2 ± 0.2 Ma trachyandesite black-matrix porphyry dike hosted within the Vathilakkos fault at the Madem Lakkos deposit (Gilg and Frei, 1994; Haines, 1998; Siron et al., 2016).

Deformation events

In this study, the Kassandra mining district has been divided into two structural domains, north and south of the Stratoni fault zone (inset, Fig. 2). Structural analyses also focused on the Olympias and Skouries deposit areas to better establish the local structural architecture. Ductile structural data is displayed in lower-hemisphere, equal-area stereographic projections and is presented in Figure 3. Three deformation episodes are defined here based on the superposition of ductile fabrics. Earlier events may have occurred but are obscured by the intensity of D_1 strain and associated metamorphism.

D_1 deformation: Gneisses and marbles within the northern domain display a locally preserved compositional layering that is transposed into the plane of a penetrative S_1 gneissosity, which affects granitic intrusions as young as 58 Ma (C. Siron, unpub. data, 2016). Foliation is defined by the alignment of peak amphibolite-facies minerals typically consisting of hornblende-biotite-plagioclase ± garnet and feldspathic mineral segregations within quartzofeldspathic biotite gneiss and amphibolite. In marble, compositional banding is parallel to the plane of S_1 foliation (Fig. 4A). Massive marble that hosts sulfide ore commonly contains aligned graphite flakes that define the S_1 fabric. Pegmatites that occupy the metamorphic sequence occur as thin layer-parallel leucosomes within migmatitic intervals of quartzofeldspathic biotite gneiss and as dikes that crosscut the metamorphic package. Most pegmatites generally exhibit a penetrative S_1 foliation (Kalogeropoulos et al., 1989). Within the Olympias deposit area, S_1 foliation strikes predominately to the north and uniformly dips to the east, as observed from surface outcrops and underground exposures. Orientation of the metamorphic sequence and the S_1 foliation abruptly shifts to an east-west strike with a shallow south dip to the north of the deposit area, likely representing a D_2 fold (Fig. 3A). North of the Stratoni fault zone, S_1 foliation dips to the north-northeast and south-southwest, defining a fold geometry (Fig. 3B). Asymmetry of granite gneiss and pegmatite boudins within the quartzofeldspathic biotite gneiss sequence show top-to-the-northeast sense of shear of S_1 foliation in the northern domain as similarly noted by Kilias et al. (1999).

Immediately to the south of the Stratoni fault zone, S_1 foliation strikes west-northwest and dips predominately toward the north-northeast, discordant to the S-dipping Stratoni fault zone (Fig. 3C). The moderate northeast dip to S_1 foliation extends into the Skouries area, where S_1 becomes south to southwest dipping, thus defining a broad D_2 anticlinorium (Fig. 3D). Foliation traces diverge from the Stratoni fault zone, striking north-south parallel to the coastline and roughly following the outcrop pattern of the mafic hanging-wall rocks on the eastern margin of the district (Fig. 2). S_1 foliation exhibits a northeast strike and southwest dip in the southeast portion of the district. Foliation boudins evident within the well-foliated mafic rocks south of the Stratoni fault zone locally occur as lenticular and symmetrical pyroxenite lozenges within amphibolite, thus recording high degrees of strain during the D_1 event.

D_2 deformation: A second ductile fabric (S_2) overprints and locally transposes the previously developed S_1 foliation and is associated with upper greenschist- to lower amphibolite-facies metamorphism based on the realignment and growth of phyllosilicate minerals (e.g., biotite) into S_2 foliation planes. Within the northern domain, the S_2 foliation forms a spaced to locally penetrative cleavage that dips gently to the south-southeast (Fig. 3E). S_2 cleavage is present within the axes of folds at the Olympias deposit, where it manifests as a penetrative fabric resulting in the realignment of biotite in the quartzofeldspathic gneiss and as thin pressure solution partings and realignment of graphite flakes in marble. S_2 cleavage is generally poorly developed within the massive, mica-poor and coarse-grained to megacrystic granitic gneiss that underlies much of the eastern portion of the northern domain. In general, S_2 cleavage is subparallel to S_1 foliation at the southern margin of the northern domain within the Stratoni fault zone. In the southern domain, the S_2 fabric occurs as a tightly spaced, penetrative crenulation cleavage (Fig. 4B) that dips moderately to the south (Fig. 3F) and is commonly localized in the axes of folds best developed in metapelitic layers. Poles to axial planar S_2 foliation measured in the Skouries area and surrounding parts of the southern domain display a clustered distribution with no evidence of post-D_2 folding. This relationship is consistent with the orientation and distribution of F_2 axial planes.

Folds associated with the D_2 event (F_2 folds) affected the metamorphic sequences in the northern and southern domains. Folds have interlimb angles that range from open to tight and commonly have inclined to near-recumbent

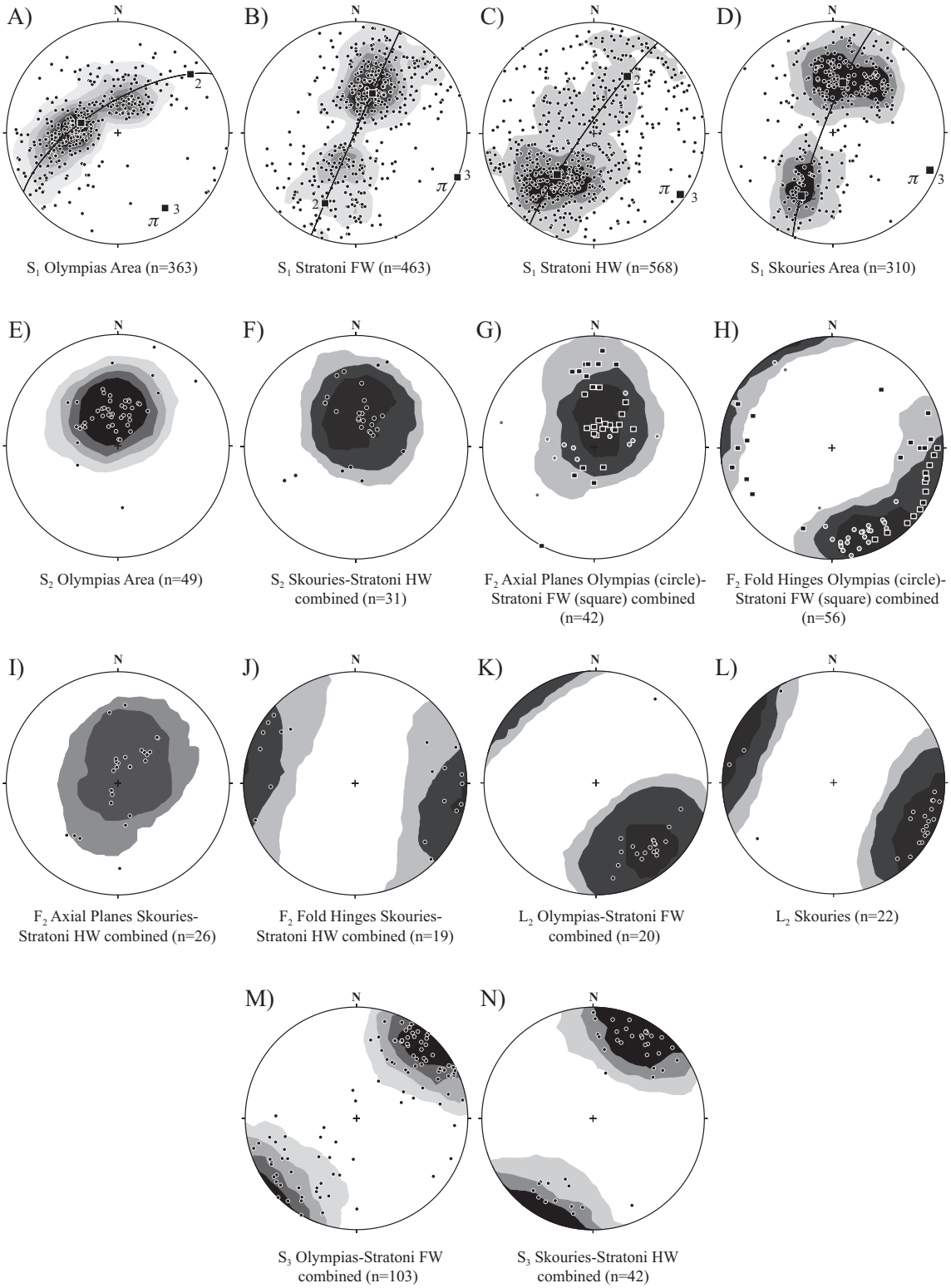

Fig. 3. Lower-hemisphere, equal-area stereographic projections of ductile structural elements subdivided by domain in the study area. Data is contoured at 3σ significance level following the method of Kamb (1959): (A-D) S_1 foliation plotted as poles from planes. Best-fit great circle, orthogonal axial distributions, and plunge of the F_2 fold axis are plotted as a solid line, black squares, and π symbol respectively. (E-F) S_2 cleavage plotted as poles from planes. (G-H) Axial planes of F_2 folds plotted as poles from planes with corresponding orientation of F_2 fold hinges from the Olympias area and Stratoni fault footwall domain. (I-J) Axial planes of F_2 folds plotted as poles from planes with corresponding orientation of F_2 fold hinges from the Skouries area and Stratoni fault hanging-wall domain. (K-L) S_1-S_2 foliation intersection. (L_2) Lineations plotted as lines. (M-N) S_3 foliation plotted as poles from planes. Abbreviations: FW = footwall, HW = hanging wall.

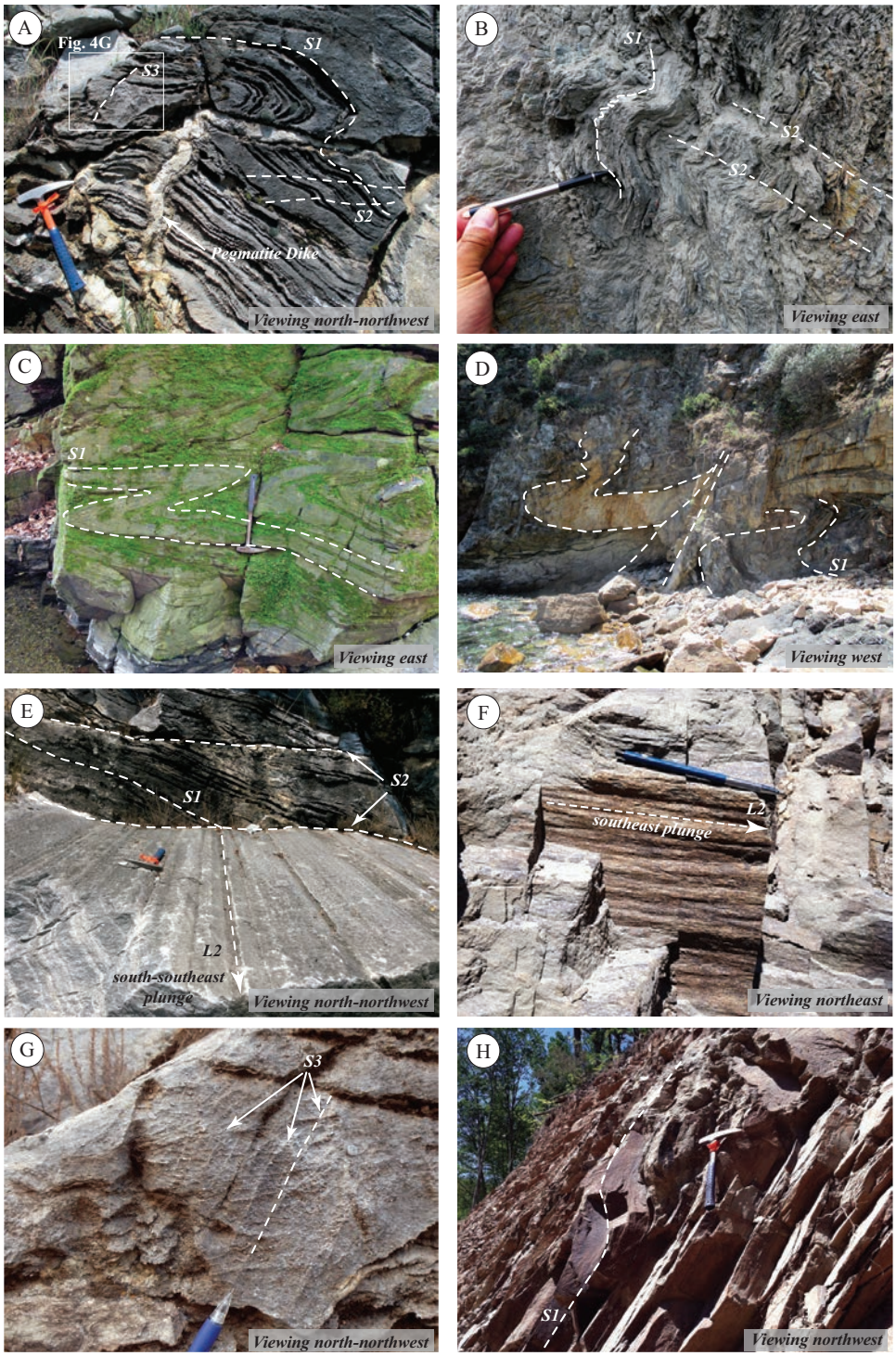

Fig. 4. Photos of representative ductile structural elements from the Kassandra mining district. (A) Outcrop of folded Kerdilion marble on the Varvara-Olympiada road north of the Olympias deposit. This outcrop displays the relationship of S_1 foliation defined by compositional layering reworked into a tight F_2 fold. A ptygmatically folded pegmatite dike is also evident. Subhorizontal axial planar S_2 cleavage and crosscutting subvertical S_3 cleavage are illustrated and shown in detail in (G). (B) Metapelitic lithology within the Vertiskos unit in the Skouries area displaying a pronounced S_2 crenulation cleavage associated with parasitic F_2 folds. (C) Tight F_2 folds in quartz-rich biotite gneiss belonging to the Vertiskos unit exposed south of the Piavitsa prospect. (D) Tight F_2 folds in a granite gneiss sill located within the immediate footwall of the Stratoni fault zone east of Stratoni. A shallow S-dipping axial plane is implied. Field of view is approximately 10 m. (E) Outcrop exhibiting S_1-S_2 foliation intersections and the resulting L_2 intersection lineation developed within the Kerdilion marble north of the Olympias deposit. (F) L_2 intersection lineations developed in quartz-rich micaceous schist of the Vertiskos unit in the Skouries area. (G) Close-up of image (A) showing the relationship of steeply dipping S_3 pressure solution cleavages with subhorizontal S_2 axial planar cleavage. (H) Kink fold warping S_1 foliation in quartz-rich biotite gneiss in the Skouries area.

axial planes (Fig. 4C, D). In the northern domain, F_2 folds in outcrop verge either northeast or southwest and uniformly plunge gently south-southeast to east-southeast (Fig. 3G, H). S_1 foliation poles from the Olympias area form a well-developed girdle distribution that defines a shallow SE-plunging F_2 fold hinge (Fig. 3A) subparallel to the plunge of F_2 folds (Fig. 3H). Field relationships and a bimodal distribution of S_1 foliation poles defining fold limbs within the footwall of the Stratoni fault zone define an upright and shallow ESE-plunging F_2 antiform (Fig. 3B; Nebel et al., 1991; Gilg, 1993; Gilg and Frei, 1994; Haines, 1998). Axial planes of parasitic F_2 folds mostly dip shallowly to the south (Fig. 3G). In the southern domain, outcrop patterns and S_1 foliation poles show a bimodal distribution that defines a NW-SE–striking F_2 antiform exhibiting an open geometry with a steep SSW-dipping axial plane that plunges shallowly to the east-southeast (Fig. 3D). Parasitic F_2 folds display axial planes that mostly dip to the south-southwest on the southern limb with a minor population of steep NNE-dipping axial planes on the northern limb (Fig. 3I). Previous identification of this district-scale fold as a major synform (e.g., Frei, 1995) is not supported by field observations in this study.

A pronounced L_2 lineation resulting from the intersection of S_1 foliation with S_2 cleavage is evident in the marbles north of the Olympias deposit (Fig. 4E). This linear fabric forms on S_2 cleavage planes and plunges gently to the southeast (Fig. 3K), subparallel to the orientation of F_2 fold axes. Within the southern domain, L_2 intersection lineations are commonly developed in metapelitic units (Fig. 4F) and similarly result from the intersection of S_1 foliation and S_2 axial planar cleavage. L_2 intersection lineations in the southern domain also plunge shallowly to the southeast (Fig. 3L).

D_3 deformation: A widely spaced NW-striking S_3 fabric occurs in both northern and southern domains (Fig. 4G). This low-strain fabric forms as a steep NE- or SW-dipping pressure solution cleavage in marble or manifests as thin cleavage domains that discretely warp S_1 and S_2 foliation in metapelitic layers but may also occur as anastomosing fractures in mica-poor granitic gneiss. S_3 foliation is best developed in marbles north of the Olympias deposit and within the metapelitic lithologic units within the southern domain (Fig. 3M, N). Locally persistent kink-style folds are evident in the Skouries area and are likely associated with the D_3 deformation event (Fig. 4H).

Mylonitic shear zones: Moderate- to shallow-dipping ductile mylonitic to protomylonitic shear zones commonly exploit pegmatite and fine-grained granite dikes and sills (referred to as aplite in the mine terminology) that are exposed underground in the Madem Lakkos mine (Haines, 1998) and in the Olympias deposit. These shear zones postdate peak metamorphic fabrics (S_1, S_2) and have an associated greenschist-facies mineral assemblage of fine-grained muscovite-chlorite. Mylonites exhibit kinematic criteria that imply at least two phases of ductile shear associated with an older contraction and a younger extensional event. The latter is described in context of the Olympias area and Stratoni fault zone in the following sections.

At the Madem Lakkos mine, a S-dipping 1.5-m-wide mylonitic shear zone occurs approximately 200 m into the footwall of the Stratoni fault zone and is hosted by a pegmatitic sill at the contact between marble and amphibolite (Haines, 1998). Asymmetric S-C fabrics, isoclinal intrafolial folds, and drag folds at the shear zone margin document reverse top-to-the-north-northeast sense of shear (Haines, 1998). Folded and boudinaged marble and mylonitized granite gneiss are thrust imbricated toward the north-northeast, implying that the fold and boudinage event predated or was outlasted by mylonitic reverse faulting. Mylonitization at lower amphibolite- to upper greenschist-facies metamorphic conditions is inferred by Haines (1998) based on mineralogy and ductile deformation textures. Rare mylonitic shear zones exhibiting similar characteristics and reverse top-to-the-northeast sense of shear also occur in the Olympias area, although their respective timing is uncertain.

Olympias Area

The Olympias deposit lies 1 km west of the village of Olympiada and approximately 6 km north of the Stratoni fault zone (Fig. 2). Previous studies on the Olympias deposit have principally described ore mineralogy and the physiochemical conditions of ore deposition (Kalogeropoulos et al., 1989; Kilias et al., 1996), with a limited number of unpublished consulting reports focused on describing the structural framework of the deposit. This section presents a revised deposit-scale geologic map and cross section (Fig. 5A, B) with detailed descriptions of ductile and brittle structures combined with kinematic analyses of major faults within the Olympias area.

The Olympias deposit

The Olympias orebodies consist of massive sulfide and silicified cataclastic breccias hosted by a less than 150-m-thick marble unit that is conformably interlayered within a body of garnet-bearing quartzofeldspathic biotite gneiss of the Kerdilion unit. The marble layer is similar to the marble horizon that hosts the Madem Lakkos and Mavres Petres deposits (Kalogeropoulos et al., 1989; Gilg, 1993; Kilias et al., 1996). Ore mineralogy consists of sphalerite-galena–dominant massive sulfide that grades into pyrite-rich intervals with variable amounts of arsenopyrite and trace chalcopyrite (Fig. 6A, B). Massive to banded Ag-Zn-Pb sulfide ore locally transitions into Au-rich arsenopyrite-bearing sulfide and arsenopyrite-boulangerite–bearing silicified breccia ore types, with diffuse zones of disseminated pyrite and arsenopyrite associated with quartz-rhodochrosite ± rhodonite alteration of the surrounding wall rock. Auriferous arsenopyrite lenses and silicified breccias containing rhodochrosite-rhodonite mostly occur in the upper northern portions of the Olympias deposit and generally crosscut the massive sulfide where both ore types occur together. Mineralized breccias include those containing a chalcedonic quartz- or carbonate-dominated matrix with sulfide minerals and younger cataclastic breccias where the matrix consists of comminuted sulfide grains.

Sulfide bodies occur as coarse-grained lenses of compositionally banded sulfide that have discordant and crosscutting contacts with respect to marble and S_1 foliation (Kalogeropoulos et al., 1989; Kilias et al., 1996; Siron et al., 2016). Orebodies commonly display internal banding that locally mimics folded marble layers (Kalogeropoulos et al., 1989). Sulfide intervals that appear folded are largely unstrained and therefore interpreted to have formed from the pseudomorphic replacement of preexisting F_2 folds (Siron et al., 2016). Mine data shows that the geometry of the Olympias orebody

is strongly influenced by the morphology of the hosting marble-gneiss sequence. Individual sulfide lenses form elongate, cigar-like shapes with their long dimension oriented in a southeast direction (Veligrakis and Dalampiras, 2016). At the deposit scale, the modeled sulfide orebody plunges approximately 19° at an azimuth of 150° southeast subparallel to the mean plunge of the F_2 fold hinge and L_2 intersection lineation, as shown in Figure 3H and 3K, respectively.

Olympias sulfide ore is locally associated with a postdeformation igneous breccia within the footwall of the Kassandra fault (Fig. 6C). This breccia body is composed of granite and quartz-rhodochrosite–altered marble fragments supported by a matrix that is compositionally similar to the granite clasts (Fig. 6D). Sulfide within the matrix of the breccia suggests a close timing relationship between magmatism, brecciation, and sulfide deposition and is consistent with a magmatic-hydrothermal breccia. The timing of emplacement of this igneous body, however, was not investigated in this study and is currently unconstrained. Glomerophyric porphyry dikes that are geochemically and texturally similar to the early Miocene dikes that crosscut the sulfide orebody at the Madem Lakkos deposit (Gilg and Frei, 1994; Haines, 1998) and the silicified rhodochrosite replacement body at the Piavitsa prospect similarly crosscut sulfide ore at the Olympias deposit (Fig. 6E; Kalogeropoulos et al., 1989; Siron et al., 2016). Brecciated contacts locally developed at dike margins consist of angular to subrounded fragments of sericite-carbonate–altered porphyry, quartz-rhodochrosite–altered marble, and sphalerite-pyrite sulfide clasts (Fig. 6E).

Faults in the Olympias area

Carbonate replacement massive sulfide at the Olympias deposit shows a close spatial relationship with mylonitic to brittle faults in contact with the host marble unit (Fig. 5A, B; Kalogeropoulos et al., 1989). An array of shallow-dipping mylonitic to protomylonitic shear zones occur throughout the Olympias deposit and define the earliest stage of postpeak metamorphic faulting in the area. These ductile shear zones are transitional with and overprinted by younger fault phases along the NW-striking Kassandra and N-striking East faults. Each fault zone exhibits less than 100 m of normal top-to-the-northeast/east displacement based on the approximate magnitude of offset between marble and the surrounding quartzofeldspathic biotite gneiss (Fig. 5B).

Kassandra fault zone: The NE-dipping Kassandra fault zone occurs on the western margin of the Olympias deposit and exploits the lithologic contact between graphite-bearing marble and interlayered quartzofeldspathic biotite gneiss, pegmatitic granite gneiss, and amphibolite. Underground and surface drilling has delineated an anastomosing fault zone comprising a network of narrow fault strands that vary in thickness from ~1 to 20 m and are traceable for a strike length greater than 2 km (Fig. 5A). Displacement on the Kassandra fault diminishes downdip as it dissipates into minor fault strands and en echelon steps, which coincide with sulfide orebodies in the central parts of the Olympias deposit (Fig. 5B).

Ultramylonitic to protomylonitic shear zones, hereafter referred to as mylonites, are associated with the Kassandra fault and define the earliest stage of fault deformation in the Olympias area. Mylonites generally occur as shallow-dipping, less than 1-m-wide shear zones that are typically localized within pegmatite sills and dikes and are focused along the upper parts of the main marble unit (Fig. 5B). Mylonites commonly occur subparallel to the local S_1 foliation at the downdip terminus of the Kassandra fault and central to the Olympias deposit (Fig. 5B). Deformation textures developed within the pegmatite-hosted mylonites consist of rotated feldspar porphyroclasts that are enclosed by a fine-grained to aphanitic matrix of dynamically recrystallized quartz (Fig. 7A), whereas those developed in marble display a pronounced shear fabric with thin, laminar carbonaceous pressure solution seams defining slip surfaces. Mylonites generally exhibit a muscovite-chlorite-carbonate mineral assemblage, suggesting formation under greenschist-facies temperature conditions (Fig. 7B). Mylonitic shear zones are laterally transitional with and commonly superimposed by semibrittle shear zones. Undeformed replacement-style sulfide and mineralized silicified breccias locally overprint older mylonitic shear zones and typically display sharp and discordant contacts with respect to the tectonic fabric (Fig. 7C).

Foliated, semibrittle shear zones that developed within quartzofeldspathic biotite gneiss within the Kassandra fault (Fig. 7D) are polymict and clast supported, containing subrounded fragments of the host lithology and pegmatitic granite gneiss. The shear fabric is typically fine grained with foliated domains consisting of pale-green hydrothermal muscovite-dolomite-quartz and disseminated pyrite with variable amounts of euhedral arsenopyrite (Fig. 7E). Semibrittle faults developed in marble are monomict, containing corroded and rotated clasts in between carbonaceous pressure solution fabrics. These shear zones are accompanied by base metal sulfides, which in part define the tectonic fabric. Mineralized semibrittle faults may become overprinted by younger cataclastic breccias and fault gouge. Silicified cataclastic breccias within the Kassandra fault commonly contain disseminated pyrite ± galena-sphalerite-arsenopyrite or may be composed of a sulfide-dominated matrix resulting from the comminution of preexisting sulfide layers (Fig. 7F). These mineralized breccias are also spatially associated with quartz-rhodochrosite ± rhodonite veins.

East fault zone: Surface mapping and underground drill holes from the eastern portion of the Olympias deposit define the 5- to 20-m-wide East fault zone with a north-south strike extent greater than 1 km (Fig. 5B). Mylonites generally occur in the footwall of the East fault but are less abundant than in the Kassandra fault area to the west. Foliated, semibrittle shear zones and silicified cataclastic breccias similarly define the East fault (Fig. 7G). NNW- to N-striking gouge-filled faults and fracture zones are pervasive within the East fault (Fig. 7H). Younger clay-altered and gouge-filled faults overprint the older mylonitic and semibrittle shear zones as well as the sulfide and silicified cataclastic breccia bodies. Postmineral faults, while recognized throughout the Olympias area and particularly evident within the East fault zone, resulted in only minor displacement of the sulfide orebodies toward the east.

Quartz-rich breccias: Silicified, chalcedonic quartz-rich breccias occur as N-S–striking fault-filled structures that crop out on the southeast margin of the Olympias deposit (Fig. 7I). These zones are commonly accompanied by quartz-rhodochrosite veins, which are typically identified by a sooty, weathered

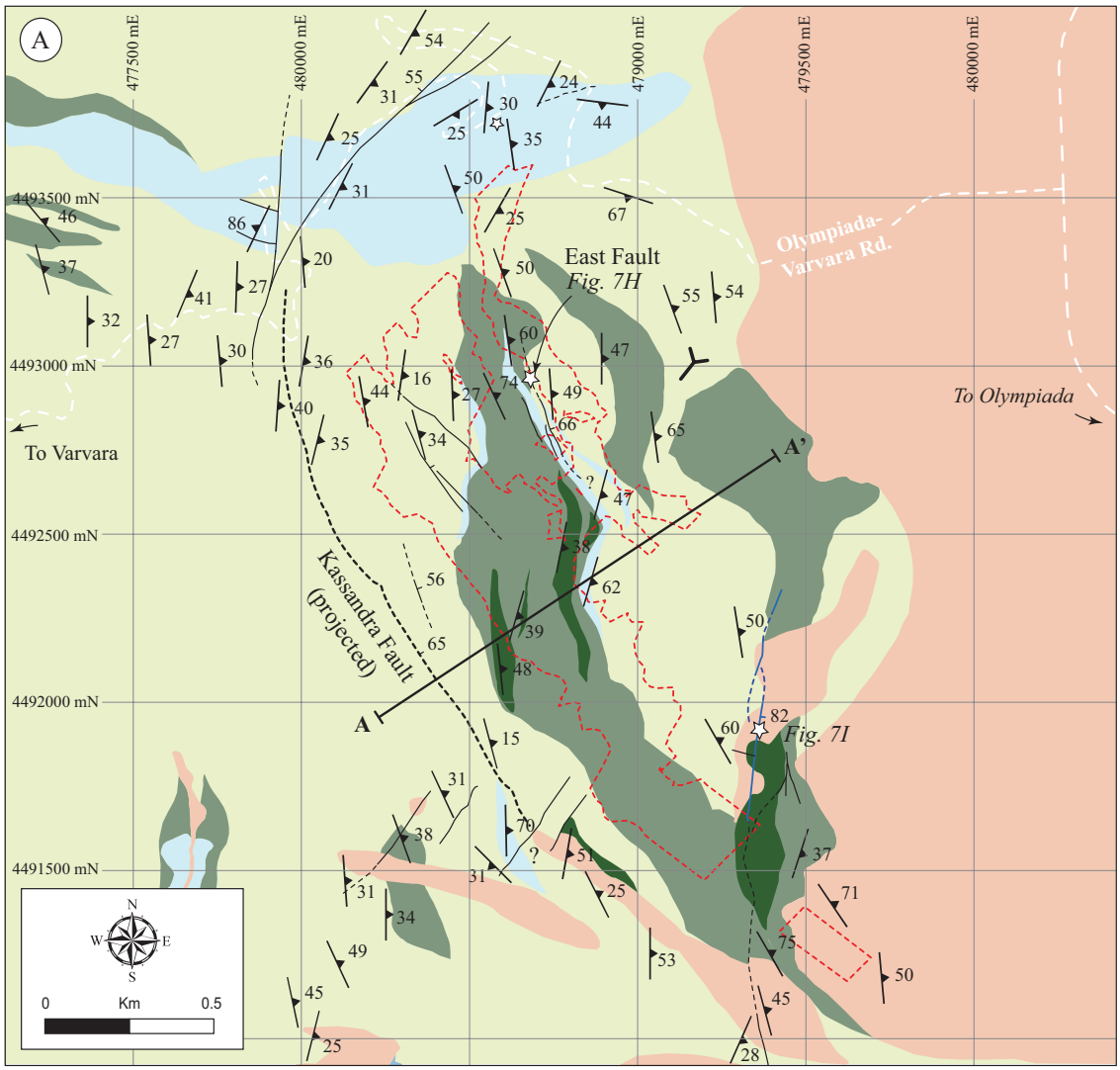

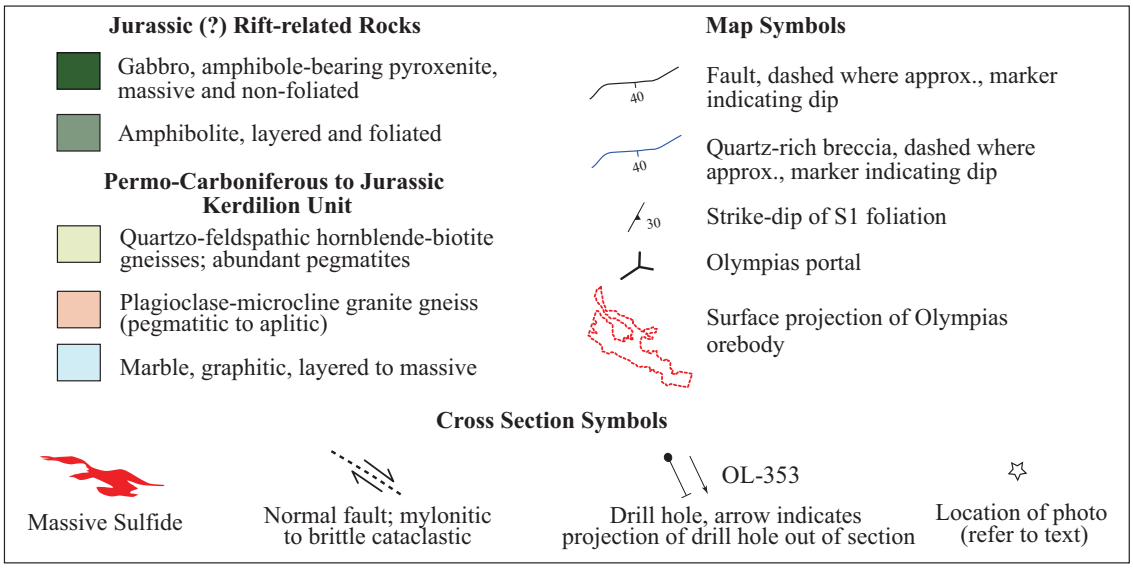

Fig. 5. (A) Detailed geologic map of the Olympias deposit area modified after Kockel et al. (1978a, b). Mapping was conducted at 1:5,000 scale and based largely on surface outcrops. (B) Cross section A-A' of the Olympias deposit is defined by underground drill core interpretation. Coordinates are displayed in the Greek Geodetic Coordinate System (GGRS 87 Greek Grid).

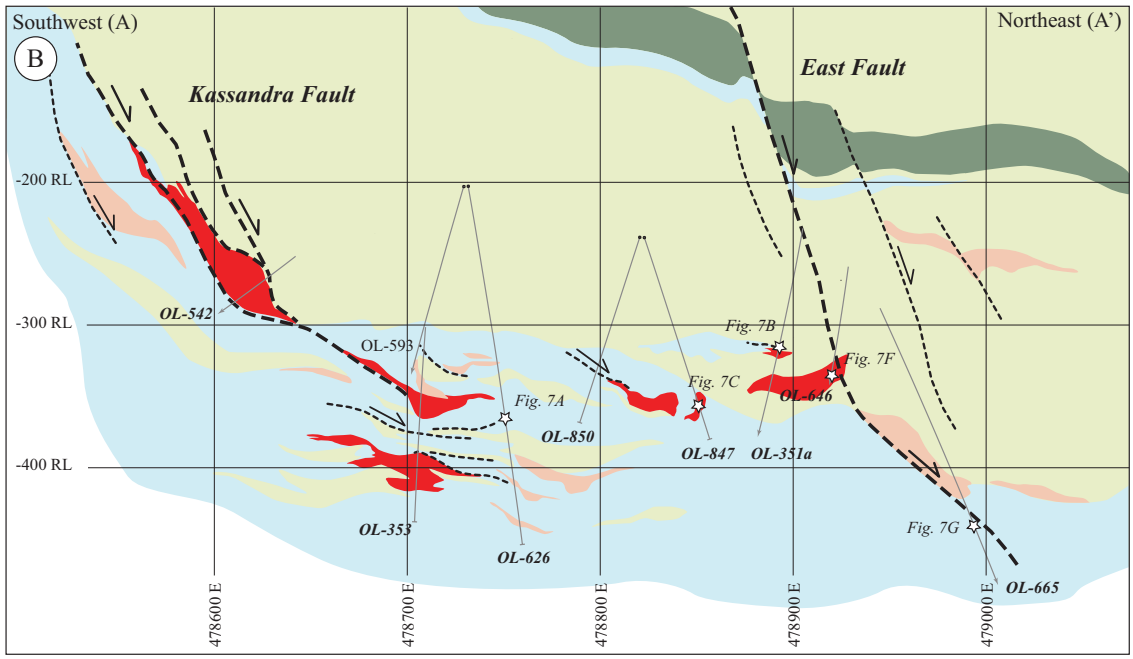

Fig. 5. *(Cont.)*

appearance with localized silicification of the adjacent metamorphic wall rock. Quartz-rich breccias are matrix supported and consist of previously sericite-altered, subangular to angular clasts of granitic gneiss that are chaotically interspersed with marble and sulfide fragments. The matrix is composed of dark-gray chalcedonic quartz containing fine-grained, disseminated euhedral pyrite and bladed arsenopyrite. Quartz-rich breccias can be Au rich, locally containing up to 19 g/t Au. The chaotic breccia texture and flinty quartz matrix is distinctive and broadly similar to the silicified breccias intercepted in drill core and adjacent to the Kassandra and East faults.

Kinematic analysis

Kinematic indictors developed within the mylonitic shear zones, where observed in drill core, imply a normal sense of shear when reoriented with respect to S_1 foliation (e.g., north-south). This is consistent with the normal eastward-displaced lithologic relationships and sense of shear on the Kassandra and East faults (Fig. 5B). An underground exposure of a mineralized segment of the Kassandra fault displays two sets of slickenlines. One set rakes obliquely across the fault surface (Fig. 7D), resulting in left-lateral displacement and a NE-directed principal axis of extension (Fig. 8A). A younger and more extensive set of slickenlines indicate normal dip-slip displacement resulting from an ENE-directed principal axis of extension (Fig. 8A). At surface, minor faults displaying centimeter-scale displacement and shear-related drag folds of S_1 foliation in quartzofeldspathic biotite gneiss are kinematically compatible with the younger set of slickenlines observed underground.

The East fault similarly displays normal top-to-the-east movement, as indicated by displaced lithologic relationships in the cross section in Figure 5B. Kinematic fault-slip data collected from surface exposures of the East fault records two generations of fault deformation superimposed on the older lithified cataclastic and mylonitic fault rocks (Fig. 8B). Slickenlines developed on a clay-altered segment of the East fault at the southern end of the Olympias deposit record oblique left-lateral displacement controlled by a NE-directed principal axis of extension (Fig. 8B). A second set of younger (?) gouge-filled faults crosscutting pegmatitic granite gneiss and quartzofeldspathic biotite gneiss display groove marks that indicate oblique right-lateral displacement controlled by an ESE-directed principal axis of extension (Fig. 8B).

Fault-slip data from auriferous fault-filled quartz-rich breccias collected on surface (Fig. 7I) exhibit near-vertical slickenlines and quartz mineral fiber growths along vein segments that imply normal movement with a minor component of either left- or right-lateral oblique slip (Fig. 8C). The shallow SE-plunging extensional strain axis corresponds to a discrete northwest-southeast extensional event that was associated with this style of mineralization in the Olympias area.

Stratoni Fault Zone

The Madem Lakkos and Mavres Petres deposits contain marble-hosted replacement Au-Ag-Zn-Pb-Cu massive to semimassive sulfide, quartz-rich disseminated Au-Ag-As-Pb-Zn-Cu sulfide, minor Cu skarn, and Au-rich quartz-rhodochrosite vein-breccia bodies, which occur throughout the Stratoni fault zone but are the dominant style of mineralization at the Piavitsa prospect. These orebodies are temporally and spatially associated with Oligo-Miocene igneous rocks and the ductile to brittle Stratoni fault zone (Fig. 9; Gilg and Frei, 1994; Haines, 1998). This section describes the sulfide deposits that occur within the Stratoni fault zone with detailed structural observations and kinematic analyses of this fault system.

Ore deposits of the Stratoni fault zone

The Madem Lakkos deposit: The Madem Lakkos deposit lies 2 km northwest of the village of Stratoni (Fig. 9) and consists

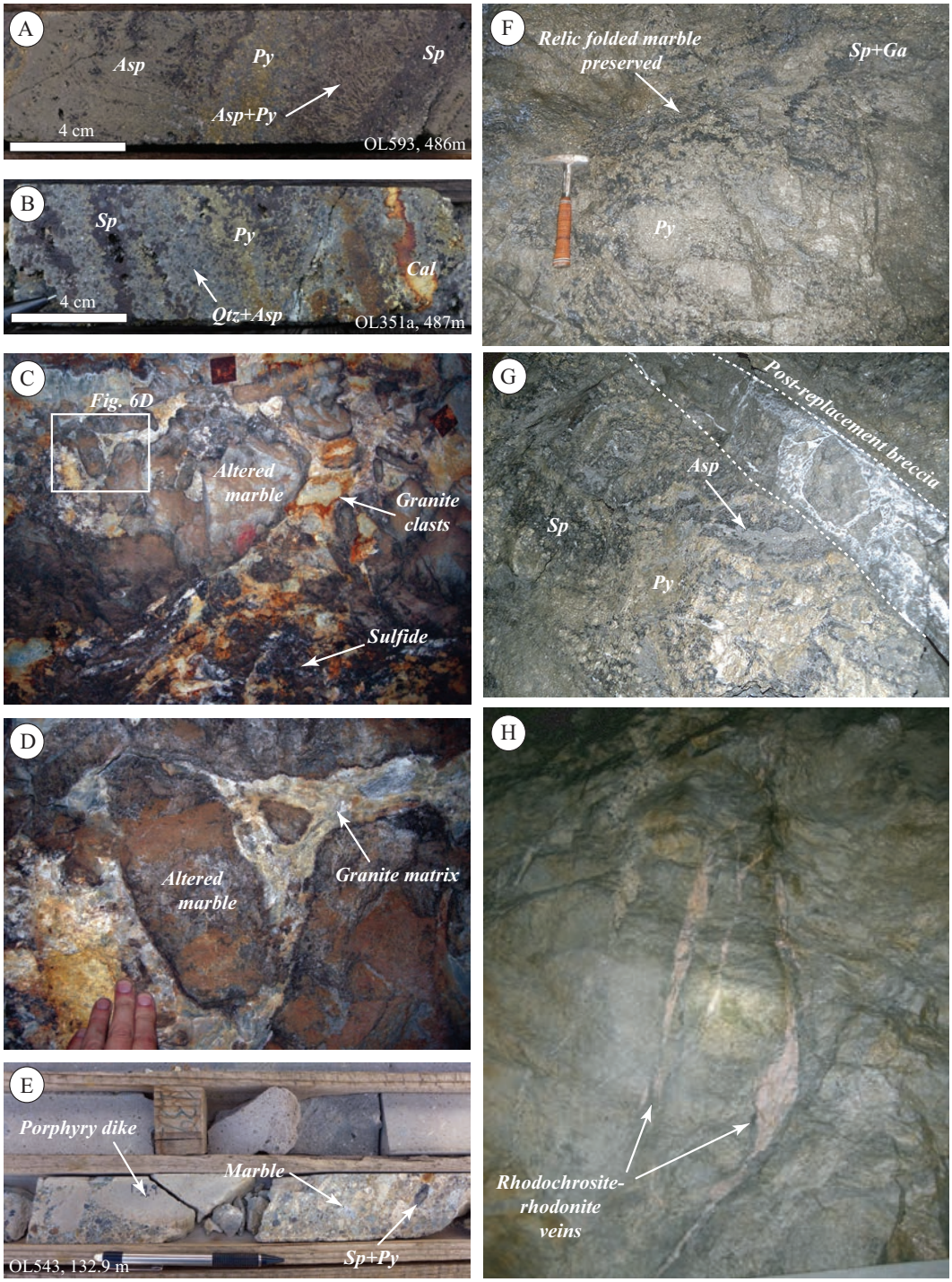

Fig. 6. Photos of representative mineralization styles and structural features from the Olympias and Mavres Petres deposits. (A-B) drill core intercepts from the Olympias deposit showing rod-textured arsenopyrite-pyrite and massive arsenopyrite replacing banded sphalerite (A) and quartz-rich, coarse-grained, and banded arsenopyrite-sphalerite-pyrite with calcite infill (B). (C) Underground exposure of igneous breccia from the –45 level at the Olympias mine. Field of view is approximately 2.5 m. (D) Close-up of image (C) showing the granitic composition of the breccia matrix. (E) Olympias drill core intercept of altered glomerophyric porphyry dike with phreatic breccia at its margins containing sulfide clasts. (F) Underground exposure of undeformed pyrite-rich massive sulfide from the Mavres Petres mine. Note the relict fold textures of the host marble preserved by the sulfide lenses. (G) Mineralized quartz-arsenopyrite-stibnite-boulangerite–bearing breccia crosscutting pyrite-sphalerite–rich massive sulfide. Stringer zones of arsenopyrite partially replace previously deposited sulfide. Image from an underground exposure at the Mavres Petres mine. Field of view is roughly 2 m. (H) NE-trending late-mineral rhodochrosite-rhodonite veins filling dilatant shear zones at the Mavres Petres mine. These veins crosscut sulfide mineralization and contain minor quantities of sulfide. Abbreviations: Asp = arsenopyrite, Cal = calcite, Ga = galena, Py = pyrite, Qtz = quartz, Sp = sphalerite.

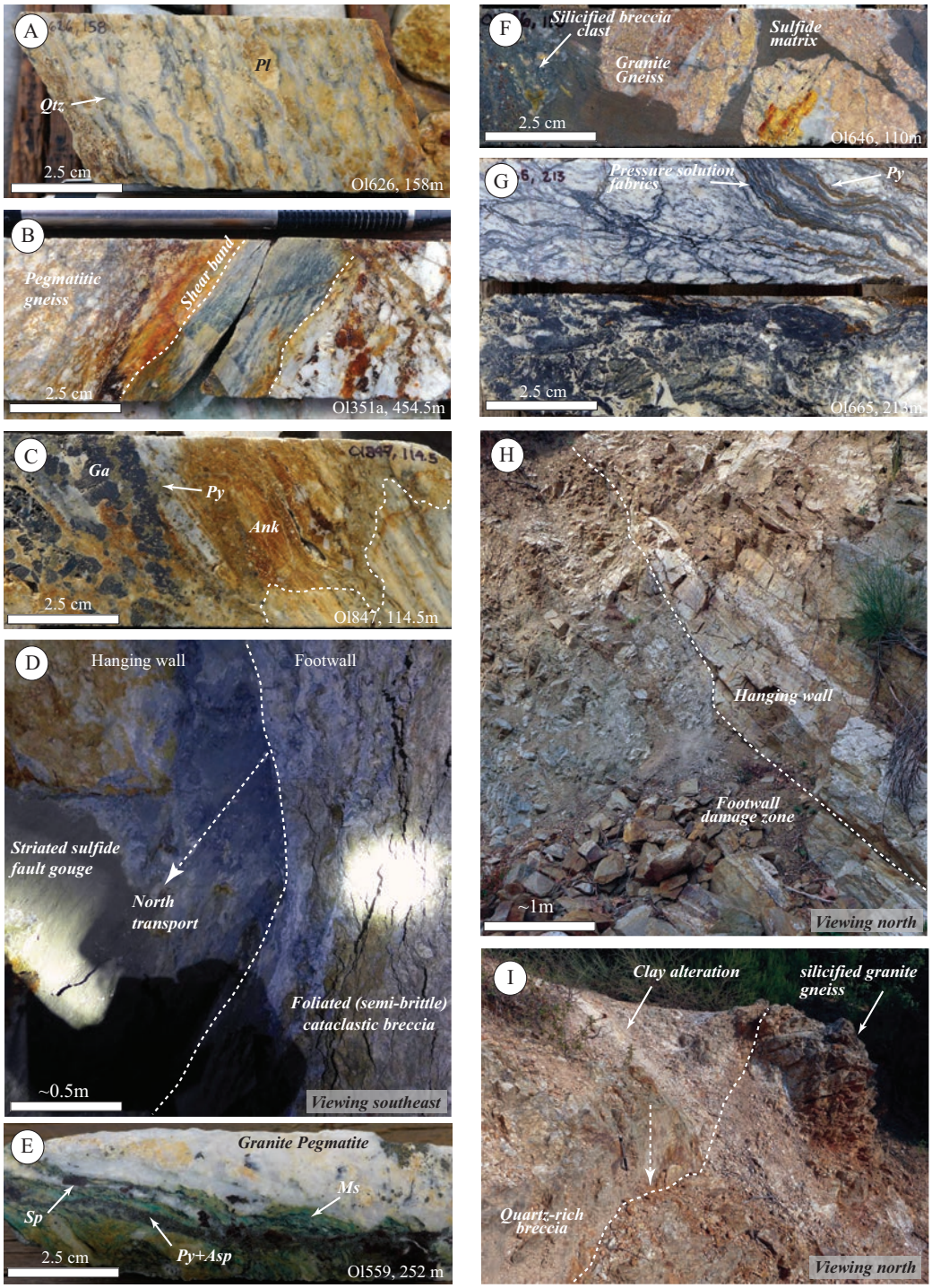

Fig. 7. Photos of representative fault styles in the Olympias deposit area. (A) Mylonitic pegmatite sill located at the base of a massive sulfide interval at the downdip terminus of the Kassandra fault. (B) Example of shear band hosted by a pegmatitic gneiss and composed of sericite-chlorite mineral assemblage. (C) Unstrained galena-pyrite semimassive sulfide and associated Fe carbonate discordantly replacing the mylonitic shear fabric in marble. (D) Underground exposure of the mineralized Kassandra fault from the –203 production level. Direction of tectonic transport is indicated by the arrow. (E) Mineralized strand of the Kassandra fault hosted in a pegmatitic granite gneiss. Note the green hydrothermal muscovite with intergrown sphalerite, pyrite, and arsenopyrite. (F) Silicified breccia containing clasts of sericite-altered granite gneiss and mineralized arsenopyrite-bearing quartz-matrix breccia, enclosed by a fine-grained and comminuted sulfide-rich matrix. (G) Foliated, semibrittle shear zone in marble containing pyrite localized along graphitic pressure solution fabrics. The lower drill core image represents a semibrittle fault overprinted by a quartz- and calcite-cemented hydrothermal breccia from the lower section of the East fault. (H) Surface exposure of the East fault with dashed line illustrating the principal slip surface. (I) Outcrop of quartz vein breccia exposed at the southeast end of the Olympias deposit. Direction of tectonic transport is indicated by the arrow. Abbreviations: Ank = ankerite, Asp = arsenopyrite, Ga = galena, Ms = muscovite, Pl = plagioclase, Py = pyrite, Qtz = quartz, Sp = sphalerite.

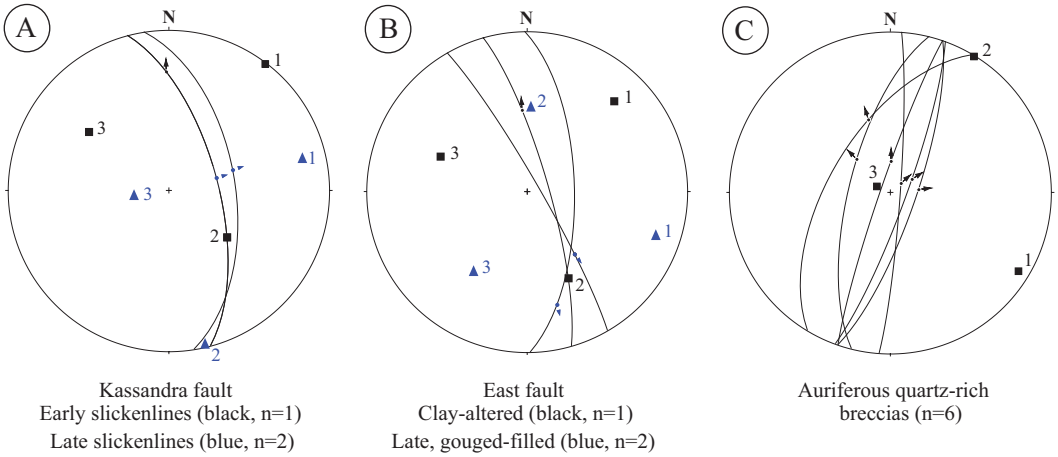

Fig. 8. Lower-hemisphere, equal-area stereographic projections of fault kinematic data from the Olympias deposit area. Fault planes and slip vectors are represented by great circles and arrows, respectively. Kinematic strain axes are plotted as squares and numbered according to the principal extension axis (1), the principal shortening axis (3), and the orthogonal intermediate axis (2). (A) Kinematic strain data from an underground exposure of the mineralized Kassandra fault is plotted as squares. The kinematic axes that describe the latest movement recorded on the Kassandra fault are represented by triangles. (B) Kinematic data from a clay-altered (late-mineral?) segment of the East fault is plotted as squares. The kinematic axes that describe the postmineral segment of the East fault are represent by triangles. (C) Fault kinematic data from outcrops of variably mineralized, auriferous quartz-rich breccias.

of skarn- and replacement-style sulfide hosted mainly within marble of the Kerdilion unit (Nebel, 1989; Nebel et al., 1991; Gilg, 1993; Gilg and Frei, 1994; Haines, 1998; Hahn, 2014; Siron et al., 2016). Unstrained sulfide ore is commonly localized at marble-granite gneiss contacts but may also occur as replacement bodies in gneiss (Haines, 1998). Previous work has shown that sulfide orebodies are spatially related to post-deformation granite dikes, referred to as aplite in the mine terminology. Orebodies are controlled by extensional faults and the closure of a prominent ESE-plunging F_2 antiform within the footwall of the Stratoni fault zone (Nebel et al., 1991; Gilg, 1993; Gilg and Frei, 1994; Haines, 1998; Siron et al., 2016).

The Madem Lakkos deposit displays a complex mineralization history involving an early phase of carbonate replacement massive sulfide, minor skarn, and a younger phase of quartz-rich sulfide mineralization. Early sulfide consists of galena-sphalerite-pyrite-pyrrhotite-arsenopyrite that forms replacement bodies displaying concordant to irregular contacts with respect to marble layers and S_1 foliation (Haines, 1998). Early sulfide ore is partially overprinted by the younger sulfide phase consisting of prismatic quartz-pyrite ± arsenopyrite-sphalerite-galena-chalcopyrite and a variety of sulfosalt minerals (e.g., boulangerite). This style of mineralization was termed disseminated sulfide in previous studies and contributed the majority of the ore mined from the Madem Lakkos deposit (Nebel et al., 1991; Gilg, 1993; Haines, 1998). Quartz-rhodochrosite ± rhodonite vein and vein breccias crosscut the sulfide orebodies (Gilg, 1993; Haines, 1998), a paragenetic relationship similar to the Olympias deposit. Volumetrically minor pyrite- and Cu-bearing calcic and magnesian skarns are present locally at surface and at depth on the eastern margin of the Madem Lakkos deposit. Skarn-related sulfide ore occurs within marble adjacent to the Vathilakkos fault (Fig. 10A) and within granitic and quartzofeldspathic biotite gneiss adjacent to the Stratoni granodiorite stock (Gilg, 1993). The timing relationship between these skarn occurrences and the carbonate replacement sulfide ores remains unclear.

Replacement orebodies in the Madem Lakkos deposit are principally restricted to the footwall of the Stratoni fault zone and are localized at ductile-brittle fault contacts and hinge zones of ESE-plunging F_2 folds associated with the Madem Lakkos antiform (Fig. 10A; Nebel, 1989; Nebel et al., 1991; Gilg, 1993; Gilg and Frei, 1994; Haines, 1998). Outcrop patterns and the distribution of S_1 foliation poles in the footwall of the Stratoni fault zone demonstrate an upright geometry and a steep SSW-dipping axial plane of the Madem Lakkos antiform (Fig. 3B). Mine data shows that ESE-plunging F_2 fold hinges in part controlled the distribution of sulfide ore within the Madem Lakkos deposit. Sulfide ore overprints thrust-related mylonitic fabrics in the Stratoni fault zone, including the younger and more extensive extensional mylonites. In the southern part of the Madem Lakkos deposit, sulfide orebodies are hosted by steeply S dipping marble lenses, which are controlled by S-dipping strands of the Stratoni fault zone (Haines, 1998).

Fine-grained to pegmatitic granitic dikes, which have localized mylonitic deformation in the footwall of the Stratoni fault, are spatially associated with replacement sulfide ore (Haines, 1998). Granitic intrusions also locally crosscut the massive sulfide orebodies and are reported to have been affected by later stages of alteration and sulfide mineralization within the Madem Lakkos deposit (Gilg, 1993; Haines, 1998). The structural, spatial, and relative timing relationships of sulfide ore with granite bodies at the Madem Lakkos deposit are broadly similar to the Olympias deposit.

The Mavres Petres deposit: The Mavres Petres carbonate replacement sulfide deposit is located ~1 km to the west of the Madem Lakkos deposit (Figs. 9, 10A). Sulfide orebodies are largely restricted to the Stratoni fault zone and are hosted

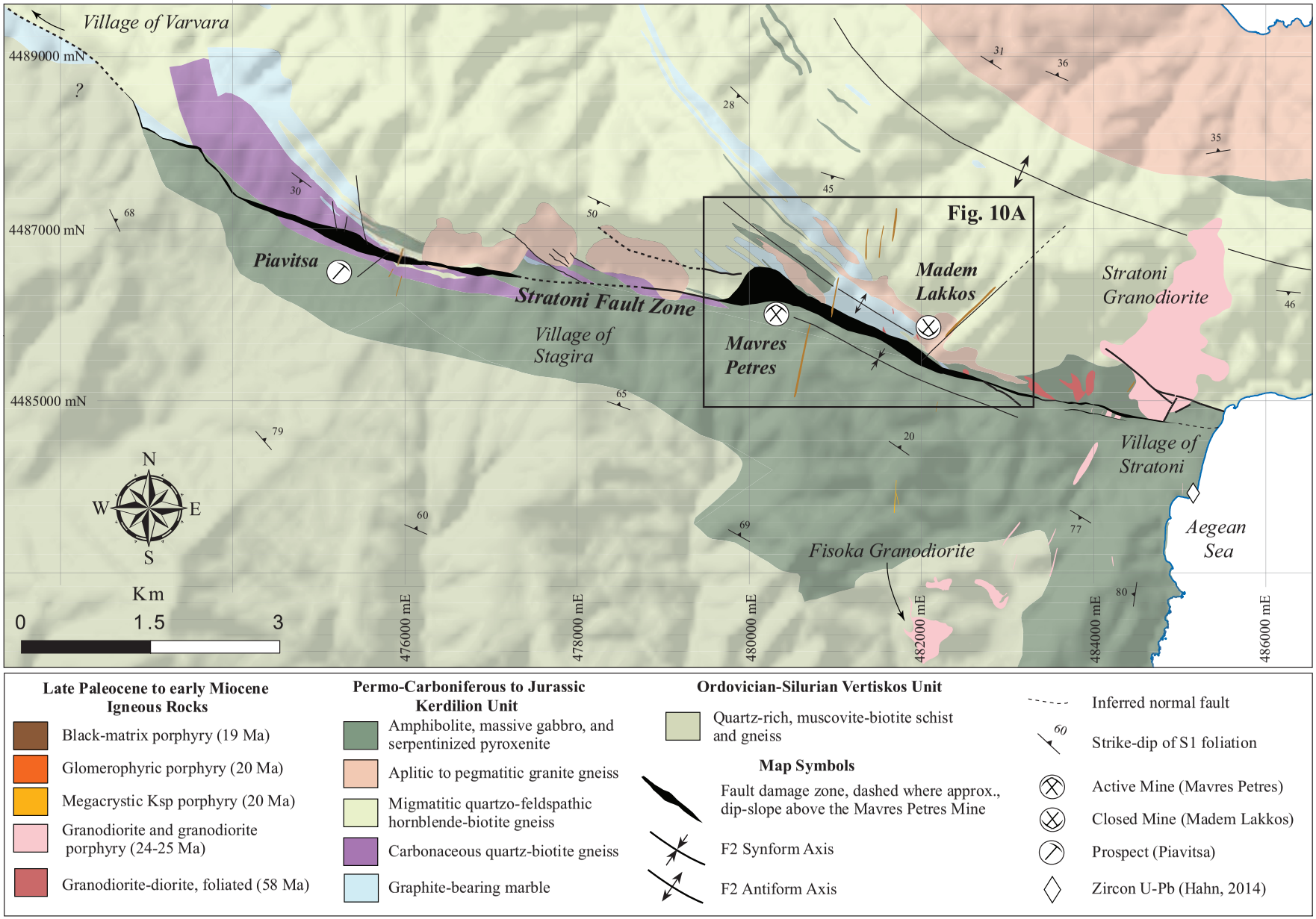

Fig. 9. Simplified geologic map of the Stratoni fault zone modified after Kockel et al. (1978a, b). The inset map is located in Figure 10A. The thick black line in the Mavres Petres area corresponds to the dip-slope exposures of the Stratoni fault zone. Coordinates are displayed in the Greek Geodetic Coordinate System (GGRS 87 Greek Grid). Abbreviations: Ksp = K-feldspar.

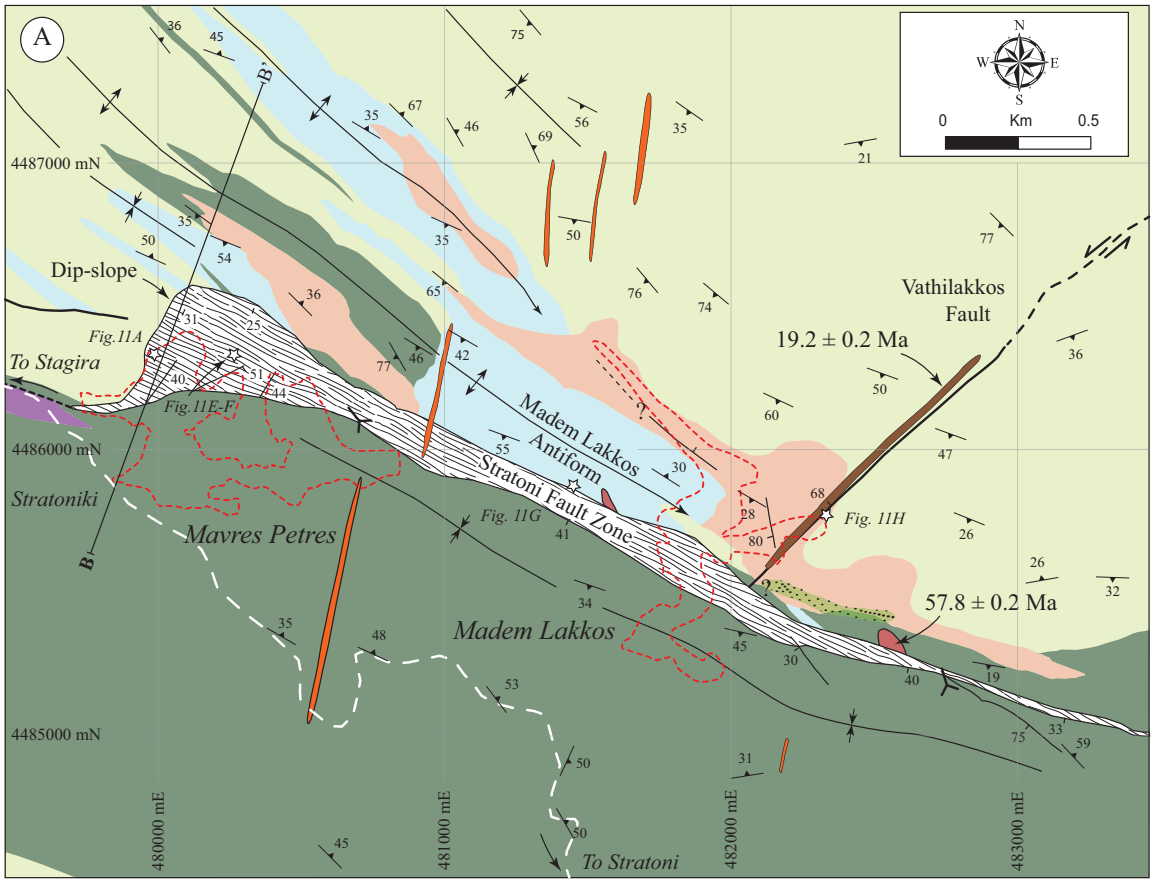

Igneous Rocks

- Black-matrix porphyry dike (19.2 Ma; Siron et al., 2016)
- Glomerophyric porphyry (~20 Ma; Siron et al., 2016)
- Granodiorite, porphyritic and foliated (Late Paleocene to early Eocene)

Jurassic Rift-related Rocks

- Amphibolite with interlayered gabbro and amphibole-bearing pyroxenite, massive and non-foliated

Permo-Carboniferous to Jurassic Kerdilion Unit

- Quartzo-feldspathic hornblende-biotite gneisses; abundant pegmatites
- Plagioclase-microcline granite gneiss (pegmatitic to aplitic)
- Carbonaceous quartz-biotite gneiss
- Marble, graphite-bearing, layered to massive, locally recrystallized

Alteration and Mineralization

- Wollastonite-tremolite-epidote ± pyrite skarn
- Massive sulfide (cross section)

Map and Cross Section Symbols

- Mylonitic to semi-brittle, and brittle cataclasite (Stratoni fault zone)
- Fault, dashed where approx., marker indicating dip
- Antiform axis indicating plunge direction
- Synform axis indicating plunge direction
- Strike-dip of S1 foliation (plan view)
- Strike-dip of S1 foliation (cross section)
- Underground portal
- Location of photo (refer to text)
- Surface projection of orebody

Fig. 10. (A) Detailed geologic map of the Madem Lakkos and Mavres Petres deposits. Mapping was conducted at 1:5,000 scale and based largely on surface outcrops. (B) Cross section B-B' of the Mavres Petres deposit defined by surface mapping and underground drill core. Inferred displacement on the Stratoni fault zone is shown by offset marble as indicated by dashed lines. Coordinates are displayed in the Greek Geodetic Coordinate System (GGRS 87 Greek Grid).

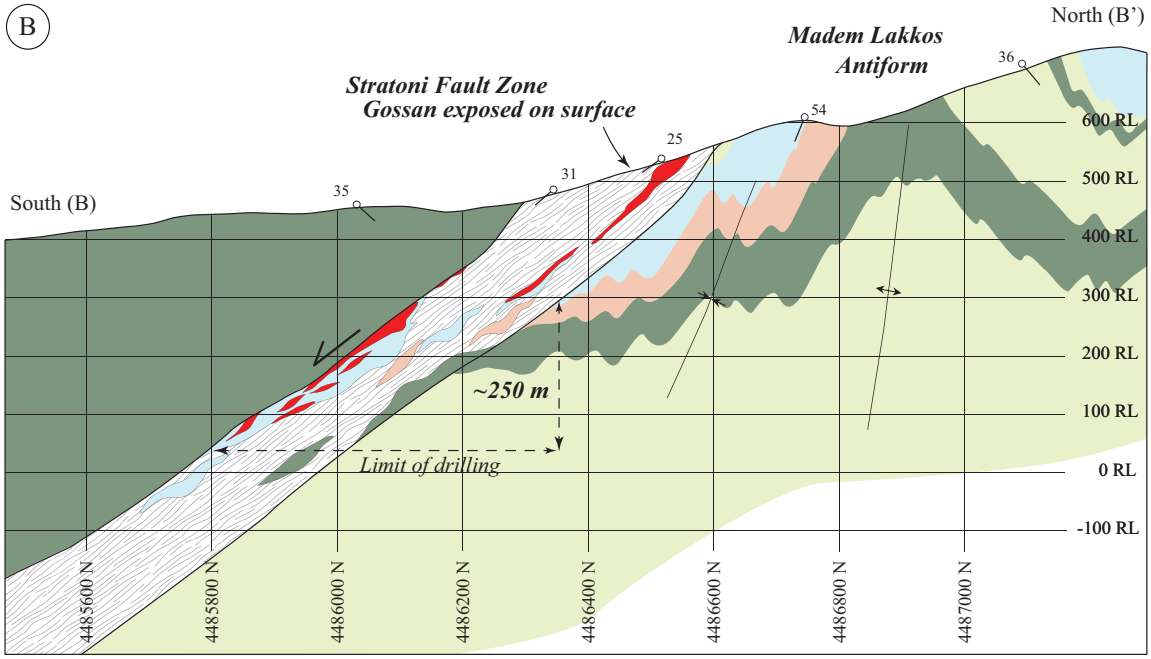

Fig. 10. *(Cont.)*

by marble lenses that are complexly imbricated with graphite-bearing quartz-biotite gneiss and schists, granite gneiss, and amphibolite. The marble unit is interpreted to be equivalent to the marble that hosts the Madem Lakkos and Olympias deposits (Kalogeropoulos et al., 1989). As currently known, the Mavres Petres deposit has a strike length greater than 1 km and a downdip extent exceeding 700 m from surface and forms semicontinuous sulfide replacement bodies that mantle and fully replace marble lenses between strands of the Stratoni fault on the southwest limb of the Madem Lakkos antiform (Fig. 10B). Sulfide textures and mineralogy are similar to Madem Lakkos and the Olympias deposits. Silicified Fe-Mn oxide gossans and pods of massive sulfide form the surface expression of the deposit on the exposed dip-slope segment of the Stratoni fault zone above the village of Stratoniki (Fig. 10A) in an area that was the focus of ancient mining (Sagui, 1928).

The Mavres Petres sulfide ores consist of massive to banded, coarse-grained pyrite-sphalerite-galena accompanied by minor accessory arsenopyrite-stibnite and trace chalcopyrite (Fig. 6F). Pyrite-sphalerite–dominant massive sulfide is compositionally gradational with domains of massive arsenopyrite in the western sector of the orebody. Bladed pyrite occurring within sphalerite-rich banded sulfide is developed locally and resembles the rod-textured pyrite that occurs in the Olympias orebody (Siron et al., 2016). Younger cataclastic breccias related to mineralized strands of the Stratoni fault zone locally crosscut sulfide ore (Fig. 6G). Quartz-rich sulfide pods and silicified breccias containing fibrous to acicular boulangerite and arsenopyrite occur in close association with quartz-rhodochrosite veins (Fig. 6H) and vein breccias, which commonly exhibit elevated Au grades. Both silicified breccias and quartz-rhodochrosite vein breccias overprint the sulfide orebodies, demonstrating similar textural relationships and paragenesis to the Madem Lakkos and Olympias deposits.

The Piavitsa prospect: The Piavitsa prospect occurs 3 km west of the Mavres Petres deposit within the Stratoni fault zone (Fig. 9). Carbonate replacement semimassive sulfide with more extensive Au-bearing quartz-rhodochrosite vein breccias occur in the Piavitsa area. Outcrop and drill core intercepts outline a broad WNW-striking set of faults with secondary N-striking splays that collectively define the western segment of the Stratoni fault zone. Outcropping quartz Mn-rich replacement bodies form the surface expression of discontinuous sulfide zones at depth. These sulfide bodies are largely restricted to marble lenses entrained within the Stratoni fault zone in a setting similar to the Mavres Petres deposit. Gold-bearing quartz-rhodochrosite ± rhodonite veins and vein breccias are principally hosted by hanging-wall quartz-muscovite-carbonate-pyrite–altered, graphite-bearing quartz-biotite-garnet schists, gneiss, and interlayered amphibolites. Gold mineralization is generally localized where fault splays obliquely intersect major strands of the Stratoni fault zone. Quartz-rhodochrosite veins intercepted in drill core locally exhibit a crustiform texture and commonly contain disseminated pyrite ± galena-sphalerite-arsenopyrite-boulangerite, similar to veins in the upper parts of the Olympias and Mavres Petres deposits. Widely spaced veins, similar in mineralogy and texture to those in drill core, occur ~2 km south of the Piavitsa prospect in association with steep W- and E-dipping faults, which accommodate centimeter-scale normal displacement as indicated by offset compositional layers within the gneiss sequence.

Previous tectonic interpretations of the Stratoni fault zone

The area that defines the Stratoni fault zone has been viewed as the tectonic boundary between the Rhodope Kerdilion unit and the Serbo-Macedonian Vertiskos unit (Kockel et al., 1977). Burg et al. (1995, 1996) interpreted the Kerdilion-Vertiskos contact as a S-verging thrust fault, whereas Kounov et

al. (2015) shows this boundary as the southeastern extension of the Kerdilion detachment fault, which controlled exhumation of the southern Rhodope core complex (e.g., Brun and Sokoutis, 2007). Zircon U-Pb ages from the metamorphic basement rocks (Hahn, 2014) with structural and geochemical data from this study challenge these previous interpretations.

Middle Jurassic amphibolites (Hahn, 2014) of ophiolitic origins that occur to the north in the footwall and to the south in the hanging wall of the Stratoni fault zone (Fig. 9) exhibit similar structural patterns. Principal component analysis of immobile elements indicates that the amphibolites to the north and south of the Stratoni fault zone are chemically indistinguishable and therefore have a common origin (see Appendix for details). The geochronological, structural, and geochemical data imply that the amphibolites were tectonically emplaced into the Kerdilion unit by at least the Middle Jurassic either during terrane assembly or after accretion and were later crosscut by normal faults that make up the Stratoni fault zone. The boundary separating the Kerdilion and Vertiskos units in the Kassandra mining district is therefore not defined by a middle Eocene detachment fault as suggested by Haines (1998) and inferred by Kounov et al. (2015) but rather by an older structure. The terrane-bounding structure separating the Kerdilion and Vertiskos units and the tectonic control that imbricated the ophiolitic rocks, however, is currently undefined within the district.

The Stratoni fault zone

The strongly mineralized and S-dipping Stratoni fault zone is a continuous mylonitic to brittle fault zone exceeding 12 km in strike length, extending from the Aegean coast at Stratoni to the village of Varvara in the west (Fig. 9). Marble lenses entrained within the Stratoni fault zone are separated from their likely footwall equivalents by a minimum of 250 m at the Mavres Petres deposit based on drill core data and cross-section interpretation (Fig. 10B). An inflection in the strike direction of the Stratoni fault zone in the Mavres Petres area reflects the linkage between two individual fault segments (Fig. 9). Underground exploration drill holes within the Mavres Petres mine confirm the western continuation of the Stratoni fault zone as it passes unexposed through the village of Stagira (Fig. 9). The fault zone is dominated by strongly carbonaceous rocks toward the west where it is intermittently exposed at surface in the Piavitsa prospect area and becomes less evident to the northwest where it likely diminishes near the village of Varvara (Fig. 9).

In general, the Stratoni fault zone separates quartzofeldspathic biotite gneiss, granite gneiss, marble, and minor amphibolite in the north from amphibolite-dominant units to the south. The fault zone also crosscuts the lower portion of the late Oligocene (25.4 ± 0.2 Ma) Stratoni granodiorite stock in the east (Fig. 9; Siron et al., 2016). Graphitic quartz-biotite gneiss and schist lay structurally above quartzofeldspathic biotite gneiss and both are gradationally interlayered with marbles and thin amphibolite units. Fault strands preferentially exploit this graphite-bearing layer, particularly within the Mavres Petres and Piavitsa areas. Residual carbonaceous material is localized along pressure solution seams (Fig. 11A, B) and is spatially associated with the hydrothermal alteration of amphibole, biotite, feldspar, and garnet to muscovite and chlorite within the damage zone. Carbonaceous material derived from the graphite-bearing quartz-biotite layer and marble is concentrated in areas where deformation and alteration is most intense.

Internal structure of the Stratoni fault zone: The Stratoni fault zone contains slivers of amphibolite, marble, quartzofeldspathic biotite gneiss, granite gneiss, and graphite-bearing quartz-biotite schists in the polyphase damage zone that consists of multiple anastomosing fault strands ranging from several tens of meters to locally in excess of 100 m in width. The SSW-dipping ductile mylonitic shear zones that define the earliest stage of extension within the Madem Lakkos deposit exhibit textures and relative timing relationships consistent with syn- to postpeak metamorphism. Kinematic indicators including asymmetric S-C fabric, quartz ribbons, and recrystallized feldspar subgrains associated with strain-related myrmekites and a biotite-hornblende shear fabric imply formation within an extensional stress field at lower amphibolite-facies metamorphic conditions (Haines, 1998). These mylonitic shear zones are extensively overprinted by broad deformation zones exhibiting pressure solution fabrics, which show the development of phyllonitic cleavage defined by residual carbonaceous material, muscovite, and chlorite. Drag folds that warp S_1 and S_2 foliation into near parallelism with the shear zone indicate a component of ductile strain, whereas the area between individual fault strands is commonly disrupted by fracturing and brecciation, reflecting more brittle styles of deformation.

Overprinting relationships record progressively younger increments of extensional strain. Semibrittle shear zones are enriched with carbonaceous material and commonly have a variably silicified fault gouge matrix that contains subrounded, asymmetrically rotated clasts of marble, amphibolite, and pegmatitic to aplitic granite gneiss (Fig. 11C). Mineralized fault strands are generally altered to a mineral assemblage consisting of hydrothermal muscovite, Fe- and Mg-rich carbonate, and fine-grained pyrite ± galena-sphalerite-arsenopyrite (Fig. 11D). Individual shear zones commonly contain asymmetric fault-related shear folds exhibiting an isoclinal geometry with S-dipping axial planes (Fig. 11E). Second-order Riedel shear fractures occur as an array of synthetic faults that overprint and internally displace previously developed shear fabric (Fig. 11F). Semibrittle shear zones and spatially associated sulfide lenses are locally overprinted by fault-hosted veins and clast-supported cataclastic fault breccias containing subangular to angular fault-rock fragments cemented by hydrothermal rhodochrosite ± rhodonite. These breccias may transition laterally into quartz-rhodochrosite ± rhodonite veins as recognized at the Mavres Petres deposit and the Piavitsa prospect (Siron et al., 2016).

Fault-slip surfaces that are late with respect to semibrittle faults and the sulfide bodies form a complex anastomosing fault network internal to the Stratoni fault zone. Late- to postmineral faults typically strike oblique to the previously developed shear fabric but in general have not accommodated sufficient strain to completely displace principal fault strands. A prominent postmineral fault surface crops out in marble above the Madem Lakkos mine and displays a corrugated fault surface with microbreccia striations consisting of angular to subangular marble fragments supported by a

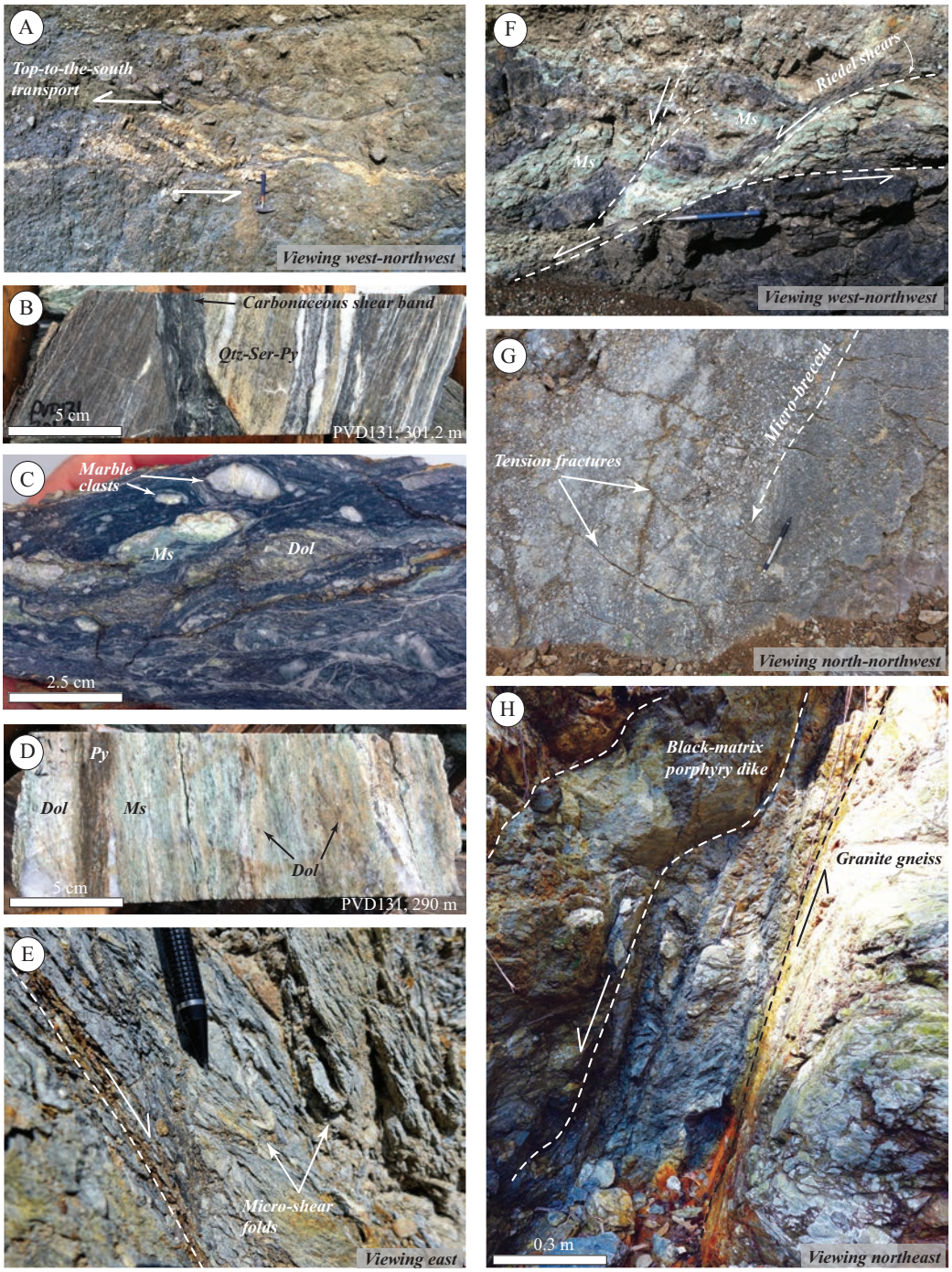

Fig. 11. Photos of representative fault styles from the Stratoni fault zone. (A) Outcrop of the ductile-brittle Stratoni fault zone above the Mavres Petres deposit. Sense of shear is normal and top-to-the-south. (B) Drill core intercept from the Piavitsa prospect of graphite-bearing quartz-biotite gneiss crosscut by a semibrittle carbonaceous shear band bounding quartz-sericite-carbonate-pyrite alteration. (C) Foliated, semibrittle fault showing well-developed pressure solution fabrics within a silicified carbonaceous matrix intergrown with pyrite, dolomite, and crystalline hydrothermal muscovite. Sense of shear is top-to-the-left. (D) Drill core intercept from the Piavitsa prospect showing typical pale-green muscovite, dolomite, and pyrite alteration replacing graphitic quartz-biotite-garnet gneiss adjacent to a mineralized strand of the Stratoni fault zone. (E) Microshear folds contained within a major strand of the Stratoni fault zone showing normal sense of shear to the south. Image taken from an outcrop above the Mavres Petres deposit. (F) Same outcrop of Stratoni fault zone exhibiting synthetic Riedel shears that crosscut the shear fabric and demonstrate normal southward sense of shear. The pale-green mineral is hydrothermal muscovite. (G) Outcrop of the postmineral segment of the Stratoni fault zone above the Madem Lakkos deposit. Microbreccia streaks and tension fractures developed on the fault surface indicate normal sense of shear in a southwest direction. (H) Outcrop of the Vathilakkos fault showing the faulted contact between granite gneiss to the east and an early Miocene black-matrix porphyry dike to the west. Abbreviations: Dol = dolomite, Ms = muscovite, Py = pyrite, Qtz = quartz, Ser = sericite.

fine-grained carbonate groundmass (Fig. 11G). Similar brittle faults associated with incremental amounts of displacement are reported to crosscut the Madem Lakkos massive sulfide orebody (Haines, 1998) and occur in underground exposures at the Mavres Petres deposit.

Neotectonic activity within the Stratoni fault zone has produced a topographically pronounced range front with distinct S-facing triangular facets (Michailidou et al., 2005). Fault surfaces commonly occupy areas of previous fault deformation and are typified by moderate to steep S-dipping fracture arrays and polished slip surfaces. In the Stratoni area, these fault surfaces are encrusted by a clast-supported breccia carapace consisting of hydrothermally altered and sulfide-bearing metamorphic wall rock and late Oligocene feldspar porphyry dike fragments that are cemented by a ferruginous matrix. These iron-rich scabs are interpreted to be ferricrete breccias that formed by weathering of sulfide-rich rock. Neotectonic faults exposed underground and intercepted in drill core manifest as narrow fault surfaces or gouge-rich zones that crosscut sulfide ore and are superimposed on all previous strain features.

Faults intersecting and oblique to the Stratoni fault zone: Numerous faults merge into or intersect the Stratoni fault zone and are observed in surface outcrops and within underground exposures. The most notable of these structures is the NW-dipping Vathilakkos fault (Fig. 10A). This structure is about a 1-m-wide network of fractures and gouge-filled brittle faults cropping out above and within the Madem Lakkos mine (Fig. 11H). The Vathilakkos fault extends for approximately 2 km to the northeast of the Stratoni fault zone as determined from drill core and surface traces. The intersection of the Vathilakkos fault with the Stratoni fault zone is not exposed, but Haines (1998) describes apparent right-lateral displacement of the Madem Lakkos orebody related to postmineral movement on this fault. An altered glomerophyric porphyry dike and an unaltered black-matrix porphyry dike, the latter dated at 19.2 ± 0.2 Ma by zircon U-Pb methods (Siron et al., 2016), each occur within the Vathilakkos fault. Both dikes crosscut the Madem Lakkos orebody at depth (Nebel, 1989; Gilg and Frei, 1994; Haines, 1998). Strands of the Vathilakkos fault crosscut the black-matrix porphyry dike (Fig. 11H), indicating that movement continued after crystallization of the dike.

Kinematic analysis

The Stratoni fault zone mainly displays normal top-to-the-south-southwest sense of shear as evidenced by displaced lithologic units (Fig. 10B) and kinematic criteria (Fig. 12A). Mineralized WNW- and NNE-striking foliated, semibrittle shear zones were likely active at the same time based on textural similarities and the lack of crosscutting relationships and are therefore treated collectively in this analysis. Kinematic analyses of S-C shear fabrics and Riedel shear fractures that developed within the semibrittle shear zones reveal a bimodal fault-slip distribution that plunges to the south-southeast and south-southwest (Fig. 12A). Slip vectors developed on NNE-striking faults occur at the intersection of the two fault sets (Fig. 12A) and are interpreted to be strain compatible with the principal WNW-striking faults. While the overall heterogeneous fault-slip behavior of the semibrittle Stratoni fault zone may be explained by multiple deformation events (Marrett and Allmendinger, 1990), strain incompatibility is likely best explained by dilation and brecciation processes.

Late- to postmineral faults within the Stratoni fault zone strike oblique to synmineral semibrittle shear zones or form splays trending to the north-northwest and north-northeast. NW-plunging slickenlines on fault surfaces within the Stratoni fault zone resulted from largely compatible dextral and normal dip-slip movement (Fig. 12B). NW-plunging slickenlines are similarly recorded on a fault surface from the Gomati fault zone to the south of the Skouries deposit (Fig. 2), which also imply right-lateral displacement. These faults convey a younger extensional episode responding to an E-directed principal axis of extension (Fig. 12B). The late- to postmineral and mostly brittle Vathilakkos fault in the footwall of the Stratoni fault zone displays left-lateral displacement on a set of NE-striking brittle faults resulting from a W-directed principal axis of extension (Fig. 12C).

Younger cataclastic breccias and gouge-filled faults that overprint earlier ductile and semibrittle fabrics record increments of normal displacement that postdate carbonate replacement sulfide orebodies. Fluted (corrugated) troughs, microbreccia streaks, calcite mineral fibers, and extensional tensile fractures that developed on the fault surface (Fig. 11G) indicate normal top-to-the-southwest transport with a component of right-lateral oblique movement produced by a NE-directed principal axis of extension (Fig. 12D). The youngest faults occupying the Stratoni fault zone display slickenlines and minor groove marks, demonstrating normal top-to-the-south-southeast relative movement with a minor left-lateral strike-slip component produced by an S-directed principal axis of extension (Fig. 12E). These data agree with the kinematic axes previously reported from the neotectonic segment of the Stratoni fault zone (Fig. 12E; Pavlides and Tranos, 1991).

$^{40}Ar/^{39}Ar$ Geochronology of the Carbonate Replacement Deposits

Two samples of pale-green hydrothermal muscovite from sulfide-bearing semibrittle, phyllonitic shear zones of the Kasandra fault at the Olympias deposit and the Stratoni fault zone at Piavitsa prospect were dated using the $^{40}Ar/^{39}Ar$ technique (see Appendix for analytical methodology and data). Muscovite is spatially associated with sulfide ore at the Olympias, Madem Lakkos, and Mavres Petres deposits and the Piavitsa prospect. It occurs within and adjacent to mineralized intervals and extends into the metamorphic wall rock for no more than several meters. Structurally, these micas define the foliation in semibrittle fault strands within the Kassandra fault and the Stratoni fault zone. Quartz-carbonate ± sulfide veinlets associated with the replacement sulfide bodies crosscut but are also overprinted by mineralized shear fabrics, implying a synmineral timing to foliation and mica development. While there are general spatial, mineralogical, and structural relationships between hydrothermal muscovite with faults and sulfide, correlation with a specific style of mineralization (replacement sulfide or rhodochrosite ± rhodonite vein breccias) is not well constrained. Shortwave infrared and powder X-ray diffraction analyses indicate that the pale-green mica in the two samples investigated is muscovite.

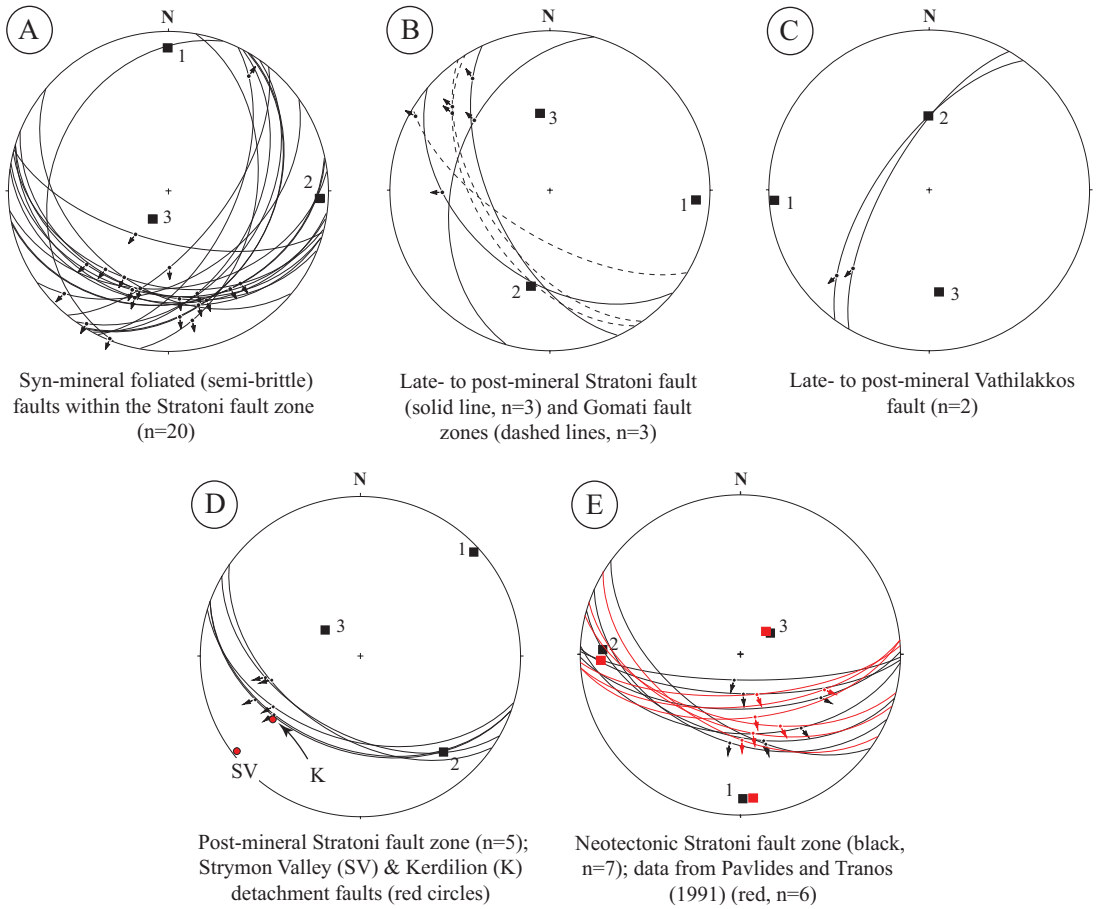

Fig. 12. Lower hemisphere, equal-area stereographic projections of fault kinematic data from the Stratoni fault zone. Fault planes and slip vectors are represented by great circles and arrows, respectively. Kinematic strain axes are plotted as squares and numbered according to the principal extension axis (1), the principal shortening axis (3), and the orthogonal intermediate axis (2). (A) Kinematic data from semibrittle and synmineral segments of the Stratoni fault zone. (B) Late- to postmineral strand of the Stratoni fault zone (solid line) and kinematically equivalent deformation from the Gomati fault zone (dashed lines). (C) Late- to postmineral Vathilakkos fault. (D) Postmineral corrugated fault segment within the Stratoni fault zone at the Madem Lakkos deposit. Kinematic criteria from the Kerdilion (K) and Strymon Valley (SV) detachment faults (Dinter, 1998) are shown as red circles for comparison. (E) Neotectonic faults within the Stratoni fault zone from this study are plotted in black with data from Pavlides and Tranos (1991) represented in red. Note the coincident position of the kinematic strain axis for each set of data.

Results

Sample OL559 (252 m) was collected from drill core, which intercepted a phyllonitic shear band crosscutting pegmatitic granite gneiss associated with the Kassandra fault at the Olympias deposit (Fig. 7E). Muscovite defines a lenticular shear fabric and forms euhedral to subhedral grains reaching 500 μm in length and is intergrown with domains of quartz-carbonate and euhedral fine-grained masses of pyrite, sphalerite, and arsenopyrite (Figs. 7E, 13A). Step-heating analysis of mica yielded an overall flat $^{40}Ar/^{39}Ar$ spectrum with a plateau age of 22.6 ± 0.3 Ma, including ~80% of total ^{39}Ar released (mean square of weighted deviates [MSWD] = 4.33; Fig. 13B). Isotopic disturbance in the initial three steps may be attributed to excess ^{40}Ar or recoil effects possibly due to a fraction of fine-grained mica within the sample. We interpret this date as the crystallization age of the mica and, by association, a minimum age of hydrothermal alteration, which was coeval within carbonate replacement sulfide ore at the Olympias deposit.

Sample PVD131 (290 m) was collected from a drill core intercept of a pervasively altered and mineralized segment of carbonaceous quartz-biotite gneiss immediately adjacent to semibrittle fault strands within the western segment of the Stratoni fault zone at the Piavitsa prospect (Fig. 11D). Muscovite occurs as euhedral to subhedral and mixed fine- to coarse-grained (greater than 500 μm) masses that are intergrown with bands of disseminated euhedral pyrite with lenticular quartz and dolomitic carbonate domains that define the shear fabric and alteration associated with sulfide ore (Fig. 13C). Step-heating analysis of an aliquot consisting of ~15 gr yielded a saddle-shaped $^{40}Ar/^{39}Ar$ age spectrum with a short, flat segment at its trough (steps 3–7) corresponding to an age of 24.0 ± 0.6 Ma, including ~62% of total ^{39}Ar released (MSWD = 5.20; Fig. 13D). Increasing ages from the higher-temperature steps may reflect inherited ^{40}Ar potentially derived from wall-rock micas. The plateau is interpreted as the minimum crystallization age of the mica and a minimum age of hydrothermal alteration associated with the replacement sulfide bodies in the Piavitsa area.

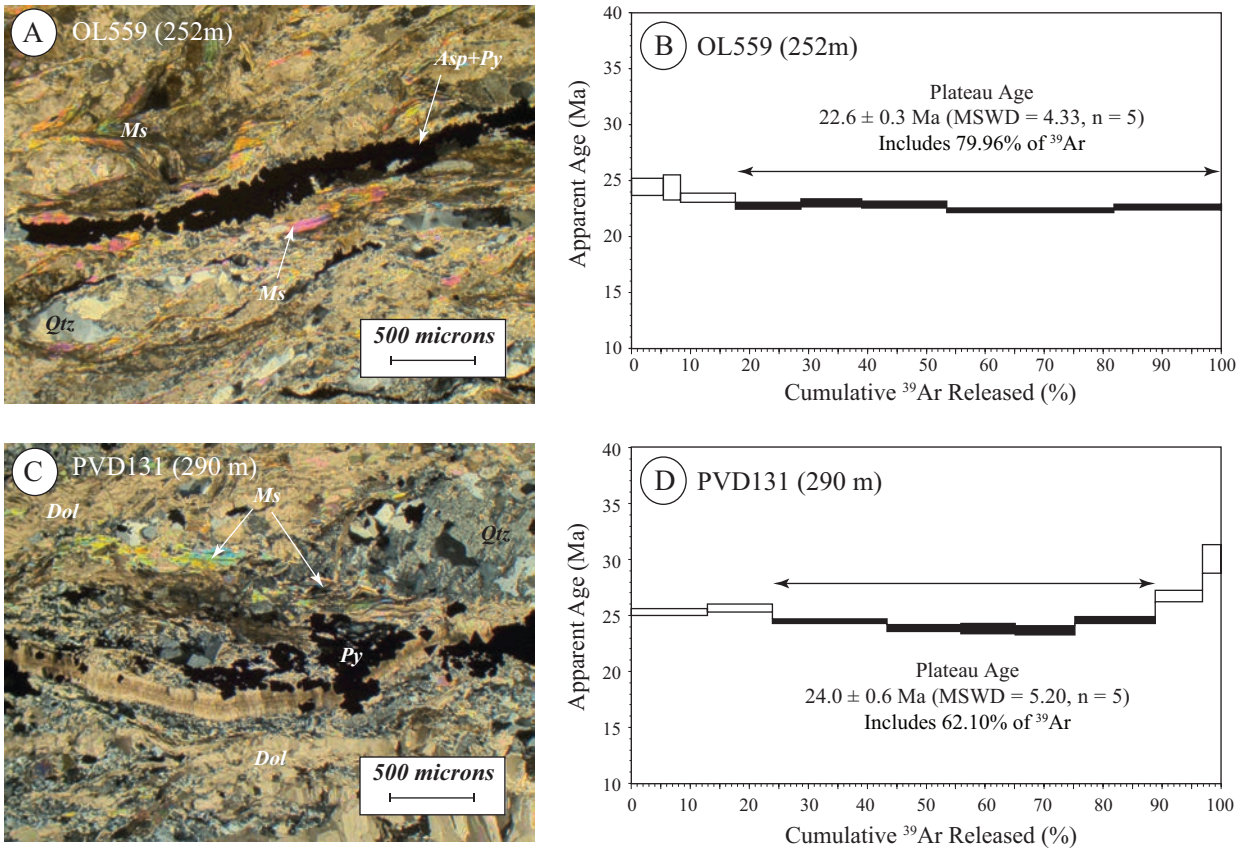

Fig. 13. Representative photomicrographs and step-heating Ar-release patterns for samples from the Olympias deposit and Piavitsa prospect. (A-B) Photomicrograph and Ar-release spectrum of sample OL559 (252 m) from a drill core intercept of the Kassandra fault at the Olympias deposit. An image of this sample is located in Figure 6E. (C-D) Photomicrograph and Ar-release spectrum of sample PVD131 (290 m) from a drill core intercept adjacent to a mineralized strand of the Stratoni fault at the Piavitsa prospect. An image of this sample is located in Figure 11D. Abbreviations: Asp = arsenopyrite, Dol = dolomite, Ms = muscovite, Py = pyrite, Qtz = quartz.

Structure of the Skouries Porphyry Au-Cu Deposit

The Skouries deposit lies 3.5 km north of the village of Megali Panagia and the Gomati fault zone (Fig. 14A). An early Miocene timing for porphyry emplacement and Au-Cu mineralization is constrained by a 20.6 ± 0.5 Ma zircon U-Pb crystallization age and 19.9 ± 0.9 Ma $^{40}Ar/^{39}Ar$ hydrothermal biotite age, respectively (Hahn et al., 2012; Hahn, 2014). These radiometric ages agree with the 19.0 ± 1.0 Ma zircon-uranothorite age of Frei (1992). Previous studies on the Skouries deposit have largely focused on the mineralogical and physiochemical conditions of ore deposition (Eliopoulos and Economou-Eliopoulos, 1991; Frei, 1995; McFall et al., 2016). Structural studies from the deposit area are limited to unpublished consulting reports. The following section presents a revised geologic map and cross section of the Skouries area that includes the Aspro Lakkos porphyry and is based on surface and drill core observation. Structural measurements of ductile metamorphic fabrics in the host gneiss and schist and vein orientations from the Skouries stock were collected from surface outcrops.

The Skouries deposit

The Skouries porphyry Au-Cu deposit is largely hosted by a composite high-K calc-alkaline to shoshonitic, megacrystic K-feldspar porphyry intrusion that was emplaced into quartz-rich micaceous gneiss and schist of the Vertiskos unit (Fig. 14A; Eliopoulos and Economou-Eliopoulos, 1991; Frei, 1992, 1995; Tobey et al., 1998; Kroll et al., 2002; Hahn et al., 2012; Hahn, 2014; Siron et al., 2016). The mineralized porphyry intrusion forms a narrow, less than 200-m-diameter, pencil-like stock that plunges steeply to the south-southwest and obliquely crosscuts the moderate to steeply NE dipping limb of a district-scale F_2 antiform (Fig. 14A, B). Surface exposures and drill data indicate that the porphyry stock has a subtle northeast elongate geometry. Four K-feldspar porphyritic intrusive phases of quartz monzonite composition comprise the Skouries stock and are described in Siron et al. (2016). The relative timing relationships among the porphyry phases are based on mineralogy, texture, and crosscutting relationships (Tobey et al., 1998; Kroll et al., 2002; Siron et al., 2016). Margins of the porphyry stock exhibit sharp and discordant intrusive contacts with respect to S_1 foliation and F_2 folds developed within the metamorphic host rocks.

Four principal vein stages and associated alteration are recognized at the Skouries deposit. The oldest vein set is a dense stockwork to sheeted array of quartz-only, quartz-magnetite, and magnetite-only stringer veins associated with pervasive disseminated magnetite and secondary K-feldspar

alteration (Fig. 15A-C). Introduction of Au-Cu was accompanied by quartz-magnetite-chalcopyrite veins associated with K-feldspar-biotite-magnetite alteration and by a later crosscutting set of sulfide-rich quartz-biotite-chalcopyrite-bornite ± magnetite veins (Kroll et al., 2002; Siron et al., 2016). Chalcopyrite-bearing magnetite veins and the later set of quartz-biotite-chalcopyrite-bornite ± magnetite veins mainly occur within the early and intramineral porphyry phases of the intrusive stock, while younger porphyry phases may host later sulfide-rich chalcopyrite-bornite veins (Siron et al., 2016), particularly deep in the deposit. Mineralized veins also occur within enclaves of schist between porphyry phases and immediately surrounding the composite porphyry stock. A younger assemblage of pyrite-carbonate (ferroan calcite-ankerite) ± base metal veins, similar to the "D" veins described by Gustafson and Hunt (1975), are accompanied by fine-grained white mica-carbonate alteration that envelops veins and minor fault breccias. These late-stage veins and associated alteration crosscut all porphyry phases within the stock and adjacent wall rock (Fig. 15D) but are volumetrically minor.

Widely spaced fractures and faults occur within the porphyry stock and the metamorphic wall rock, as observed in drill core and surface outcrops. Albeit minor, faults crosscut all porphyry phases, veins, and associated alteration. Faults in the Skouries area occupy steeply dipping, NW-striking planes that manifest as narrow, gouge-rich shear zones that are generally less than 0.5 m in width. Offset of compositional layers within the metamorphic sequence suggests that these faults accommodate only minor normal displacement.

Geometry of porphyry-related veins and dikes

Outcrops of the early quartz monzonite porphyry phase containing quartz-magnetite and chalcopyrite-bearing magnetite veins and associated pervasive K-feldspar-biotite-magnetite alteration form the surface expression of the Skouries deposit. These veins are steeply dipping and display a preferential north-northeast sheeted orientation (Fig. 15E). A volumetrically minor population of shallow-dipping quartz-only and quartz-magnetite veins associated with K-feldspar-magnetite envelopes (Fig. 15B) is also present in outcrop and at depth. These shallow-dipping veins are crosscut by younger, steeply dipping Cu-bearing quartz-magnetite veins (Fig. 15B, C). Pyrite-carbonate ± base metal veins that occur within a 1-km radius of the porphyry stock are interpreted to be the distal expression of the Skouries magmatic-hydrothermal system. These young and spatially distal veins strike to the northwest-southeast and north-south (Fig. 15F), oblique to the direction of S_1 foliation and subparallel to the fault-fracture network in the area.

Late-stage megacrystic K-feldspar porphyry dikes hosted by gneiss and schist occur within 0.5 km from the Skouries stock. Porphyry dikes display steeply dipping planar geometries with sharp and discordant contacts with respect to S_1 foliation. These dikes typically lack veins, locally exhibit a weak, albeit pervasive sericite-pyrite alteration, and crosscut amphibole-magnetite–altered schist adjacent to the porphyry stock. An anisotropic distribution of porphyry dike orientations is evident from outcrop with northeast-southwest strikes predominating and a subordinate set that strikes roughly in an east-west direction (Fig. 15G).

Discussion

Deformation history and kinematic evolution of extensional faulting in the Kassandra mining district

The metamorphic basement rocks belonging to the Permo-Carboniferous to Jurassic Kerdilion unit and the Ordovician-Silurian Vertiskos unit within the Kassandra mining district were affected by at least three synmetamorphic deformation episodes beginning with an early D_1 event that resulted in a penetrative S_1 foliation accompanied by amphibolite-facies metamorphism. The D_2 event reworked the earlier S_1 penetrative fabrics into tight to open F_2 folds with an associated axial planar S_2 cleavage and locally prominent L_2 intersection lineation. A younger and lower-strain D_3 event resulted in an S_3 cleavage, which overprinted all earlier ductile fabrics. D_1 and D_2 fabrics both imply top-to-the-northeast vergence possibly representing increments of progressive deformation associated with regional Eocene or older contraction. Contractional ductile deformation likely continued through the late Paleocene, as evidenced by intrusions that contain a penetrative S_1 foliation.

The Stratoni fault zone originated as a mylonitic normal fault that was active during regional SW-directed ductile extension, as demonstrated at the Madem Lakkos deposit by Haines (1998). Mylonitic shear zones nucleated within a lithologically complex section of the Kerdilion metamorphic sequence where the orientation of ductile structural fabrics were approximately perpendicular to the principal axis of extension. Extensional mylonites preferentially exploited the rheologically weak marble and graphitic metapelite unit bounded by massive amphibolite to the south with granite gneiss and quartzofeldspathic gneiss to the north. Mylonitic shear zones in the Olympias area, however, are less prominent than within the Stratoni fault zone and are largely restricted to a diffuse shear zone network between the Kassandra and East faults. Sharp rheological gradients between quartzofeldspathic biotite gneiss and conformably interlayered graphite-bearing marble units with granitic pegmatite sills established a stratigraphic control for localizing extensional strain. Based on textural and kinematic similarities, the mylonitic shear zones within the Olympias deposit were probably coeval with extensional mylonites in the Stratoni fault zone. Mylonitic deformation probably initiated at the onset of regional extension during the middle Eocene based on apatite and zircon fission track ages from the Kerdilion detachment fault located to the west of the Kassandra mining district (Fig. 2; Wüthrich, 2009; Kounov et al., 2015).

Semibrittle faults overprint earlier mylonitic shear zones in the Olympias area and within the Stratoni fault zone. Textures suggest that ductile-brittle fault fabrics formed by the mechanical reduction of grains through cataclastic flow (e.g., Sibson, 1977), whereas carbonaceous fault-slip surfaces and pressure solution (stylolitic) fabric development was facilitated by volume loss through dissolution mass transfer processes. Deformation at this time was likely accelerated locally by the introduction of hydrothermal fluids into the previously developed mylonitic shear zone (e.g., Cox et al., 2001), resulting in the formation of a shear-related foliation. Kinematic fault-strain features showing top-to-the-south normal displacement along semibrittle strands of the Stratoni fault were controlled

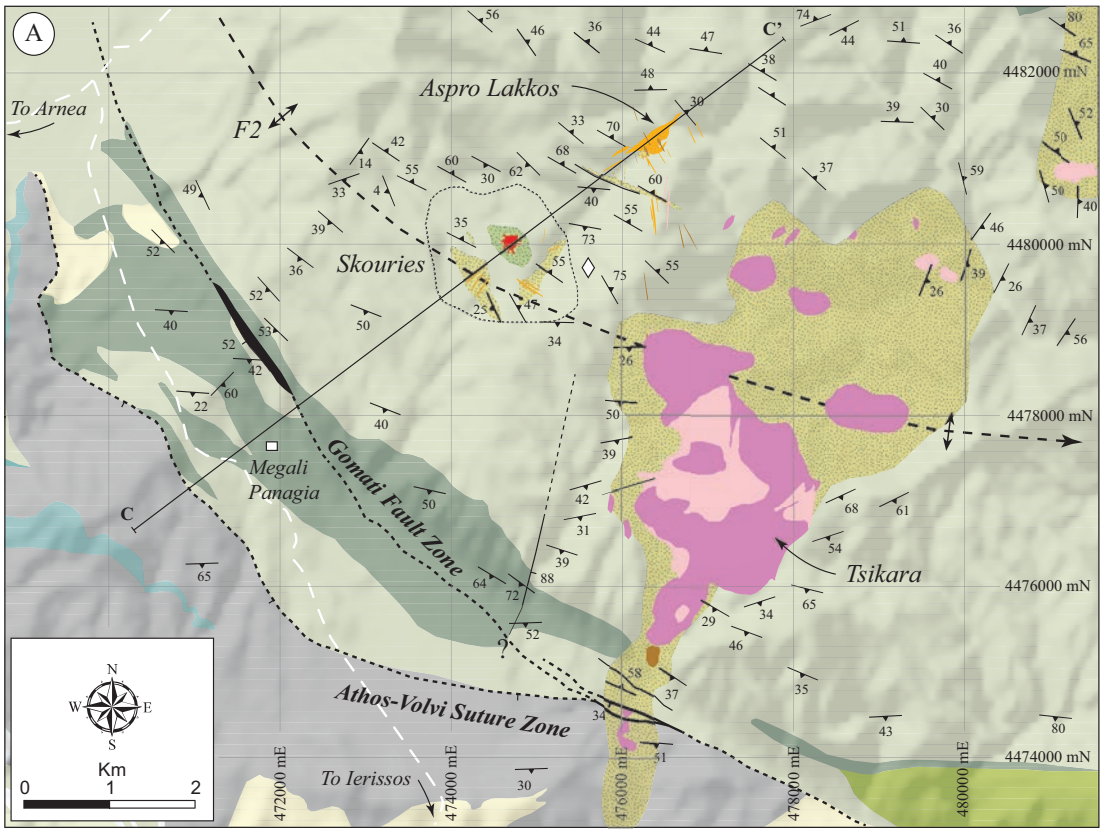

Igneous Rocks

- Trachyandesite porphyry dike (19.6 Ma; Siron et al., 2016)
- Aspro Lakkos quartz monzonite porphyry (19.7 Ma; Siron et al., 2016)
- Skouries quartz monzonite porphyry (20.6 Ma; Hahn et al., 2012)
- Tsikara granodiorite, variably porphyritic (27 Ma; Siron et al., 2016)
- Tsikara monzogabbro and monzodiorite (27 Ma; Siron et al., 2016)

Triassic-Jurassic Rift-related Rocks

- Quartz-sericite marble and calc-schist
- Graphitic phyllite and quartzite
- Amphibolite with interlayered gabbro and amphibole-bearing pyroxenite, massive and non-foliated
- Serpentinized peridotite and dunite

Ordovician-Silurian Vertiskos Unit

- Quartz-rich muscovite-biotite schist intercalated with leucocratic augen gneiss
- Pegmatitic granite gneiss (unknown affiliation)

Alteration and Mineralization

- Quartz-sericite-pyrite ± galena
- Amphibole-K-felspar-biotite-magnetite
- Demagnetization (pyrite) halo of the Skouries porphyry defined by unpub. aero-magnetic data

Map and Cross Section Symbols

- Fault damage zone, dashed where approx., marker indicating dip (40)
- Antiform axis indicating plunge direction
- Strike-dip of S1 foliation (plan view) (30)
- Strike-dip of S1 foliation (cross section) (30)
- SOP-137 Drill hole (cross section)
- Normal fault; reactivated thrust fault?
- Mélange (Athos-Volvi Suture Zone; Himmerkus et al., 2005)
- Zircon U-Pb (Hahn, 2014)
- Village

Fig. 14. (A) Detailed geologic map of the Skouries deposit and surrounding area modified after Kockel et al. (1975, 1977). Mapping was conducted at 1:5,000 scale and based largely on surface outcrops. (B) Cross section C-C' of the Skouries porphyry and the postmineral Aspro Lakkos porphyry is based on surface mapping and drill core. Trace of folded S_1 foliation is illustrated by the dotted line. Coordinates are displayed in the Greek Geodetic Coordinate System (GGRS 87 Greek Grid).

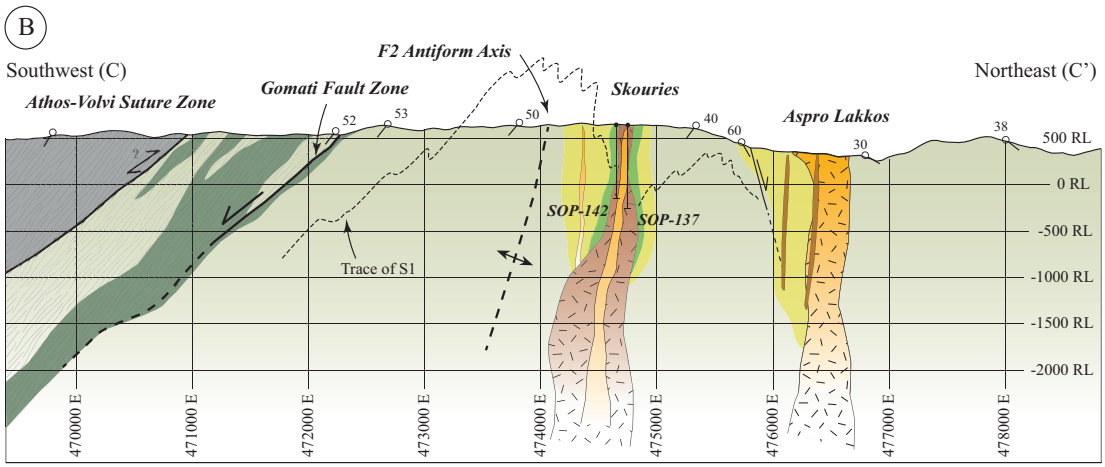

Fig. 14. *(Cont.)*

by north-south extension (Fig. 16, red circles). Due to limited exposure, however, kinematic control on the synmineral fault strands in the Olympias area is less well defined. Kinematic data from the striated, sulfide-bearing Kassandra fault surface exposed underground in the Olympias mine indicates control by a NE-directed extensional strain axis (Fig. 8A), which is consistent with postmineral deformation.

An east-west extensional event was recorded by a set of incipiently mineralized fault strands that crosscut massive sulfide within the Stratoni fault zone (Fig. 16, green squares). Kinematic fault-slip data from the Olympias area and the Gomati fault zone in the south (Fig. 2) also record this tectonic event. Faults demonstrating east-west extension within the district may correspond to a widespread east-northeast–west-southwest extensional episode documented by others workers within the region (e.g., Kilias et al., 1999). This period of extension may have been episodically prolonged through the late Oligocene and early Miocene, controlling the upper crustal emplacement of NNE-trending porphyry dikes, as well as the Au-bearing quartz-rhodochrosite veins localized along N- and NNE-trending faults.

Subsequent northeast-southwest extension within the district is recorded by brittle faults that crosscut the Mavres Petres and Madem Lakkos sulfide orebodies and therefore postdate the carbonate replacement event. Postmineral brittle faults, such as the corrugated fault scarp that crops out above the Madem Lakkos mine, are texturally and kinematically compatible with middle to late Miocene NE-SW–directed extension (Fig. 16, blue triangles) as documented from other fault zones in the north Aegean region (Dinter and Royden, 1993; Sokoutis et al., 1993; Dinter, 1998; Kilias et al., 1999). Fault-slip indicators recording northeast-southwest extension in the Olympias area are kinematically compatible with postmineral fault strands within the Stratoni fault zone and, by association, reflect middle to late Miocene extension.

Steeply dipping fault surfaces aligned subparallel to the Stratoni fault zone and displaying SSE-plunging slickenlines record a final stage of north-south extension (Fig. 16, gray diamonds). These faults are differentiated from late Oligocene semibrittle and mineralized fault strands within the Stratoni fault zone by their brittle textures, unconsolidated gouge fill, and overprinting relationship relative to all earlier fabrics and fault surfaces. Kinematic data that describes this fault set agrees with published results from neotectonic faults within the Stratoni fault zone (Pavlides and Tranos, 1991). Gouge-filled faults and brittle fracture zones that occur at the Olympias deposit are probably coeval with the most recent faults evident in the Stratoni fault zone. This youngest fault set is interpreted to have formed by the late Quaternary and may be related to active tectonism (Pavlides and Tranos, 1991; Koukouvelas and Aydin, 2002; Pavlides and Caputo, 2004; Michailidou et al., 2005; Pavlides et al., 2010).

Structural controls and timing of carbonate replacement and vein-style mineralization

The carbonate replacement sulfide deposits in the district exhibit morphologies that are influenced by a preexisting ductile structural architecture and the interaction of synmineral faults with marble host rocks. In the Olympias area, premineral, penetrative L_2 intersection lineations and F_2 folds that developed within the gneisses and marbles contribute to a structurally enhanced SE-plunging permeability network. Termination of the Kassandra fault at depth into an en echelon network of subsidiary shallow-dipping mylonitic to semibrittle fault strands likely resulted from the lateral transfer of strain controlled by the rheologically heterogeneous metamorphic sequence (Fig. 5B). Permeable pathways developed between the Kassandra and East faults, facilitated by the intersection of shallow-dipping mylonites with preexisting ductile fabrics, were exploited by hydrothermal fluids that reacted with marble to produce replacement sulfide orebodies (Fig. 17A).

Previous studies have concluded that the sulfide orebodies at the Olympias deposit resulted from magmatic fluids (Kalogeropoulos et al., 1989); however, no definitive source intrusion was identified. A published arsenopyrite Re-Os age of 26.1 ± 5.3 Ma (Hahn et al., 2012; Hahn, 2014) indicates an Oligo-Miocene age of sulfide deposition. An undeformed granitic dike located in the western portion of the Olympias deposit yielded zircon U-Pb ages between 29.2 ± 0.5 and 21.3 ± 0.3 Ma (Hahn, 2014), consistent with a local magmatic event coeval with ore formation. The mineralized magmatic-hydrothermal granite breccia body located in the footwall of

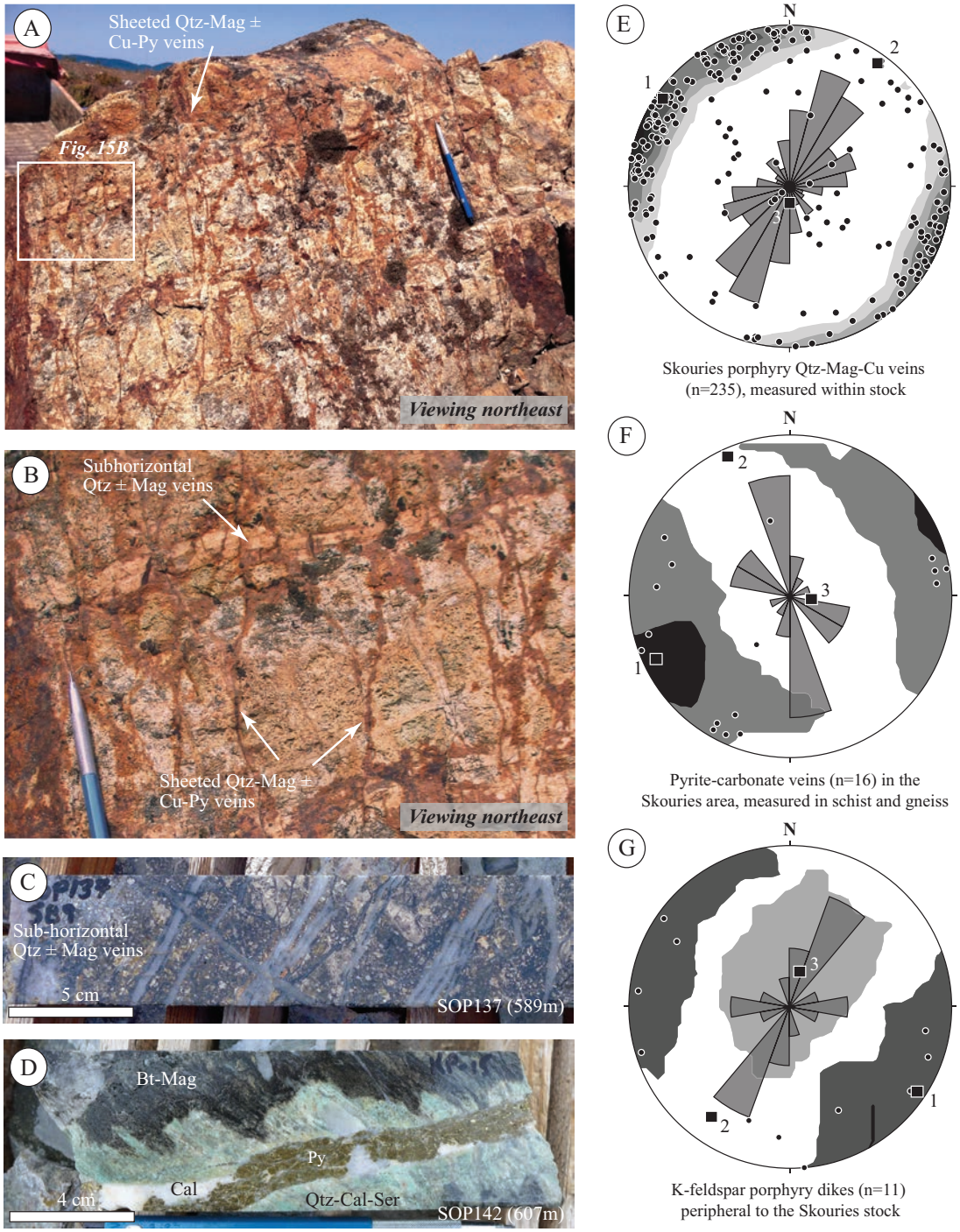

Fig. 15. Representative photos of porphyry-style veins and vein measurement data from the Skouries area. (A) Early quartz monzonite porphyry phase cropping out in the Skouries open-pit area hosting sheeted quartz-magnetite veins, which strike northeast. (B) Close-up view of box in (A) showing oxidized Cu-bearing quartz-magnetite veins that crosscut earlier subhorizontal quartz ± magnetite veins. (C) Drill core example of quartz-magnetite veins crosscutting the early quartz monzonite porphyry phase. These veins occur at a high angle to core axis (vertical hole) indicating that they belong to the subhorizontal set. Note the steeply dipping vein, which overprints the shallow-dipping set. (D) Late pyrite-ferroan calcite vein with a pale-green mica-quartz-carbonate envelope replacing biotite-magnetite–altered schist adjacent to the porphyry stock. (E) Stereonet of quartz-magnetite and Cu-bearing quartz-magnetite veins measured from the porphyry stock in outcrop. (F) Stereonet of pyrite-carbonate veins occurring within the Vertiskos unit in the Skouries area. (G) Late-stage K-feldspar porphyry dikes occurring peripheral to porphyry stock. Stereonets display planar data represented as poles in a lower-hemisphere, equal-area projection and contoured at 3σ significance level following the method of Kamb (1959). The rose diagram illustrates azimuth of veins and dikes with petals displayed as axes and scaled by length. Axial distributions are plotted as black squares with numbers corresponding to density concentrations ranging from greatest (1), intermediate (2), and least (3). Abbreviations: Bt = biotite, Cal = calcite, Mag = magnetite, Py = pyrite, Qtz = quartz, Ser = sericite.

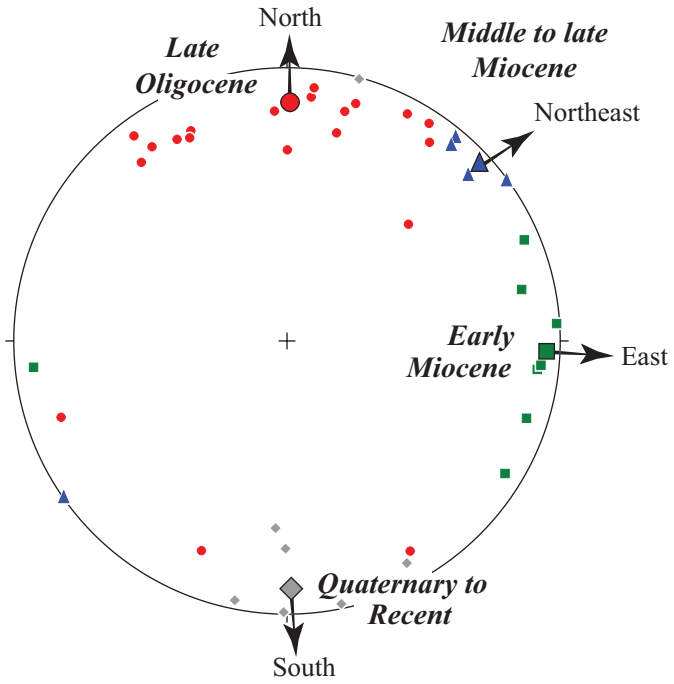

Fig. 16. Kinematic evolution model for the Stratoni fault zone presented as a distribution of the principal extensional strain axes from individual fault measurements plotted in a lower-hemisphere, equal-area stereographic projection. The principal extensional strain axes for each fault population are plotted as small symbols with the mean represented by large symbols with arrows indicating the extension direction.

the Kassandra fault is similar to the unstrained aplitic granite bodies that are spatially related to sulfide ore at the Madem Lakkos deposit (Gilg, 1993; Haines, 1998), further supporting a close Oligo-Miocene igneous association to ore. The post-mineral timing of glomerophyric porphyry dikes that crosscut Olympias ore and their geochemical correlation with the early Miocene porphyry suite (Siron et al., 2016) suggest a minimum age of sulfide deposition at ~20 Ma.

Ductile fabrics and folds are also important within the Stratoni fault zone and contributed to the localization of the sulfide ores. Quartzofeldspathic gneiss and marbles reworked by F_2 folds associated with the Madem Lakkos antiform (Fig. 10A) resulted in an ESE-plunging permeability network in the footwall of the Stratoni fault zone (Fig. 17B). On the S-dipping limb of the Madem Lakkos antiform, the rheological contrasts between quartzofeldspathic biotite gneiss and granite gneiss with marble and massive amphibolite likely localized strain and facilitated the propagation of the eastern segment of the Stratoni fault zone. Mineralized semibrittle faults displaying south-southwest and east-west fault-slip vectors reported in Haines (1998) from the Madem Lakkos mine are consistent with the kinematic data presented in this study and correspond to the syn- and late-mineral kinematic evolution of the Stratoni fault zone, respectively. Structural evidence combined with field relationships demonstrate that the Stratoni fault zone forms the principal permeability pathways that focused hydrothermal fluids.

In the Mavres Petres and Piavitsa areas, the Stratoni fault zone and contained marble lenses constitute the principal structural and lithologic controls for massive sulfide ore formation. Dismembered marble lenses enclosed by foliated carbonaceous phyllonite and entrained by segments of the Stratoni fault form the elongate downdip component of the replacement sulfide orebody (Fig. 17B). The Mavres Petres deposit is broadly coincident with a change in strike orientation of the Stratoni fault zone, which is interpreted to represent the linkage between two overlapping fault segments. The graphitic metapelitic unit, evident along the western segment of the Stratoni fault zone, may have provided a structurally weak layer that concentrated deformation potentially aided by fluid-enhanced pressure solution mass transport mechanisms. Localization of strain is interpreted to have been largely controlled by the lithologic anisotropy imposed by the carbonaceous metapelite layer juxtaposed to massive amphibolite and facilitated by the preferred orientation of the Stratoni fault zone with respect to the principal stress field at the time of deformation. Internal fault bifurcations, fault intersections, and incompatible strain behavior between coeval fault strands and the high surface area of locally imbricated marble lenses within the Stratoni fault zone contributed to a mechanically enhanced permeability network, which was exploited by migrating hydrothermal fluids.

The late Oligocene Stratoni and Fisoka granodiorite stocks (Fig. 9) or possibly a concealed intrusion in the area may have been the potential igneous source of mineralizing fluids that resulted in the carbonate replacement sulfide orebodies in the Stratoni fault zone (Gilg and Frei, 1994; Haines, 1998; Hahn, 2014; Siron et al., 2016). The mylonitic and unstrained aplitic granite dikes that are spatially associated with ore at the Madem Lakkos deposit are potentially comagmatic with the Stratoni and Fisoka granodiorite stocks (Gilg and Frei, 1994). A shift in the direction of extension from north-south to east-west occurred after sulfide deposition and late Oligocene magmatism. The NNE- to NE-striking glomerophyric and black-matrix porphyry dikes within the Stratoni fault zone (Fig. 10A) support fault kinematic data in suggesting that E-W–directed extension was active through the early Miocene. The Au-bearing quartz-rhodochrosite ± rhodonite vein breccias crosscut sulfide ore and semibrittle shear zones in the Mavres Petres and Piavitsa areas, indicating a later timing relative to carbonate replacement mineralization (Fig. 18). Quartz-rhodochrosite ± rhodonite veins fill N- to NNE-striking faults, which principally show normal displacement, implying that east-west extension also controlled their emplacement.

The $^{40}Ar/^{39}Ar$ ages determined from hydrothermal muscovite spatially and probably genetically associated with sulfide ore suggest a minimum alteration and mineralization age between 25 and 22 Ma (Fig. 18). Green mica, intergrown with

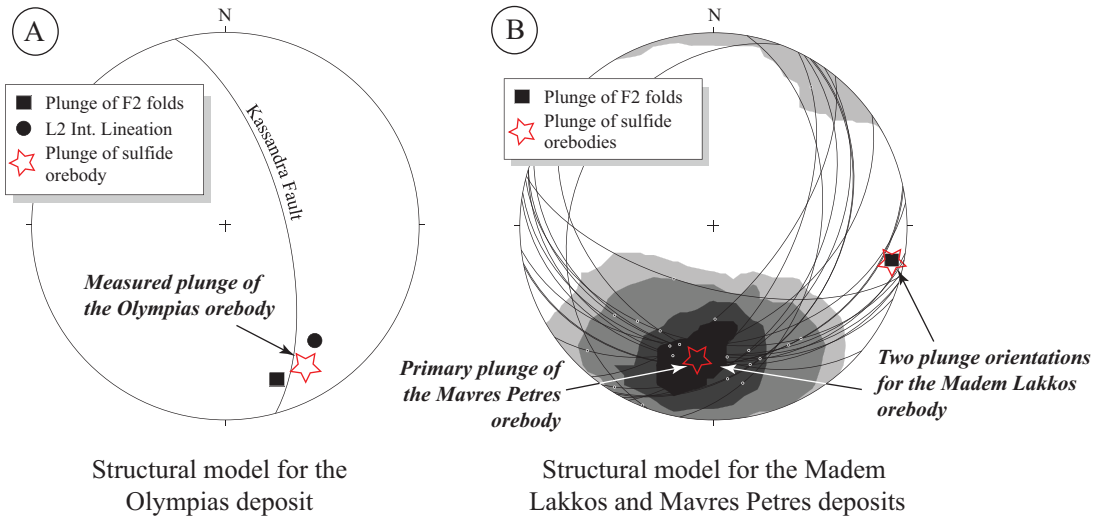

Fig. 17. Schematic summary diagram displaying structural data and plunge orientation of carbonate replacement orebodies plotted in a lower-hemisphere, equal-area stereographic projection. (A) Measured plunge of the Olympias orebody with the Kassandra fault plotted as a great circle and the mean plunge of F_2 fold hinges and (S_1, S_2) L_2 intersection lineations plotted as square and circle, respectively. (B) Plunge of the Madem Lakkos and Mavres Petres orebodies plotted with fault surfaces defining the Stratoni fault zone indicated by great circles. Fault-slip vectors are indicated by small circles and contoured using the method of Kamb (1959). The mean plunge of F_2 fold hinges from the footwall of the Stratoni fault zone is plotted as a square.

sulfide ore and in part defining the tectonic fabric within semibrittle strands of the Stratoni fault, suggests that deformation, alteration, and mineralization were synchronous. The 24.0 ± 0.6 Ma $^{40}Ar/^{39}Ar$ age for muscovite at the Piavitsa prospect is interpreted as the timing of the carbonate replacement sulfide event, coeval with semibrittle extensional faulting and late Oligocene magmatism within the Stratoni fault zone. This timing is supported by field relationships and overlaps within analytical error the zircon U-Pb crystallization age of the Fisoka granodiorite stock (24.5 ± 0.1 Ma; Siron et al., 2016). Synkinematic intergrowths of hydrothermal muscovite-dolomite with sulfide similarly define the tectonic fabric of semibrittle shear bands within the Kassandra fault at the Olympias deposit. The 22.6 ± 0.3 Ma $^{40}Ar/^{39}Ar$ age is interpreted to reflect the timing of carbonate replacement sulfide and semibrittle extensional faulting in the Olympias area. This minimum $^{40}Ar/^{39}Ar$ age, while younger than the Piavitsa prospect, is still supportive of a late Oligocene mineralizing event possibly driven by the granite that resulted in the igneous breccia or a parent intrusion at depth in the Olympias area.

Structural controls on the emplacement of the Skouries porphyry

The crosscutting relationships observed between intrusive phases with Au-Cu–mineralized veins and associated alteration, supported by published geochronological data, demonstrate that the Skouries deposit was part of an early Miocene magmatic-hydrothermal event (Frei, 1995; Kroll et al., 2002; Hahn et al., 2012; McFall et al., 2016; Siron et al., 2016). Structural data and outcrop patterns indicate that the Skouries stock occupies the steep NE-dipping limb of a major NW-trending district-scale F_2 antiform (Fig. 14A, B) and is interpreted to be the principal structure that controlled upper crustal emplacement.

The subtle NE-elongate geometry of the Skouries stock is broadly mimicked by the preferred northeast orientation of related porphyry dikes and Au-Cu mineralized veins contained within the stock. The shallow-dipping to flat-lying veins within the porphyry stock imply transient fluid overpressure conditions and hydraulic fracturing of a crystallizing hydrous magma within a fluid-saturated magmatic-hydrothermal environment (e.g., Gruen et al., 2010). The lack of sulfide and the early paragenesis of these veins indicate that the subhorizontal hydraulic fracturing processes occurred relatively early and possibly at higher temperature than the main mineralizing vein events. The younger, steeply dipping and sheeted veins within the porphyry stock dilated in response to northwest-southeast and west-northwest–east-southeast extension (Fig. 15E). Variations in the orientation of steeply dipping veins, however, indicate that dilation of subvertical fractures varied spatially within the porphyry stock and may reflect localized, episodic fluctuations in the orientation of the horizontal differential stress axes during Au-Cu mineralization (e.g., Tosdal and Richards, 2001). Pyrite-carbonate ± base metal veins overprint all earlier vein phases and associated K-feldspar and biotite-magnetite alteration, suggesting that they developed late with respect to the Skouries magmatic-hydrothermal system.

The preferred northeast orientation of porphyry dikes surrounding the Skouries stock is consistent with the pattern developed by the Au-Cu mineralized veins, as well as the subdued elongation direction of the porphyry stock. The differential horizontal stresses developed within an anisotropic regional stress field likely influenced the northeast orientation of structural elements related to the Skouries porphyry system (e.g., Tosdal and Richards, 2001). The early Miocene and barren Aspro Lakkos porphyry stock located 2 km to the northeast of the Skouries deposit also displays a northeast-southwest

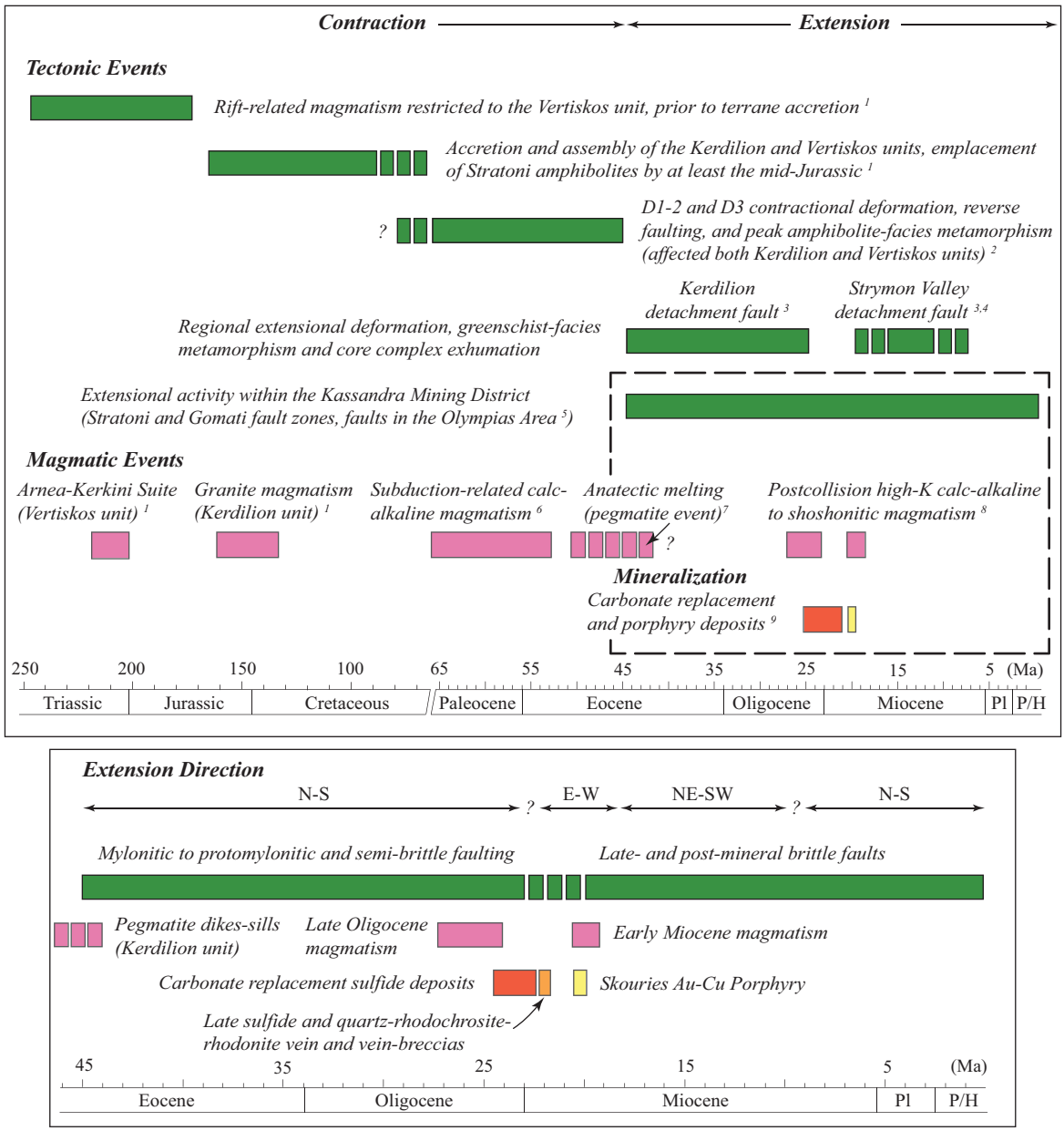

Fig. 18. Summary diagram illustrating the timing of structural, magmatic, and mineralization events in the Kassandra mining district. Timing constraints are supported by the following references.
[1] Zircon U-Pb and Pb-Pb ages (Himmerkus et al., 2006, 2009b, 2011; Hahn, 2014);
[2] Field relationships (this study);
[3] Apatite and zircon fission track ages (Brun and Sokoutis, 2007; Wüthrich, 2009; Kounov et al., 2015);
[4] $^{40}Ar/^{39}Ar$ ages of biotite and K-feldspar (Dinter and Royden, 1993, and references therein; Dinter et al., 1995);
[5] Field relationships (Pavlides and Tranos, 1991; Haines, 1998; this study);
[6] Zircon U-Pb and Pb-Pb ages (Frei, 1992, 1996; Himmerkus el al., 2011; this study);
[7] White mica Rb-Sr ages and field relationships (Kalogeropoulos et al., 1989; Wawrzenitz and Krohe, 1998; this study);
[8] Zircon U-Pb ages (Siron et al., 2016);
[9] K-Ar age of hydrothermal illite (Madem Lakkos: Gilg and Frei, 1994), Re-Os arsenopyrite age (Olympias: Hahn et al., 2012; Hahn, 2014), $^{40}Ar/^{39}Ar$ age of hydrothermal biotite (Skouries: Hahn et al., 2012; Hahn, 2014), and $^{40}Ar/^{39}Ar$ ages of hydrothermal muscovite (Olympias and Piavitsa: this study).

elongation (Fig. 14A). This northeast orientation is similarly shared by the chain of late Oligocene igneous stocks and dikes (Fig. 2), which likely reflects a crustal-scale structure that acted as a conduit for the shallow emplacement of rising magmas. During the early Miocene, a shift from NS- to EW-directed extension, as evidenced by fault kinematic data and crosscutting structural relationships, may have triggered ascent of fertile magmas through the upper crust, localizing the Skouries porphyry stock within the steeply dipping limb of a major district-scale antiform.

Summary and Conclusions

The Kassandra mining district belongs to the Serbo-Macedonian metallogenic province, an Oligo-Miocene magmatic belt developed in a postcollisional and extensional back arc environment that hosts porphyry Au-Cu and polymetallic carbonate replacement deposits, including vein and skarn systems (Janković, 1997; Serafimovski, 2000; Heinrich and Neubauer, 2002). Ores hosted by marble along with elevated Au contents distinguish the Madem Lakkos, Mavres Petres, and Olympias deposits from other carbonate-hosted systems within the belt (e.g., Trepča mining district of eastern Kosovo; Strmić-Palinkaš et al., 2013). While similarly hosted by marble of Rhodope origins and strongly controlled by extensional faults, the carbonate replacement deposits in the Madan-Thermes district of southern Bulgaria and northeastern Greece are older, closely associated with late Eocene to early Oligocene magmatism, and notably deficient in gold (Marchev et al., 2005; Kaiser Rohrmeier et al., 2013). The early Miocene Skouries porphyry Au-Cu deposit broadly resembles, in terms of chemistry and structural setting, other mineralized porphyry deposits in the Serbo-Macedonian metallogenic province, such as the early to late Oligocene Kiseljak and Buchim deposits of southern Serbia and the Republic of Macedonia, respectively (Serafimovski et al., 2010; Márton et al., 2013). These porphyry systems, including Skouries, are analogous to economic porphyry deposits developed in postcollisional back arc settings described elsewhere (e.g., Ridgeway-Cadia and North Parkes districts of New South Wales, Australia; Wilson, 2003).

The Stratoni fault zone has been historically viewed as the tectonic boundary separating the Kerdilion unit from the Vertiskos unit (Kockel et al., 1977). The Kerdilion unit is compositionally gradational with no observable change in metamorphic grade across the Stratoni fault zone. Amphibolites occurring in footwall and hanging-wall domains are conformably interlayered in the Kerdilion unit and are geochemically indistinguishable. Ductile structural elements spanning the Stratoni fault zone also display consistent deformation patterns, suggesting that footwall and hanging-wall rock types were affected by the same phases of deformation, for which synmetamorphic fabrics are largely contractional (Fig. 18). These data suggest that the tectonic boundary between the Kerdilion and Vertiskos units is probably an older structure and not a detachment as previously thought (Haines, 1998; Kounov et al., 2015).

The location and morphology of carbonate replacement sulfide deposits within the Kassandra mining district is influenced by a preexisting ductile structural architecture and the interaction of synmineral faults with available marble host rocks. The Olympias orebody is controlled by a SE-plunging L_2 intersection lineation and F_2 folds interacting with extensional mylonites and semibrittle shear zones that link the Kassandra and East faults within a hosting marble unit. Timing of mineralization may have overlapped with igneous activity, which locally formed a granite-matrix breccia and mylonite-associated granitic dikes and sills along ore-controlling faults. To the south, the Madem Lakkos orebody is controlled by marbles localized within the hinge of a footwall antiform and synmineral strands of the Stratoni fault zone (Gilg, 1993; Gilg and Frei, 1994; Haines, 1998) in association with granite dikes that may form part of the late Oligocene intrusive suite. The Mavres Petres orebody, however, is hosted by fault-bounded marble lenses entrained within a strongly carbonaceous segment of the Stratoni fault zone.

Carbonate replacement sulfide ore and synmineral faults within the district were active from 24.0 ± 0.6 to 22.6 ± 0.3 Ma based on $^{40}Ar/^{39}Ar$ geochronology of hydrothermal muscovite. The $^{40}Ar/^{39}Ar$ data suggest a late Oligocene timing for sulfide deposition within the district, consistent with the zircon U-Pb crystallization ages from the Fisoka and Stratoni granodiorite stocks (Siron et al., 2016). Further work, however, is needed to assess the relationship of the granitic intrusions that are associated with mineralization in the Olympias and Madem Lakkos deposits to other Oligocene intrusions in the district.

Kinematic fault-slip data indicates that carbonate replacement mineralization was coeval with north-south extension during the late Oligocene (Fig. 18) with a later phase of east-west extension as evidenced by the kinematic data and implied by dikes and mineralized veins that occur within N- to NE-trending faults. Younger Au-bearing quartz-rhodochrosite vein and vein breccias that developed along these structures overprint semibrittle faults and sulfide within the Stratoni fault zone, suggesting that east-west extension was coeval with the latest phase of hydrothermal activity at the Mavres Petres deposit and the Piavitsa prospect (Fig. 18). Postmineral faults produced by northeast-southwest extension crosscut the sulfide orebodies within the Stratoni fault zone and are kinematically compatible with middle to late Miocene regional extension (Dinter, 1998). A final stage of brittle faulting overprints all earlier deformation events and is characterized by north-south extension typical of the modern tectonic environment (Pavlides and Tranos, 1991).

The early Miocene Skouries porphyry stock is hosted by folded gneiss and schist of the Vertiskos unit and crosscuts the moderate to steeply dipping limb of a major F_2 antiform. Quartz-magnetite and Au-Cu–mineralized quartz-biotite-chalcopyrite-bornite ± magnetite veins contained within the porphyry stock predominately strike to the northeast, consistent with the preferred orientation of related porphyry dikes. Ascent of fertile magmas into the upper crust may have been triggered by a change in the regional extensional stress field, as evidenced by fault kinematic data. Polymetallic carbonate-hosted replacement and porphyry Au-Cu ore formation manifested where a preexisting structural architecture juxtaposed reactive host rocks and localized magmatism within an evolving postcollisional, extensional back arc environment.

Acknowledgments

The first author would like to acknowledge Eldorado Gold Corporation for providing logistical and financial support for this study. We are grateful for the thoughtful discussions with Peter Lewis and Hellas Gold geologists Panagiotis Daoultzis, Antonis Garezos, Nikos Nestorov, George Perantonis, Scott Randall, Sally Russell, Grigorios Thermos, Pavlos Tsitsanis, and Timoleon Xonikis (Madem Lakkos), Ria Vagkli (Skouries), and Konstantinos Kydonakis and Panagiotis Zachariadis (Olympias). Samuel Haines is thanked for providing his thoughts on the structural evolution of the Stratoni fault zone from the now-closed Madem Lakkos mine. Richard Allmendinger (Cornell

University) is acknowledged for providing assistance in the interpretation and presentation of structural data, and Amy Willis (Cornell University) is graciously thanked for assisting with the interpretation of principal component data. A travel grant was awarded to the first author by the Mario Einaudi Center for International Studies at Cornell University. Richard Friedman (University of British Columbia) kindly provided comments on an earlier draft, and a critical review by Richard Tosdal significantly improved the quality of this manuscript. Shaun Barker is also acknowledged for providing a careful editorial review of the final version of this manuscript.

REFERENCES

Allmendinger, R.W., Cardozo, N., and Fisher, D., 2012, Structural geology algorithms: Vectors and tensors in structural geology: Cambridge, Cambridge University Press, 302 p.

Armijo, R., Meyer, B., Hubert, A., Barka, A., 1998, Westward propagation of the North Anatolian fault into the northern Aegean: Timing and kinematics: Geology, v. 27, p. 267–270.

Bébien, J., Michard, A., Montigny, R., Feinberg, H., and Voidomatis, P., 2001, The Grigoriou plutonic complex (Mt. Athos, Greece): A component of the north Aegean Eocene-Oligocene calc-alkaline magmatism: European Union of Geosciences Symposium, 11th, Strasbourg, France, 2001, LS03:314.

Best, M.G., Christiansen, E.H., Deino, A.L., Grommé, C.S., and Tingey, D.G., 1995, Correlation and emplacement of a large, zoned, discontinuously exposed ash flow sheet; the $^{40}Ar/^{39}Ar$ chronology, paleomagnetism, and petrology of the Pahranagat Formation, Nevada: Journal of Geophysical Research, v. 100, p. 24,593–24,609.

Bonev, N., and Dilek, Y., 2010, Geochemistry and tectonic significance of protoophiolitic metamafic units from the Serbo-Macedonian and western Rhodope massifs (Bulgaria-Greece): International Geology Review, v. 52, p. 298–335.

Bonev, N., Burg, J.-P., and Ivanov, Z., 2006, Mesozoic-Tertiary structural evolution of an extensional gneiss dome—the Kesebir-kardamos dome, eastern Rhodope (Bulgaria-Greece): International Journal of Earth Science, v. 95, p. 318–340.

Bonev, N., Dilek, Y., Hanchar, J.M., Bogdanov, K., and Klain, L., 2012, Nd-Sr-Pb isotopic composition and mantle sources of Triassic rift units in the Serbo-Macedonian and western Rhodope massifs (Bulgaria-Greece): Geological Magazine, v. 149, p. 146–152.

Brun, J.P., and Faccenna, C., 2008, Exhumation of high-pressure rocks driven by slab rollback: Earth and Planetary Science Letters, v. 272, p. 1–7.

Brun, J.P., and Sokoutis, D., 2007, Kinematics of the southern Rhodope core complex (North Greece): International Journal of Earth Science., v. 96, p. 1079–1099.

——2010, 45 m.y. of Aegean crust and mantle flow driven by trench retreat: Geology, v. 38, p. 815–818.

Burg, J.-P., 2012, Rhodope: From Mesozoic convergence to Cenozoic extension. Review of petrostructural data in the geochronological frame: Journal of the Virtual Explorer, v. 42, doi: 10.3809/jvirtex.2011.00270.

Burg, J.-P., Ivanov, Z., Ricou, L.-E., Dimor, D., and Klain, L., 1990, Implications of shear-sense criteria for the tectonic evolution of the central Rhodope massif, southern Bulgaria: Geology, v. 18, p. 451–454.

Burg, J.-P., Godfriaux, I., and Ricou, L.-E., 1995, Extension of the Mesozoic Rhodope thrust units in the Vertiskos-Kerdilion massifs (northern Greece): Comptes Rendus de l'Académie des Sciences, v. 320, p. 889–896.

Burg, J.-P., Ricou, L.-E., Ivanov, Z., Godfriaux, I., Dimor, D., and Klain, L., 1996, Synmetamorphic nappe complex in the Rhodope massif. Structure and kinematics: Terra Nova, v. 8, p. 6–15.

Cardozo, N., and Allmendinger, R.W., 2013, Spherical projections with OSX-Stereonet: Computers and Geosciences, v. 51, p. 193–205.

Christofides, G., D'Amico, C., Del Moro, A., Eleftheriadis, G., and Kyriakopoulos, C., 1990, Rb-Sr geochronology and geochemical characters of the Sithonia plutonic complex (Greece): European Journal of Mineralogy, v. 2, p. 79–87.

Christofides, G., Koroneos, A., Liati, A., and Kral, J., 2007, The A-type Kerkini granitic complex in north Greece: Geochronology and geodynamic implications: Bulletin of the Geological Society of Greece, vol. 40, p. 700–711.

Cox, S.F., Knackstedt, M.A., and Braun, J., 2001, Principals of structural control on permeability and fluid flow in hydrothermal systems: Reviews in Economic Geology, v. 14, p. 1–24.

Dazé, A., Lee, J.K.W., and Villeneuve, M., 2003, An intercalibration study of the Fish Canyon sanidine and biotite $^{40}Ar/^{39}Ar$ standards and some comments on the age of the Fish Canyon tuff: Chemical Geology, v. 199, p. 111–127.

de Boorder, H., Spakman, W., White, S.H., and Wortel, M.J.R., 1998, Late Cenozoic mineralization, orogenic collapse, and slab detachment in the European Alpine belt: Earth and Planetary Letters, v. 164, p. 569–575.

De Wet, A.P., Miller, J.A., Bickle, M.J., and Chapman, H.J., 1989, Geology and geochronology of the Arnea, Sithonia, and Ouranoupolis intrusions, Chalkidiki Peninsula, northern Greece: Tectonophysics, v. 161, p. 65–79.

Dimitriadis, S., Kondopoulou, D., and Atzemoglou, A., 1998, Dextral rotations and tectonomagmatic evolution of the southern Rhodope and adjacent regions (Greece): Tectonophysics, v. 299, p. 159–173.

Dinter, D.A., 1998, Late Cenozoic extension of the Alpine collisional orogen, northeastern Greece: Origin of the north Aegean basin: Geological Society of America Bulletin, v. 110, p. 1208–1230.

Dinter, D.A., and Royden, L., 1993, Late Cenozoic extension in northeastern Greece: Strymon Valley detachment system and Rhodope metamorphic core complex: Geology, v. 21, p. 45–48.

Dinter, D.A., Macfarlane, A., Hames, W., Isachsen, C., Bowring, S., and Royden, L., 1995, U-Pb and $^{40}Ar/^{39}Ar$ geochronology of the Symvolon granodiorite: Implications for the thermal and structural evolution of the Rhodope metamorphic core complex, northeastern Greece: Tectonics, v. 14, p. 886–908.

Dixon, J.E., and Dimitriadis, S., 1984, Metamorphosed ophiolitic rocks from the Serbo-Macedonian massif near lake Volvi, northeast Greece: Geological Society of London Special Publication, v. 17, p. 603–618.

Eldorado Gold Corporation, 2017, Resources and reserves: www.eldoradogold.com/assets/resources-and-reserves/, accessed October 29, 2017.

Eliopoulos, D.G., and Economou-Eliopoulos, M., 1991, Platinum-group elements and gold contents in the Skouries porphyry copper deposit, Chalkidiki Peninsula, northern Greece: Economic Geology, v. 86, p. 740–749.

Forward, P., Francis, A., and Liddell, N., 2010, Technical report on the Stratoni project Pb-Zn-Ag deposit, northern Greece: European Goldfields Limited, Technical Report NI 43-101, 54 p.

Frei, R., 1992, Isotope (Pb-Rb-Sr-S-O-C-U-Pb) geochemical investigations of Tertiary intrusions and related mineralizations in the Serbo-Macedonian (Pb-Zn, Sb + Cu-Mo metallogenetic) province in northern Greece: Unpublished Ph.D. thesis, Zürich, Switzerland, ETH Zürich, 231 p.

——1995, Evolution of mineralizing fluid in the porphyry copper system of the Skouries deposit, northeast Chalkidiki (Greece): Evidence from combined Pb-Sr and stable isotope data: Economic Geology, v. 90, p. 746–762.

——1996, The extent of inner mineral isotope equilibrium: A systematic bulk U-Pb and Pb step leaching (PbSL) isotope study of individual minerals from the Tertiary granite of Jerissos (northern Greece): European Journal of Mineralogy, v. 8, p. 1175–1189.

Fytikas, M., Innocenti, F., Manetti, P., Mazzuoli, R., Peccerillo, A., and Villari, L., 1984, Tertiary to Quaternary evolution of volcanism in the Aegean region: Geological Society of London Special Publication, v. 17, p. 687–699.

Gautier, P., Brun, J.-P., Moriceau, R., Sokoutis, D., Martinod, J., and Jolivet, L., 1999, Timing, kinematic and cause of Aegean extension: A scenario based on a comparison with simple analogue experiments: Tectonophysics, v. 315, p. 31–72.

Gilg, H.A., 1993, Geochronology (K-Ar), fluid inclusion, and stable isotope (C, H, O) studies of skarn, porphyry copper, and carbonate-hosted Pb-Zn (Ag, Au) replacement deposits in the Kassandra mining district (eastern Chalkidiki, Greece): Unpublished Ph.D. thesis, Zürich, Switzerland, ETH Zürich, 153 p.

Gilg, H.A., and Frei, R., 1994, Chronology of magmatism and mineralization in the Kassandra mining area, Greece: The potentials and limitations of dating hydrothermal illites: Geochimica et Cosmochimica Acta, v. 58, p. 2107–2122.

Gruen, G., Heinrich, C.A., and Schroeder, K., 2010, The Bingham Canyon porphyry Cu-Mo-Au deposit. II. Vein geometry and ore shell formation by pressure-driven rock extension: Economic Geology, v. 105, p. 69–90.

Gustafson, L.B., and Hunt, J.F., 1975, The porphyry copper deposit at El Salvador, Chile: Economic Geology: v. 70, p. 857–912.

Haines, H.S., 1998, A structural synthesis for sector Vb of the Madem Lakkos polymetallic sulfide deposit—northeast Greece: Unpublished M.Sc. thesis, London, University of London, 81 p.

Hahn, A., 2014, Nature, timing and geodynamic context of polymetallic mineralisation in the Kassandra mining district, North Greece: Unpublished Ph.D. thesis, London, Kingston University, 351 p.

Hahn, A., Naden, J., Treloar, P.J., Kilias, S.P., Rankin, A.H., and Forward, P., 2012, A new timeframe for the mineralization in the Kassandra mine district, N. Greece: Deposit formation during metamorphic core complex exhumation: European Mineralogical Conference, v. 1, 1EMC2012-742.

Heinrich, C.A., and Neubauer, F., 2002, Cu-Au-Pb-Zn-Ag metallogeny of the Alpine-Balkan-Carpathian-Dinaride geodynamic province: Mineralium Deposita, v. 37, p. 533–540.

Himmerkus, F., Zachariadis, P., Reischmann, T., and Kostopoulos, D.K., 2005, The mafic complexes of the Athos-Volvi-Zone—a suture zone between the Serbo-Macedonian massif and the Rhodope massif?: Geophysical Research Abstracts, v. 7, p. 10, 240.

Himmerkus, F., Reischmann, T., and Kostopoulos, D.K., 2006, Late Proterozoic and Silurian basement units within the Serbo-Macedonian massif, northern Greece: The significance of terrane accretion in the Hellenides: Geological Society of London Special Publication, v. 260, p. 35–50.

Himmerkus, F., Anders, B., Reischmann, T., and Kostopoulos, D., 2007, Gondwana-derived terranes in the northern Hellenides: Geological Society of America Memoir, v. 200, p. 379–390.

Himmerkus, F., Reischmann, T., and Kostopoulos, D.K., 2009a, Serbo-Macedonian revisited: A Silurian basement terrane from northern Gondwana in the internal Hellenides, Greece: Tectonophysics v. 473, p. 20–35.

——2009b, Triassic rift-related metagranites in the internal Hellenides, Greece: Geological Magazine, v. 146, p. 252–265.

Himmerkus, F., Zachariadis, P., Reischmann, T., and Kostopoulos, D., 2011, The basement of the Mount Athos Peninsula, northern Greece: Insights from geochemistry and zircon ages: International Journal of Earth Sciences., v. 101, p. 1467–1485.

Jahn-Awe, S., Froitzheim, N., Nagel, T.J., Frei, D., Georgiev, N., and Pleuger, J., 2010, Structural and geochronological evidence for Paleogene thrusting in the western Rhodopes, SW Bulgaria: Elements for a new tectonic model of the Rhodope Metamorphic Province: Tectonics, v. 29, TC3008, doi: 10.1029/2009TC002558.

Janković, S., 1997, The Carpatho-Balkanides and adjacent area: A sector of the Tethyan Eurasian metallogenic belt: Mineralium Deposita, v. 32, p. 426–433.

Jolivet, L., and Brun, J.P., 2010, Cenozoic geodynamic evolution of the Aegean region: International Journal of Earth Sciences, v. 99, p. 109–138.

Jolivet, L., Faccenna, C., Huet, B. , Labrousse, L., Le Pourhiet, L., Lacombe, O., Lecomte, E., Burov, E., Denele, Y., Brun, J.P., Philippon, M., Paul, A., Salaun, G., Karabulut, H., Piromallo, C., Monie, P., Gueydan, F., Okay, A.I., Oberhansli, R., Pourteau, A., Augier, R., Gadenne, L., and Driussi, O., 2013, Aegean tectonics: Strain localization, slab tearing, and trench retreat: Tectonophysics, v. 597–598, p. 1–33.

Jolliffe, I.T., 2002, Principal component analysis, 2nd ed.: New York, Springer, 487 p.

Jones, C.E., Tarney, J., Baker, J.H., and Gerouki, F., 1992, Tertiary granitoids of Rhodope, northern Greece: Magmatism related to extensional collapse of the Hellenic orogen?: Tectonophysics, v. 210, p. 295–314.

Kaiser Rohrmeier, M., von Quadt, A., Driesner, T., Heinrich, C.A., Handler, R., Ovtcharova, M., Ivanov, Z., Petrov, P., Sarov, St., and Peytcheva, I., 2013, Postorogenic extension and hydrothermal ore formation: High-precision geochronology of the central Rhodopian metamorphic core complex (Bulgaria-Greece): Economic Geology, v. 108, p. 691–718.

Kalogeropoulos, S.I., Kilias, S.P., Bitzios, D.C., Nicolaou, M., and Both, R.A., 1989, Genesis of the Olympias carbonate-hosted Pb-Zn (Au, Ag) sulfide ore deposit, eastern Chalkidiki Peninsula, northern Greece: Economic Geology, v. 84, p. 1210–1234.

Kamb, W.B., 1959, Ice petrofabric observations from Blue Glacier, Washington, in relation to theory and experiment: Journal of Geophysical Research, v. 64, p. 1891–1909.

Kilias, A., Falalakis, G., and Mountrakis, D., 1999, Cretaceous-Tertiary structures and kinematics of the Serbo-Macedonian metamorphic rocks and their relation to the exhumation of the Hellenic hinterland (Macedonia, Greece): International Journal of Earth Sciences, v. 88, p. 513–531.

Kilias, S.P., Kalogeropoulos, S.I., and Konnerup-Madsen, J., 1996, Fluid inclusion evidence for the physicochemical conditions of sulfide deposition in the Olympias carbonate-hosted Pb-Zn(Au, Ag) sulfide ore deposit, E. Chalkidiki Peninsula, N. Greece: Mineralium Deposita, v. 31, p. 394–406.

Kockel, F., Mollat, H., and Walther, H., 1971, Geologie des Serbomazedonischen massivs und seines mesozoischen Rahmes (Nord-Griechenland): Geologisches Jahrbuch der Bundesanstalt für Geowissenschaften und Rohstoffe, v. 89, p. 529–551.

Kockel, F., Mollat, H., and Gundlach, H., 1975, Hydrothermally altered and (copper-) mineralized porphyritic intrusions in the Serbo-Macedonian massif (Greece): Mineralium Deposita, v. 10, p. 195–204.

Kockel, F., Mollat, H., and Walther, H., 1977, Erläuterungen yur geologischen karte der Chalkidiki und agrenzender Gebiete 1:100,000 (Nord-Griechenland): Bundesanstalt für Geowissenschaften und Rohstoffe, Hannover, p. 1–119.

——1978a, Geological map of Greece, Stavros sheet: Athens, Institute of Geological and Mining Research, scale 1:50,000.

——1978b, Geological map of Greece, Stratoniki sheet: Athens, Institute of Geological and Mining Research, scale 1:50,000.

Koukouvelas, I.K., and Aydin, A., 2002, Fault structure and related basins of the North Aegean Sea and its surroundings: Tectonics, v. 21, p. 10-1–10-17.

Kounov, A., Wüthrich, E., Seward, D., Burg, J.P., and Stockli, D., 2015, Low-temperature constraints on the Cenozoic thermal evolution of the southern Rhodope core complex (northern Greece): International Journal of Earth Science, v. 104, p. 1337–1352.

Krenn, K., Bauer, C., Proyer, A., Klözli, U., and Hoinkes, G., 2010, Tectonometamorphic evolution of the Rhodope orogen: Tectonics, v. 29, TC4001, doi: 10.1029/2009TC002513.

Krohe, A., and Mposkos, E., 2002, Multiple generations of extensional detachments in the Rhodope mountains (northern Greece): Evidence of episodic exhumation of high-pressure rocks: Geological Society of London Special Publication, v. 204, p. 151–178.

Kroll, T., Müller, D., Seifert, T., Herzig, P.M., and Schneider, A., 2002, Petrology and geochemistry of the shoshonite-hosted Skouries porphyry Cu-Au deposit, Chalkidiki, Greece: Mineralium Deposita, v. 37, p. 137–144.

Kuiper, K.F., Deino, A., Hilgen, F.J., Krijgsman, W., Renne, R., and Wijbrans, J.R., 2008, Synchronizing rock clocks of Earth history: Science, v. 320, p. 500–504.

Kydonakis, K., Gallagher, K., Brun, J.-P., Jolivet, M., Gueydan, F., and Kostopoulos, D., 2014, Upper Cretaceous exhumation of the western Rhodope metamorphic province (Chalkidiki Peninsula, northern Greece): Tectonics, v. 33, p. 1113–1132.

Kydonakis, K., Brun, J.-P., Poujol, M., Monié, P., and Chatzitheodoridis, E., 2016, Inference on the Mesozoic evolution of the north Aegean from the isotopic record of the Chalkidiki block: Tectonophysics, v. 682, p. 65–84.

Liati, A., 2005, Identification of repeated Alpine (ultra) high-pressure metamorphic events by U-Pb SHRIMP geochronology and REE geochemistry of zircon: The Rhodope zone of northern Greece: Contributions to Mineralogy and Petrology, v. 150, p. 608–630.

Liati, A., Gebauer, D., and Fanning, C.M., 2011, Geochronology of the Alpine UHP Rhodope zone: A review of isotopic ages and constraints on the geodynamic evolution, *in* Dobrzhinetskaya, L.F., Faryad, S.W., Wallis, S., and Cuthbert, S., eds., Ultrahigh-pressure metamorphism 25 years after the discovery of coesite and diamond: Amsterdam, Elsevier, p. 295–324.

Lips, A.L., 2002, Correlating magmatic-hydrothermal ore deposit formation over time with geodynamic processes in SE Europe: Geological Society of London Special Publication, v. 204, p. 69–79.

Lips, A.L.W., White, S.H., and Wijbrans, J.R., 2000, Middle-Late Alpine thermotectonic evolution of the southern Rhodope massif, Greece: Geodinamica Acta, v. 13, p. 281–292.

Marchev, P., Kaiser-Rohrmeier, M., Heinrich, C., Ovtcharova, M., von Quadt, A., and Raicheva, R., 2005, 2: Hydrothermal ore deposits related to postorogenic extensional magmatism and core complex formation: The Rhodope massif of Bulgaria and Greece: Ore Geology Reviews, v. 27, p. 53–89.

Marrett, R.A., and Allmendinger, R.W., 1990, Kinematic analysis of fault-slip data: Journal of Structural Geology, v. 12, p. 973–986.

Márton, I., Dragić, D., Djordjević, B., Fox, P., Tosdal, R.M., van der Toorn, J., and Hasson, S., 2013, Intrusion-alteration-mineralization relationships from the porphyry Cu-Au deposit at Kiseljak, Serbia [ext. abs.]: 12th Biennial Society for Geology Applied to Mineral Deposits (SGA) Meeting: Mineral deposit research for a high-tech world, Uppsala, Sweden, 2013, Extended Abstracts.

McFall, K.A., Roberts, S., Teagle, D., Naden, J., Lusty, P., and Boyce, A., 2016, The origin and distribution of critical metals (Pd, Pt, Te, and Se) within the Skouries Cu-Au porphyry deposit, Greece: Mineral Deposits Study Group Meeting, 39th, Dublin, Ireland, 2016, Extended Abstracts.

Michailidou, A., Chatzipetros, A., and Pavlides, S., 2005, Quantitative analysis-tectonic geomorphology indicators of the faults in the region of

Stratoni-Varvara and Gomati-Megali Panagia (eastern Chalkidiki): Bulletin of the Geological Society of Greece, v. 38, p. 14–29.
Mposkos, E.D., and Kostopoulos, D.K., 2001, Diamond, former coesite and supersilicic garnet in metasedimentary rocks from the Greek Rhodope: A new ultrahigh-pressure metamorphic province established: Earth and Planetary Science Letters, v. 192, p. 497–506.
Nebel, M.L., 1989, Metamorphism and polygenesis of the Madem Lakkos polymetallic sulfide deposit, Chalkidiki, Greece: Unpublished Ph.D. thesis, Golden, Colorado, Colorado School of Mines, 215 p.
Nebel, M.L., Hutchinson, R.W., and Zartman, R.E., 1991, Metamorphism and polygenesis of the Madem Lakkos polymetallic sulfide deposit, Chalkidiki, Greece, Economic Geology, v. 86, p. 81–105.
Nelson, E.P., 2006, Drill-hole design for dilational ore shoot targets in fault-fill veins: Economic Geology, v. 101, p. 1079–1085.
Neubauer, F., 2002, Contrasting late Cretaceous with Neogene ore provinces in the Alpine-Balkan-Carpathian-Dinaride collision belt: Geological Society of London Special Publication, v. 204, p. 81–102.
Papanikolaou, D., 2013, Tectonostratigraphic models of the Alpine terranes and subduction history of the Hellenides: Tectonophysics, v. 595–596, p. 1–24.
Pavlides, S., and Caputo, R., 2004, Magnitude versus faults' surface parameters: Quantitative relationships from the Aegean region: Tectonophysics, v. 380, p. 159–188.
Pavlides, S., Caputo, R., Sboras, S., Chatzipetros, A., Papathanasiou, G., and Valkaniotis, S., 2010, The Greece catalogue of active faults and database of seismogenic sources: Bulletin of the Geological Society of Greece, v. 43, p. 486–494.
Pavlides, S.B., and Tranos, M.D., 1991, Structural characteristics of two strong earthquakes in the north Aegean: Ierissos (1932) and Agios Efstratios (1968): Journal of Structural Geology, v. 13, p. 205–214.
Pe-Piper, G., and Piper, D.J.W., 2002, The igneous rocks of Greece: Stuttgart, Borntraeger, 645 p.
——2006, Unique features of the Cenozoic igneous rocks of Greece: Geological Society of America Special Paper, v. 409, p. 259–282.
Pearce, J.A., 1996, A user's guide to basalt discrimination diagrams: Geological Association of Canada Short Course Notes, v. 12, p. 79–113.
——2014, Immobile element fingerprinting of ophiolites: Elements, v. 10, p. 101–108.
Piercey, S.J., 2014, A review of quality assurance and quality control (QA/QC) procedures for lithogeochemical data: Geoscience Canada, v. 41, p. 75–88.
Renne, P.R., and Norman, E.B., 2001, Determination of the half-life of ^{37}Ar by mass spectrometry: Physical Review, C 63 (047302), 3 p.
Renne, P.R., Swisher, C.C., Deino, A.L., Karner, D.B., Owens, T.L., and DePaolo, D.J., 1998, Intercalibration of standards, absolute ages, and uncertainties in $^{40}Ar/^{39}Ar$ dating: Chemical Geology, v. 145, p. 117–152.
Ricou, L.E., Burg, J.-P., Godfriaux, I., and Ivanov, Z., 1998, Rhodope and Vardar: The metamorphic and the olistostromic paired belts related to the Cretaceous subduction under Europe: Geodinamica Acta, v. 11, p. 285–309.
Ring, U., Glodny, J., Will, T., and Thomson, S., 2010, The Hellenic subduction system: High-pressure metamorphism, exhumation, normal faulting, and large-scale extension: Annual Reviews of Earth and Planetary Sciences, v. 38, p. 45–76.
Roddick, J.C., 1983, High-precision intercalibration of $^{40}Ar/^{39}Ar$ standards: Geochimica et Cosmochimica Acta, v. 47, p. 887–898.
Rollinson, H.R., 1993, Using geochemical data: Evaluation, presentation, interpretation: London, Longman, 352 p.
Sagui, C.L., 1928, The ancient mining works of Cassandra, Greece: Economic Geology, v. 23, p. 671–680.
Serafimovski, T., 2000, The Lece-Chalkidiki metallogenic zone: Geotectonic setting and metallogenic features: Geologija, v. 42, p. 159–164.
Serafimovski, T., Stefanova, V., and Volkov, A.V., 2010, Dwarf copper-gold porphyry deposits of the Buchim-Damjan-Borov Dol ore district, Republic of Macedonia (FYROM): Geology of Ore Deposits, v. 52, p. 179–195.
Sibson, R.H., 1977, Fault rocks and fault mechanisms: Journal of the Geological Society, London, v. 133, p. 191–213.
Siron, C.R., Thompson, J.F.H., Baker, T., Friedman, R., Tsitsanis, P., Russell, S., Randall, S., and Mortensen, J., 2016, Magmatic and metallogenic framework of Au-Cu porphyry and polymetallic carbonate-hosted replacement deposits of the Kassandra Mining District, Northern Greece: Society of Economic Geologists Special Publication 19, p. 29–55.
Sokoutis, D., Brun, J.P., Van Den Driessche, J., and Pavlides, S., 1993, A major Oligo-Miocene detachment in southern Rhodope controlling north Aegean extension: Journal of the Geological Society, London, v. 150, p. 243–246.
Spell, T.L., and McDougall, I., 2003, Characterization and calibration of $^{40}Ar/^{39}Ar$ dating standards: Chemical Geology, v. 198, p. 189–211.
Steiger, R.H., and Jäger, E., 1977, Subcommission on geochronology: Convention on the use of decay constants in geo- and cosmochronology: Earth and Planetary Science Letters, v. 36, p. 359–362.
Strmić-Palinkaš, S., Palinkaš, L.A., Renac, C., Spangenberg, J.E., Lüders, V., Molnar, F., and Maliqi, G., 2013, Metallogenic model of the Trepča Pb-Zn-Ag skarn deposit, Kosovo: Evidence from fluid inclusions, rare earth elements, and stable isotope data: Economic Geology, v. 108, 135–162.
Tobey, E., Schneider, A., Algería, A., Olcay, L., Perantonis, G., and Quiroga, J., 1998, Skouries porphyry copper-gold deposit, Chalkidiki, Greece: Setting, mineralization, and resources, *in* Porter, T.M., ed., Porphyry and hydrothermal copper and gold deposits: A global perspective: Adelaide, PGC Publishing, p. 175–184.
Tosdal, R.M., and Richards, J.P., 2001, Magmatic and structural controls on the development of porphyry Cu ± Mo ± Au deposits: Reviews in Economic Geology, v. 14, p. 157–181.
Turpaud, P., and Reischmann, T., 2003, Zircon ages of granitic gneisses from the Rhodope (N. Greece), determination of basement age evidences for a Cretaceous intrusive event: Geophysical Research Abstracts, 5:04435.
——2010, Characterization of igneous terranes by zircon dating: Implications for UHP occurrences and suture identification in the central Rhodope, northern Greece: International Journal of Earth Science, v. 99, p. 567–591.
Veligrakis, T., and Dalampiras, L., 2016, 3-D modeling contribution for producing near mine exploration targets at Olympias gold-rich polymetallic carbonate replacement deposit, Halkidiki, N. Greece [ext. abs.]: SEG 2016 Conference: Tethyan Tectonics and Metallogeny, Çeşme, Turkey, September 25–28, 2016, Extended Abstracts.
Wawrzenitz, N., and Krohe, A., 1998, Exhumation and doming of the Thassos metamorphic core complex (S. Rhodope, Greece): Structural and geochronological constraints: Tectonophysics, v. 285, p. 301–312.
Wawrzenitz, N., and Mposkos, E., 1997, First evidence for Lower Cretaceous HP/HT-metamorphism in the eastern Rhodope, North Aegean region, Northeast Greece: European Journal of Mineralogy, v. 9, p. 659–664.
Wilson, A.J., 2003, The geology, genesis, and exploration context of the Cadia gold-copper porphyry deposits, NSW, Australia: Unpublished Ph.D. thesis, Hobart, University of Tasmania, 335 p.
Wortel, M.J.R., and Spakman, W., 2000, Subduction and slab detachment in the Mediterranean-Carpathian region: Science, v. 290, p. 1910–1917.
Wüthrich, E., 2009, Low temperature thermochronology of the northern Aegean Rhodope massif: Unpublished Ph.D. thesis, Zürich, Switzerland, ETH Zürich, 210 p.

APPENDIX

Methodology

Structural analysis methods

Structural measurements were collected using a Brunton compass following the North American strike-dip and right-hand-rule convention. Structural data are presented on a lower-hemisphere, equal-area stereographic projection using Stereonet 9.5 software (Cardozo and Allmendinger, 2013) and contoured using the statistical method of Kamb (1959). Kinematic fault-strain features were measured following the criteria defined in Nelson (2006). Fault kinematic data are similarly presented in a lower-hemisphere, equal-area stereographic projection using FaultKin 7.0 software (Allmendinger et al., 2012). The infinitesimal strain axes, determined from the statistical Bingham axial distributions, were calculated and plotted for each fault population following the graphical kinematic method of Marrett and Allmendinger (1990).

Geochemistry methods

Whole-rock geochemical analyses of amphibolite samples were completed at Acme labs in Vancouver, British Columbia. Major and minor element analyses were determined by inductively coupled plasma-mass spectrometry (ICP-MS) and inductively coupled plasma-optical emission spectrometry (ICP-OES) after lithium metaborate and tetraborate fusion. Analytical accuracy and precision determined from internationally certified reference standards and duplicates, respectively, are within 5 relative percent for major oxides and within 10 relative percent for most minor and trace elements (calculation methods after Piercey, 2014). Whole-rock geochemical data used in this study is located in Table A1.

Immobile element geochemical data (Al, Nb, Nd, Th, Ti, Y, and Zr) from footwall and hanging-wall amphibolites in outcrop and drill core have basaltic compositions based on the immobile element ratio classification diagram of Pearce (1996, 2014; Fig. A1A). The degree of similarity between both amphibolite populations was further investigated using principal component analysis. Principal component analysis is a variance-maximizing projection that transforms a set of variables into proportional linear combinations of orthogonal vectors (principal components), which systematically decrease in their degree of variance (Rollinson, 1993). The first two principal components of the seven calculated account for 81% of the explained variance in the data (Fig. A1B) and are therefore considered adequate for the principal component interpretation (e.g., Jolliffe, 2002). The first principal component, representing a linear combination of variables with the highest variance, is completely overshadowed by the second principal component, which is represented by a combination of variables with the next highest degree of variance (Fig. A1C). The overlapping relationship shown here indicates that the footwall and hanging-wall amphibolite populations spanning the Stratoni fault zone display a high level of similarity and thus are interpreted to be of like origin.

$^{40}Ar/^{39}Ar$ geochronology methods

Samples were prepared and analyzed at the $^{40}Ar/^{39}Ar$ geochronology laboratory at the University of Manitoba in

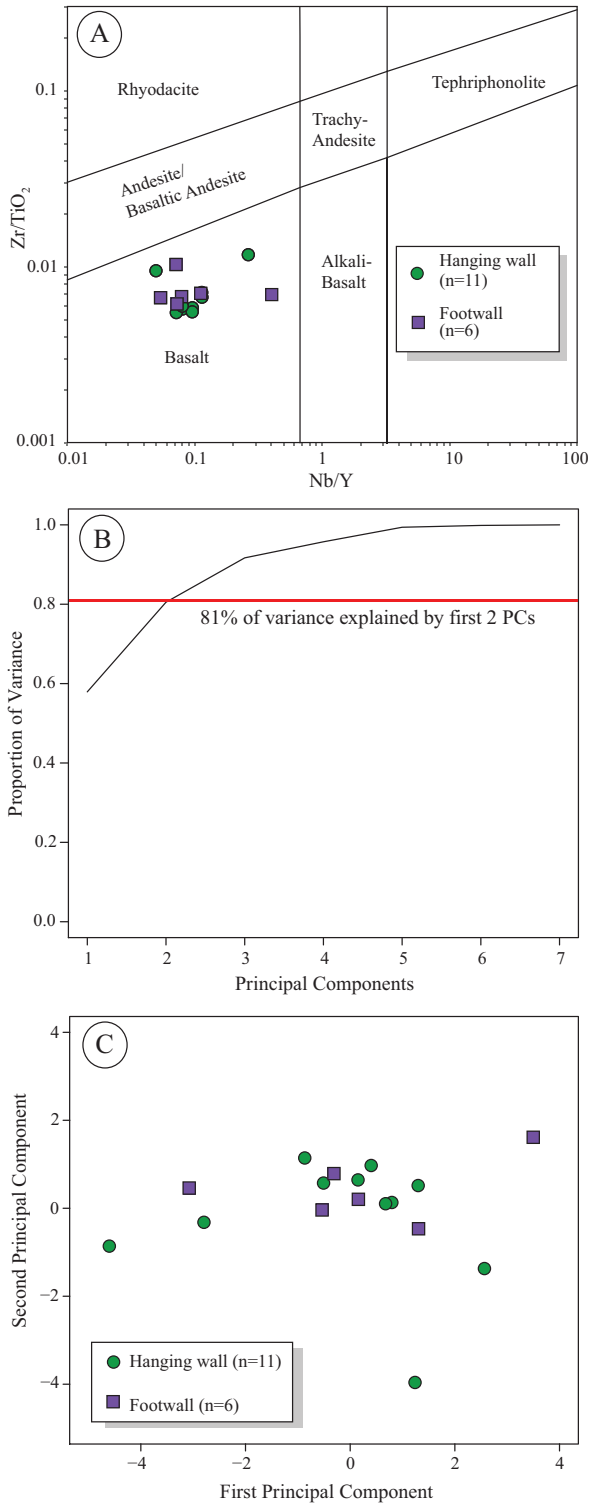

Fig. A1. Amphibolite trace element geochemical data. (A) Representative footwall (square) and hanging wall (circle) amphibolite samples from the Stratoni fault zone plotted on an immobile element-based discrimination diagram modified after Pearce (1996, 2014). (B) Scree plot explaining the percent variance for each of the principal components (PCs). The first two principal components represent a proportion of the variance (81%) as indicated by the horizontal red line. (C) Plot of first and second principal components showing the overlap in the footwall and hanging-wall amphibolite populations.

Winnipeg, Canada. The $^{40}Ar/^{39}Ar$ analytical work in this study was performed using a multicollector Thermo Fisher Scientific ARGUS VI mass spectrometer linked to a stainless steel Thermo Fisher Scientific extraction/purification line and Photon Machines (55 W) Fusions 10.6 CO_2 laser. Argon isotopes (with atomic mass ranging from 40 to 37) were measured using Faraday detectors with low-noise (1×10^{12} Ω) resistors. Argon with atomic mass of 36 was measured using a compact discrete dynode detector. The sensitivity for argon measurements is ~6.312×10^{17} moles/fA as determined from measured aliquots of the Fish Canyon sanidine (Dazé et al., 2003; Kuiper et al., 2008).

Standard and unknown samples were placed into 2-mm-deep wells within 18-mm-diameter aluminium disks, with standards placed strategically so that the lateral neutron flux gradients across the disk could be evaluated. Planar regressions were fit to the standard data, and the $^{40}Ar/^{39}Ar$ neutron fluence parameter (J) was interpolated for the unknown samples. Uncertainties in J are estimated at 0.1 to 0.2% (1 s) based on Monte Carlo error analysis of the planar regressions (Best et al., 1995). All specimens were irradiated in the cadmium-lined, in-core (CLICIT) facility of the Oregon State University TRIGA reactor. Unknown samples, including the Fish Canyon sanidine (Kuiper et al., 2008) and GA1550 biotite (Spell and McDougall, 2003) standards, were irradiated for 7 h.

Irradiated samples were placed in a Cu sample tray with a KBr cover slip and introduced into a stainless steel high-vacuum extraction line and baked with an infrared lamp for 24 h. Single crystals were either fused or step heated using the laser. Reactive gases were removed after ~3 min by three GP-50 SAES getters (two at room temperature and one at 450°C) prior to being admitted by expansion into an ARGUS VI mass spectrometer. Five argon isotopes were measured simultaneously over a period of 6 min. Measured isotope abundances were corrected for extraction-line blanks, which were determined before every sample analysis. Line blanks averaged ~4 fA for atomic mass 40 and ~0.015 fA for atomic mass 36.

Mass discrimination, monitored by online analysis of air pipettes, resulted in a mean D = 1.01312 ± 0.00109 per atomic mass unit based on 28 aliquots interspersed with the unknown samples. A value of 295.5 was used for the atmospheric $^{40}Ar/^{36}Ar$ ratio (Steiger and Jaëger, 1977) for the purposes of routine measurement of mass spectrometer discrimination using air aliquots and correction for atmospheric argon in the $^{40}Ar/^{39}Ar$ age calculation. Corrections are made for neutron-induced ^{40}Ar from potassium, ^{39}Ar and ^{36}Ar from calcium, and ^{36}Ar from chlorine (Roddick, 1983; Renne et al., 1998; Renne and Norman, 2001). Geochronological data used in this study is located in Table A2.

Chris Siron is an economic geologist with 10 years of experience researching and exploring for porphyry Cu-Mo-Au and polymetallic carbonate-hosted replacement deposits, orogenic Au systems, and uranium roll-front deposits. His current research focuses on understanding the structural evolution of regions and the implications for ore formation. He holds degrees from the Colorado School of Mines, Golden, Colorado, in economic geology and geological engineering and is currently a Ph.D. candidate in the department of geological sciences at Cornell University, Ithaca, New York.